Study of planar pixel sensors hardened to radiations for the upgrade of the ATLAS vertex detector

Mathieu Benoit

LAL 11-118
Mai 2011

THÈSE

Présentée le 10 juin 2011

par

Mathieu BENOIT

pour obtenir le grade de

Docteur ès Sciences
de l'Université Paris XI, Orsay

Étude des détecteurs planaires pixels durcis aux radiations pour la mise à jour du détecteur de vertex d'ATLAS

Soutenue devant la commission d'examen composée de :

M.	E.	Augé	
M.	G	Casse	Rapporteur
M.	C.	Goessling	Rapporteur
M.	L.-A.	Hamel	
M.	A.	Lounis	Directeur de thèse
M.	A.	Stocchi	Président

"I've found from past experiences that the tighter your plan, the more likely you are to run into something unpredictable."
MacGyver

Résumé

Le Large Hadron Collider (LHC), située au CERN, Genève, produit des collisions de protons accélérés à une énergie de 3.5 TeV depuis le 23 Novembre 2009. L'expérience ATLAS enregistre depuis des données et poursuit sa recherche de nouvelle physique à travers l'analyse de la cinématique des événements issues des collisions. L'augmentation prévue de la luminosité sur la période s'étalant de 2011 2020 apportera de nouveaux défis pour le détecteur qui doivent être considérés pour maintenir les bonnes performance de la configuration actuelle. Le détecteur interne sera le sous-détecteur le plus affecté par l'augmentation de la luminosité qui se traduira par une augmentation des dommages occasionés par la forte radiation et par la multiplication du nombre de traces associées à chaque croisement de faisceau. Les dommages causés par l'irradiation intense entrainera une perte d'efficacité de détection et une réduction du nombre de canaux actifs.

Un intense effort de Recherche et Developpement (R&D) est présentement en cours pour concevoir un nouveau détecteur pixel plus tolérant aux radiations et au cumul des événements générant un grand nombre de traces à reconstruire. Un premier projet de mise-à-jour du détecteur interne, nommé Insertable B-Layer (IBL) consiste à ajouter un couche de détection entre le tube à vide du faisceau et la première couche de silicium. Le projet SLHC prévoit de remplacer l'ensemble du détecteur interne par une version améliorée plus tolérante aux radiations et aux cumuls des événements. Dans cet ouvrage, je présente une étude utilisant la simulation technologique assisté par ordinateur (TCAD) portant sur les méthodes de conception des détecteurs pixels planaires permettant de réduire les zones inactives des détecteurs et d'augmenter leurs tolérances aux radiations. Les différents modèles physiques disponible ont étés étudiés pour développer un modèle cohérent capable de prédire le fonctionnement des détecteurs pixels planaires après irradiation. La structure

d'anneaux de gardes utilisée dans le détecteur interne actuel a été étudié pour obtenir de l'information sur les possible méthodes permettant de réduire l'étendu de la surface occupée par cette structure tout en conservant un fonctionnement stable tout au long de la vie du détecteur dans l'expérience ATLAS. Une campagne de mesures sur des structures pixels fut organisée pour comparer les résultats obtenue grâce à la simulation avec le comportement des structures réelles. Les paramètres de fabrication ainsi que le comportement électrique ont été mesurés et comparés aux simulations pour valider et calibrer le modèle de simulation TCAD. Un modèle a été développé pour expliquer la collection de charge excessive observée dans les détecteurs planaires en silicium lors de leur exposition a une dose extrême de radiations.

Finalement, un modèle simple de digitalisation à utiliser pour la simulation de performances detecteurs pixels individuels exposès à des faisceau de hauteènergie ou bien de l'ensemble du détecteur interne est présenté. Ce modèle simple permets la comparaison entre les données obtenue en faisceau test aux modèle de transport de charge inclut dans la digitalisation. Le dommage dû à la radiation , l'amincissement et l'utilisation de structures à bords minces sont autant de structures dont les effets sur la collecte de charges affectent les performance du détecteur. Le modèle de digititalisation fut validé pour un détecteur non-irradié en comparant les résultats obtenues avec les données acquises en test faisceau de hauténergie. Le modèle validé sera utilisé pour produire la première simulation de l'IBL incluant les effets d'amincissement du substrat, de dommages dûes aux radiations et de structure dotés de bords fins.

Keywords : Dommage induit par la radiation, silicium, détecteur pixel planaires, simulation TCAD, test faisceau , IBL, SLHC

Abstract

In this work, is presented a study, using TCAD simulation, of the possible methods of designing of a planar pixel sensors by reducing their inactive area and improving their radiation hardness for use in the Insertable B-Layer (IBL) project and for SLHC upgrade phase for the ATLAS experiment. Different physical models available have been studied to develop a coherent model of radiation damage in silicon that can be used to predict silicon pixel sensor behavior after exposure to radiation. The Multi-Guard Ring Structure, a protection structure used in pixel sensor design was studied to obtain guidelines for the reduction of inactive edges detrimental to detector operation while keeping a good sensor behavior through its lifetime in the ATLAS detector. A campaign of measurement of the sensor's process parameters and electrical behavior to validate and calibrate the TCAD simulation models and results are also presented. A model for diode charge collection in highly irradiated environment was developed to explain the high charge collection observed in highly irradiated devices.

A simple planar pixel sensor digitization model to be used in test beam and full detector system is detailed. It allows for easy comparison between experimental data and prediction by the various radiation damage models available. The digitizer has been validated using test beam data for unirradiated sensors and can be used to produce the first full scale simulation of the ATLAS detector with the IBL that include sensor effects such as slim edge and thinning of the sensor.

Keywords : Radiation Damage, Multi-Guard Ring Structure, Silicon detector, TCAD simulation, Digitization, Planar Pixel Sensor, Slim edges, Test Beam, IBL, SLHC

Table des matières

Introduction

The Large Hadron Collider, located in CERN, Geneva, has been delivering collisions of proton beam accelerated to an energy of 3.5 TeV since November 23 2009. since then, the ATLAS experiment has been recording data to search for new physics to be discovered through analysis of the collision kinematic. The planned luminosity rise for the period between 2011 and 2020 will however bring new challenge to the detector that will need to be addressed to maintain the performance of the actual detector. The inner detector will be the most challenged with the increased amount of tracks per collision to detect, resulting from the high luminosity upgrade. Radiation damage in its sensors and electronics will eventually reduce the efficiency and lead to failure of the detector system. Aging of the detector will also reduce the number of active channels and increase the detection inefficiency.

An intense R&D effort has been ongoing to design a new pixel detector capable of handling increased occupancy linked to higher luminosity and able to resist to radiation damage induced by the collisions. The Insertable B-Layer (IBL) project has been created to perform a first update of the detector by adding a new pixel layer between the beampipe and the actually inner layer of the pixel detector. The SLHC project plans to replace the whole inner detector with an improved version able to withstand a ten fold increase in radiation damage and track multiplicity. In this work, I present a study, using TCAD simulation, of the possible method of design of a planar pixel sensors reducing their inactive area and improving their radiation hardness. Different physical models available have been studied to develop a coherent model of radiation damage in silicon that can be used to predict silicon pixel sensor behavior after exposure to radiation. The Multi-Guard Ring Structure used in pixel sensor design was studied to obtain guidelines for the reduction

of inactive edges detrimental to detector operation while keeping a good sensor behavior through its lifetime in the ATLAS detector. A campaign of measurement of the sensor's process parameters and electrical behavior to validate and calibrate the TCAD simulation models and results will also be presented in this work. A model for charge collection in highly irradiated diode was developed to explain the high charge collection observed in highly irradiated devices.

Finally , a simple planar pixel sensor digitization model to be used in test beam and full detector system is presented. The simple model allow for easy comparison between experimental data and prediction by the various radiation damage models available. The digitizer has been validated using test beam data for unirradiated sensors and can be used to produce the first full scale simulation of the ATLAS detector with the IBL that include sensor effects such as slim edge and thinning of the sensor.

Chapitre 1

The ATLAS experiment and upgrade project

1.1 The Large Hadron Collider

The Large Hadron Collider is a 27 km diameter proton accelerator and collider using supra-conductive magnet technology, located in CERN, designed to operate at a nominal energy of 7 TeV. The particle beam accelerated in the LHC originate from the accelerator complex present on site at CERN [1], as seen on figure 1.1. The proton synchrotron produce a beam of an energy of 25 GeV that is the injected in the Super Proton synchrotron which accelerate the protons up to an energy of 450 GeV. The protons are then injected in the LHC and accelerated to an energy up to 7 TeV. The machine nominal operation luminosity is $10^{34}\ cm^{-2}s^{-1}$. At the moment of writing these line, the LHC was operated at a beam energy of 3.5 TeV for a peak luminosity of $8.3 \times 10^{32}\ cm^{-2}s^{-1}$.

Figure 1.2 show the peak luminosity recorded by the ATLAS detector and delivered by the LHC for the period spanning from january 2011 to may 9th 2011. The luminosity is exponentially increasing toward the nominal value for which the machine was designed. A shutdown of the machine is planned for 2013 to allow maintenance and reparation. Work on the magnet is scheduled to allow to reach nominal energy of 7 TeV per proton. Two beam circulate in the clockwise and counterclockwise direction of the accelerator and can collide at 4 main point around the ring, where are located the 4 main LHC experiments : ATLAS, CMS, LHCb and ALICE.

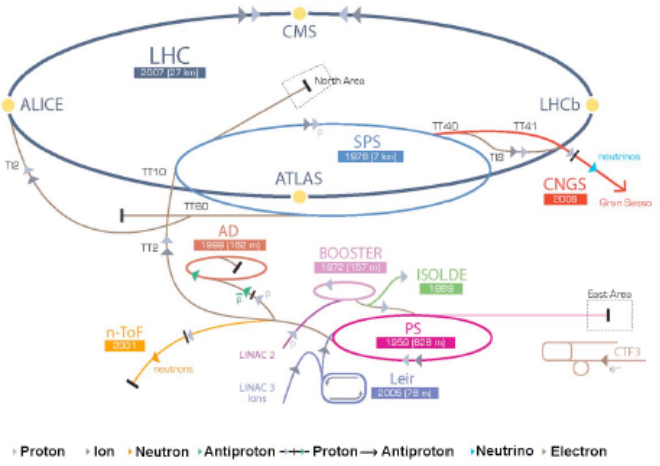

FIGURE 1.1 – The LHC and CERN accelerator complex

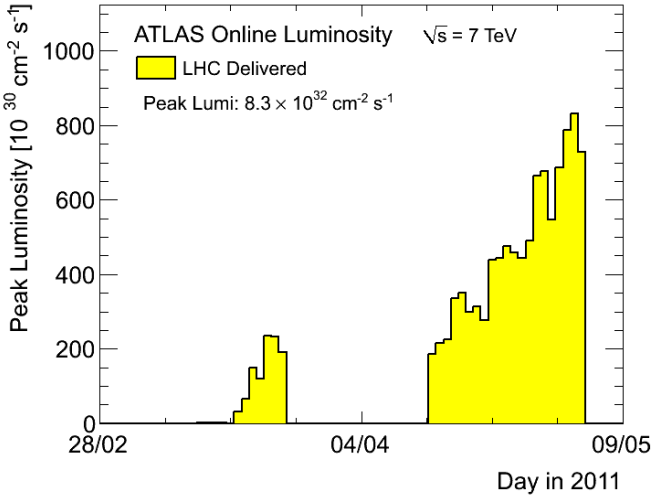

FIGURE 1.2 – ATLAS recorded Online peak luminosity per day for 2011

1.2 The ATLAS experiment

The ATLAS (A Toroidal LHC ApparatuS) experiment is a particle collider installed on the LHC experiment. This general purpose detector focus on the detection of the elusive Higgs boson through various decay channels and on the research of new physics beyond the standard model . The ATLAS detector is composed of three main concentric sub-detector represented on figure 1.3 : The inner detector, used for trajectory and impulsion measurement of charged particle, the calorimeters measuring the electromagnetic and hadronic energy deposition of the particles emanating from the interaction point and the muon spectrometer used to measure the impulsion and trajectory of the weakly interacting muons. The inner detector is enclose in a solenoid with a magnetic field of 2 T allowing the measurement of the transverse momentum of the particle crossing its volume using the curvature of the track in the magnetic field oriented along the beam direction. The muon spectrometer is enclosed in a toroidal magnet system with a magnetic field of 4 T.

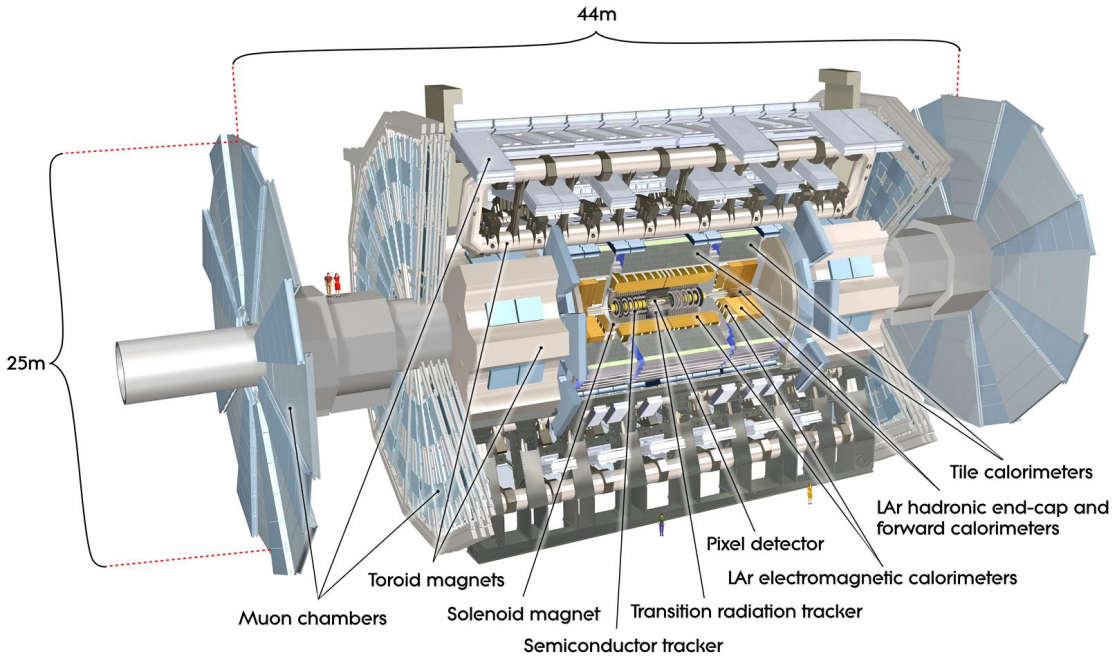

FIGURE 1.3 – The ATLAS detector

The ATLAS detector is designed to operate at a collision frequency of 40 MHz with

bunch crossing every 25 ns. The amount of interaction at this rate and luminosity would be to large to be recorded and a on detector trigger system. called level 1 trigger, filter the interesting event using the calorimetric information. The trigger system identify the bunch crossing timestamp and retrieve from the detector the information related to that timestamp from the detector systems holding the data. Higher level trigger system are then applied to further reduce the amount of data and select only interesting event emanating from the collision of the proton in the center of the machine.

1.2.1 The Inner detector

The inner detector [2] is an essential part of ATLAS that has for purpose to measure the trajectories of particles produced during the collisions of high energy protons beam produced by the LHC. The detector is composed of three subsystems : The pixel detector , the Semi-Conductor Tracker (SCT) and the Transition radiation Tracker (TRT). The pixel detector consists of three concentric barrels of pixel detector modules located at 5.05, 8.85 and 12.25 cm from the interaction point and of 6 disk, 3 on each side of interaction point, located at a mean z of 49.5, 58.0 and 65.0 cm with regard to the interaction point. Fig. 1.4 shows the cylindrical layers formed by the Inner Detector's subsystems. Particle beams will travel in the cylinder's Z direction and collision will take place at the geometrical center of the inner detector cylindrical structure.

The barrels are assembled with 1744 modules, shown in figure 1.5, each containing 16 front-end electronics 2880 channel chips, labeled FE-I3, bump-bonded to the pixel sensors mounted on a flex-hybrid circuit board, along with a module control chip (MCC). The module are assembled into ladders then paired to form a bistave structure, shown in figure 1.6a. The bistaves are then assembled on the support tube to form half shell assemblies , shown in figure 1.6b, that are then clamped together to form a pixel layer. The disk contain each 48 modules for a total of 288 modules for both end caps. The inner detector covers a region of $\pm 2.5\eta$ in the pseudo-rapidity coordinate system where $\eta = -ln(tan(\theta/2))$. Each sensor exhibit pixels of 400x50 μm leading to a hit position reconstruction resolution of 12 μm in ϕ at normal incidence.

The modules of the bistave assembly of the pixel barrels are overlapping in the Φ

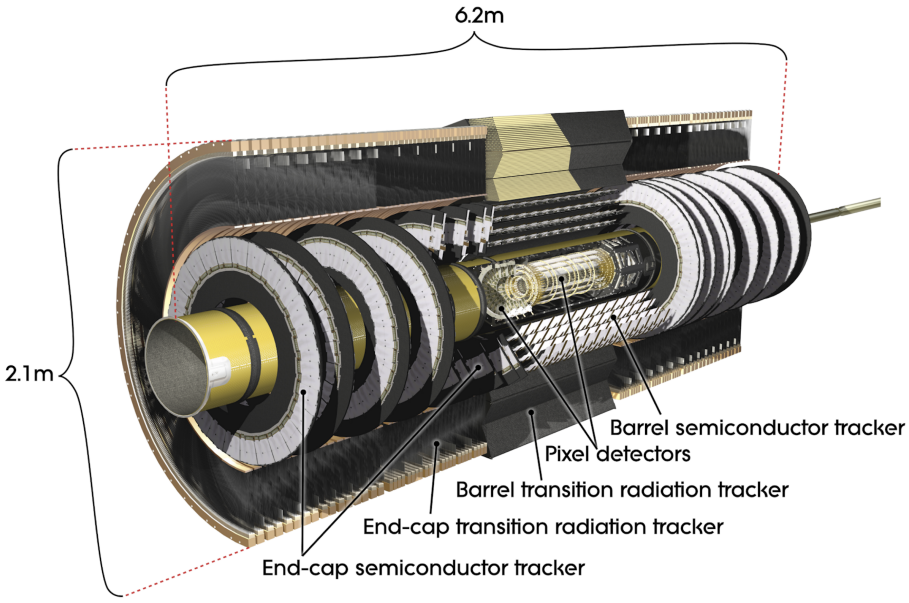

FIGURE 1.4 – 3D view of ATLAS Inner Detector, including Silicon tracker (SCT) and Transition Radiation Tracker (TRT) [3]

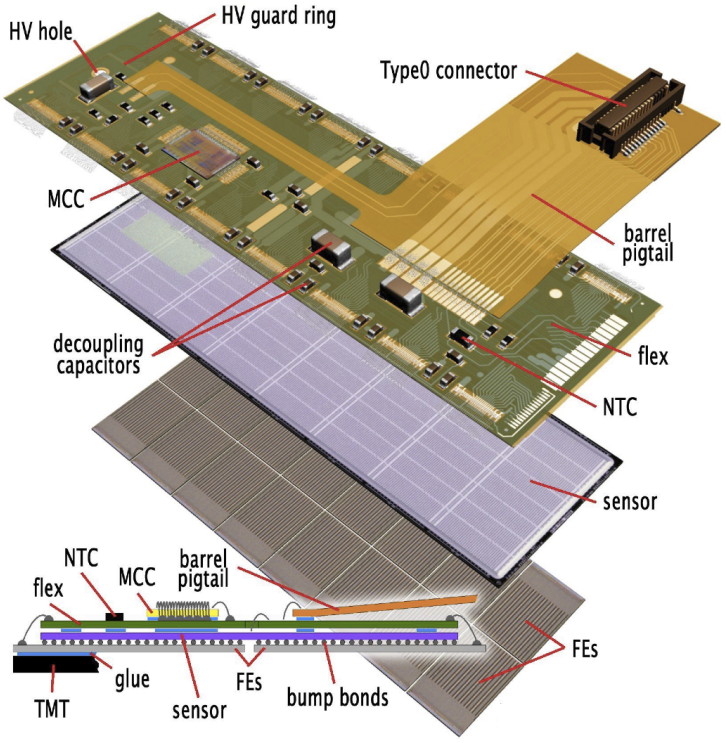

FIGURE 1.5 – Schematic view of a barrel pixel module [2]

direction (angular coordinate in the cylindrical coordinate system), as shown on Fig. 1.7. This overlap of detector modules is necessary to ensure an hermetic tracking coverage in Φ needed to separate simultaneous tracks from high transverse energy particles produced by the collisions at the interaction point. The edges of the pixel modules are not active area and need to be covered by the active area of the preceding and following modules along the half-shell assembly. This overlap of the sensors increase the amount of material between the interaction point and the calorimeters and has been reduced as much as possible to limit its effect on data quality.

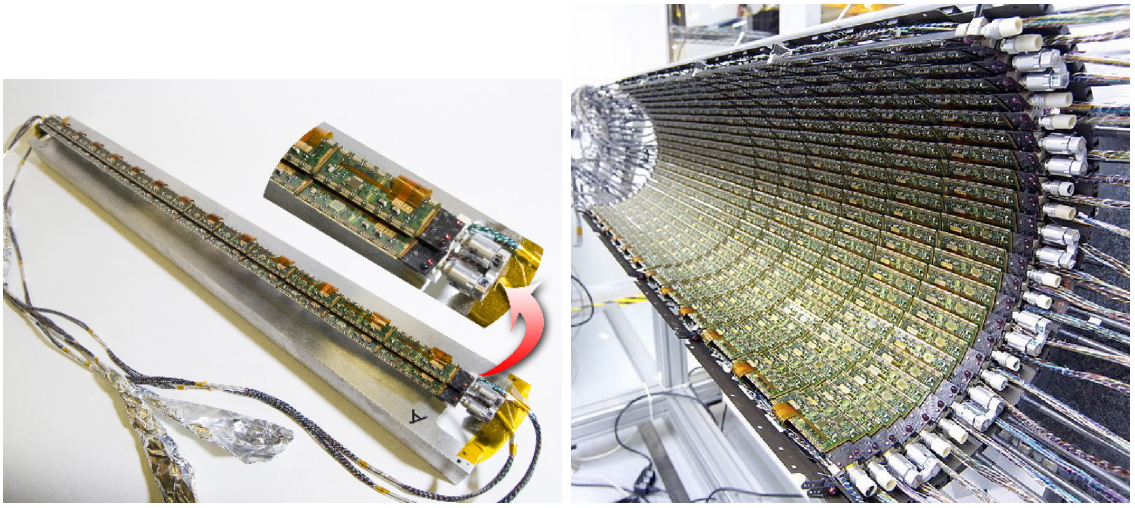

(a) The bistave assembly (b) Half shell assembly

FIGURE 1.6 – Bistave and half-shell structure of the ATLAS pixel detector [4]

The position of the three detector layers close to the interaction point lead to a high number of charged and neutral particles crossing the detector. Radiation damage in these zone near the origin of the interactions will affect the performance of the innermost detector system. The inner detector innermost pixel layer, the b-layer, will be exposed to fluences of the order of 5×10^{15} n_{eq}/cm^2) at the end of its lifetime. Figure 1.8 show the simulated level of radiation damage in equivalent to 1 MeV neutrons for the inner detector for a 10^7 seconds of operation at nominal luminosity. The pixel sensors forming the tracker will suffer from high fluences phenomena like the formation of a double Junction/double electric field peak and Space-Charge Sign Inversion (SCSI) [5; 6]. Radiation effects also include an increase in the bias potential required to fully deplete the pixel sensors as the acceptor-like traps

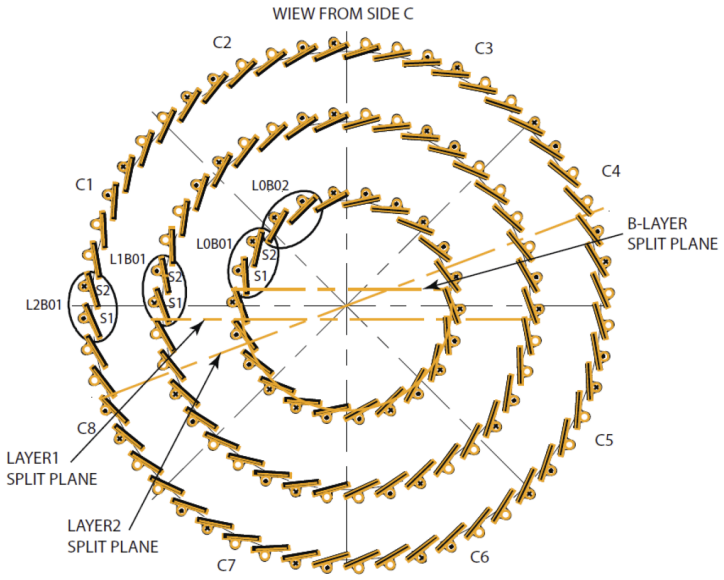

FIGURE 1.7 – Layout of the barrel pixel modules, R-Phi plane view [3]

concentration in silicon increases with exposure to radiation. The sensors will be operatedat full depletion voltage in order to measure significant charge signals from particles crossing the sensors, as collected charge is reduced by the trapping in defects created by radiation.

The Semiconductor tracker, or SCT, shown in figure 1.9, surround the pixel detector. The detector is composed of two layers of micro-strip silicon p-in-n sensors rotated by an angle of 40 mrad with regard to each other. Strip are 80 μm x 128 mm long with the 80 μm pitch oriented in the ϕ direction. Four cylindrical layers are positioned at respective radius of 29.9, 37.1, 44.3 and 51.4 cm with regard to the interaction point at $\phi = 0$. Nine end-caps complete the system. The end-caps are located on each side of the interaction point at a distances between 85 and 272 cm of the interaction point in the z direction. The z and r positioning resolution of the SCT modules are respectively of 580 μm and 17 μm and cover a region of $\pm 2.5\eta$ in pseudo-rapidity.

The final part of the inner detector is the Transition Radiation Tracker sitting at a radius between 55.4 and 108.2 cm of the interaction point. The system is composed of 351000 tubes of 4mm diameter filled with a gas mixture of Xe, CO_2 and O_2. A gold plated wire travel through the middle of the straw to form a detection electrode. A bias voltage of 1530V is applied between the outer surface and the wire to form an electric field inside

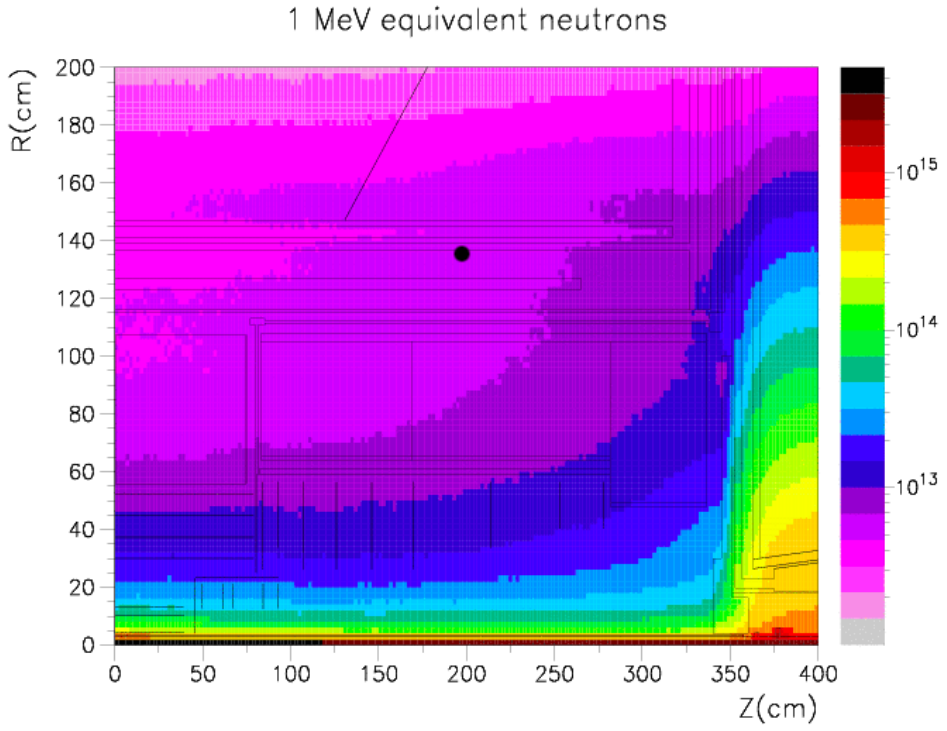

FIGURE 1.8 – Annual 1 MeV neutron equivalent fluences assuming 10^7 s at nominal luminosity [7]

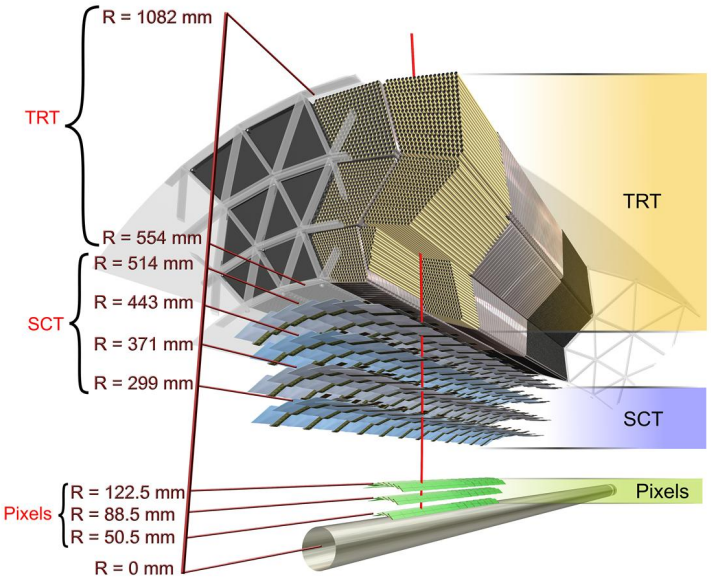

FIGURE 1.9 – The inner detector layer structure

the tube where ions and electron can drift . Particle crossing the tube deposit energy by ionizing the gas and creating free charge that drift toward the electrode. Electrons crossing the tubes will also produce transition radiation photon that will yield additional signal with regard to other charge particles, allowing identification of the electrons using a two threshold system. Positioning resolution in the r-ϕ plane is 130 μm.

1.2.2 The calorimeter

The calorimeter system, shown in figure 1.10 surrounds the inner detector and is used to accurately measure the energy of the particle and jets coming from collision interactions. The calorimeter is divided into two main parts : The electromagnetic calorimeter and the hadronic calorimeter. The design of the system has been done to minimize the dead area in the coverage in the r-ϕ plane and maximize the uniformity of the response to energy deposition.

The electromagnetic calorimeter is a sampling calorimeter using liquid argon as the

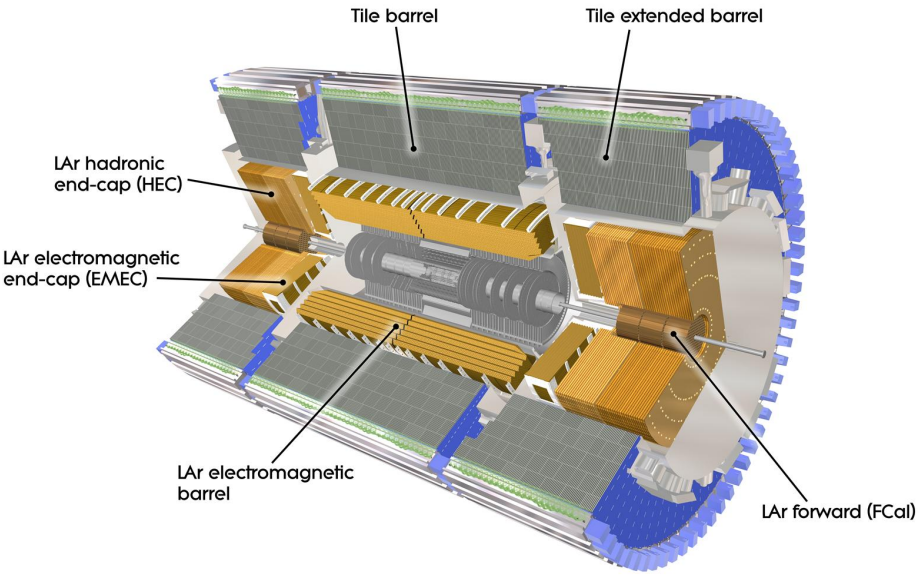

FIGURE 1.10 – The ATLAS calorimeter system

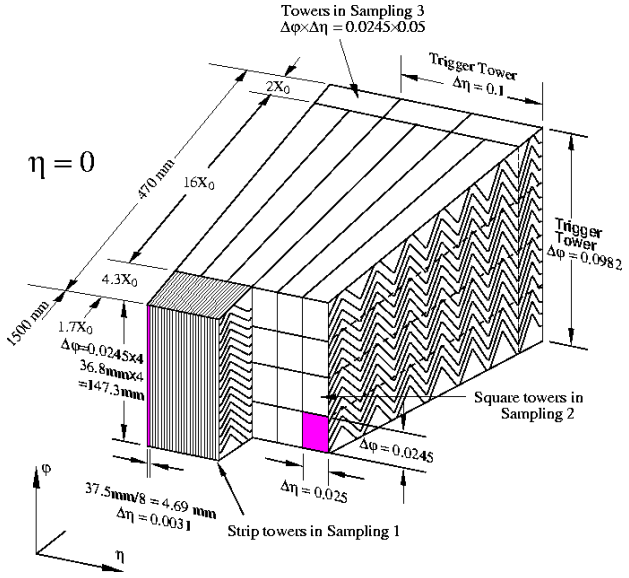

FIGURE 1.11 – The ATLAS calorimeter system

detection medium. The accordeon electrode geometry, shown in figure 1.11 allow to obtain a complete r-ϕ coverage and uniform material budget. The barrel part of the electromagnetic calorimeter extend between $\pm 3.2\eta$ while the endcaps cover the range of $3.2 < |\eta| < 4.9$. The barrel of the calorimeter is divided in three longitudinal section for $|\eta| < 2.5$. and two segment for $2.5 < |\eta| < 3.2$. A presampler calorimeter with fine granularity strips is present for $|\eta| < 1.8$ to allow correction for energy loss in the inner detector , cryostats and service located before the calorimeter. The measured energy resolution of the electromagnetic calorimeter has been found to be described by equation 1.1 where a is a stochastic term equal to 10% and b a constant equal to 0.17%.

$$\frac{\sigma(E)}{E} = \frac{a}{\sqrt{(E(GeV))}} \oplus b \tag{1.1}$$

The forward region of the calorimeter, located in $3.1 < |\eta| < 4.9$, is called the Forward Calorimeter (FCAL) and also use liquid argon as a detection medium. The readout electrode are cylinder parallel to the beam direction inserted in a copper matrix with a distance of 250 μm between the electrodes and the wall of the matrix, as shown in figure 1.12. A quartz spacer is used to maintain the distance between the electrode tube and the copper matrix and liquid argon fills the gap between the two surfaces.

The hadronic calorimeter is divided into two subsystems : The Tile Calorimeter and the Hadronic End-Cap plus Forward Calorimeter. The Tile Calorimeters extend for the $|\eta| < 1.6$ pseudorapidity region of the detector. It is composed of modules scintillating tiles stacked between Iron absorbers slabs, as shown on figure 1.13, . Each tile is read through an wavelength shifting optical fibers coupled to photomultipliers. Timing resolution of the photomultipliers is 23.5 ns , allowing to tag hadronic interaction to the correct Level 1 trigger clock.

The Forward Calorimeters and Hadronic End-Cap are liquid Argon sampling calorimeters located at each end of the detector, in the $3.1 < |\eta| < 4.9$ pseudo-rapidity region. The Hadronic End-Cap is formed of 128 modules of parallel plate liquid argon chambers , 32 for each wheel, an example of which can be seen in figure 1.14. The FCAL use the same electrode structure as the electromagnetic calorimeter with a Tungsten matrix instead of

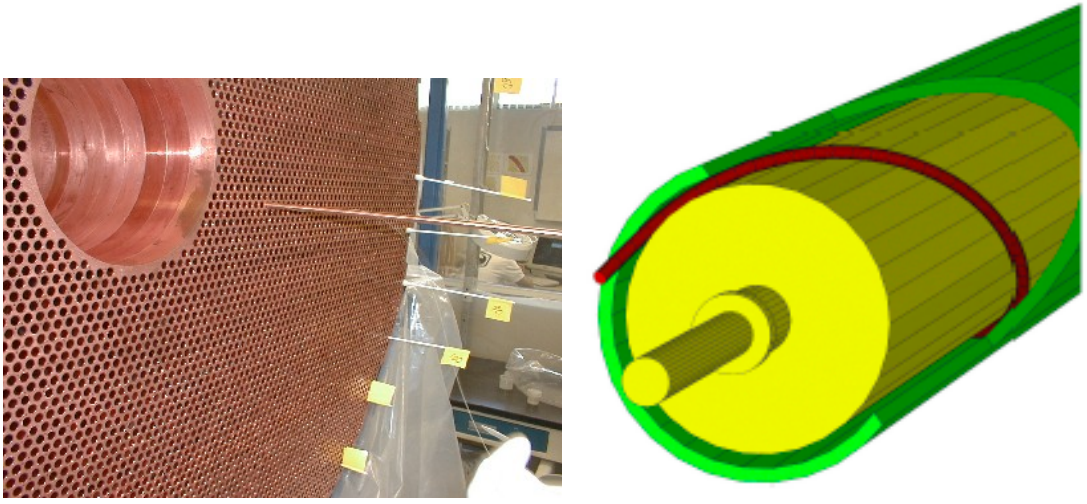

(a) FCAL endcap copper matrix (b) FCAL endcap electrode geometry

FIGURE 1.12 – The ATLAS forward calorimeter electrode structure and its copper matrix

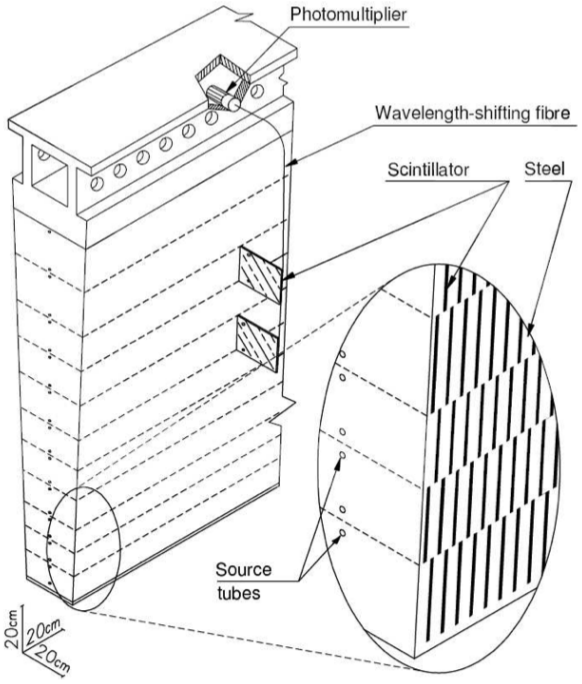

FIGURE 1.13 – The ATLAS Tile Calorimeter module

copper. Disposition of the different forward calorimeter system is described in figure 1.15.

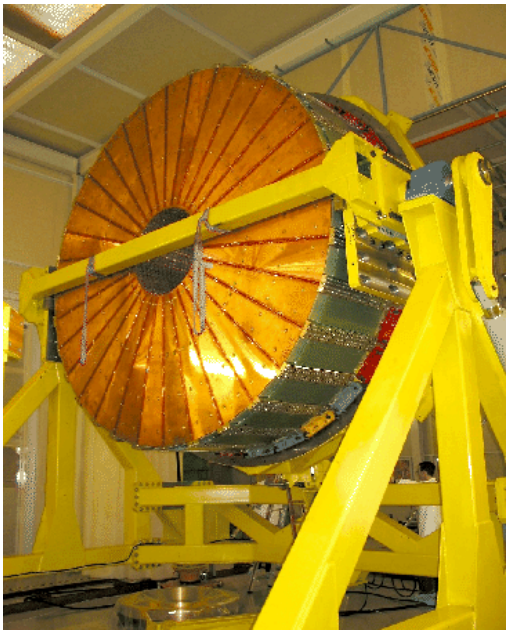

FIGURE 1.14 – An ATLAS End-Cap calorimeter wheel

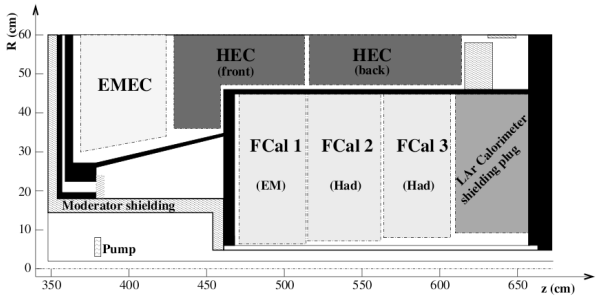

FIGURE 1.15 – ATLAS Forward region disposition of calorimeters systems

1.2.3 The muon spectrometer

The muon spectrometer, shown in figure 1.16, is of a rapid detection system located outside the toroidal magnet system, used for triggering on muons coming from interactions, and a precision measurement system located inside the toroid magnetic field and used to measure accurately the impulsion of the muons by measuring the curvature of their tracks in the field. Three type of detection module are used in the detector system :

The Thin-Gap chamber (TGC)

The Cathode strip chambers (CSC)

The Monitored drift tubes (MDT)

The Resistive-plate chambers (RPC)

The precision measurement chambers are located in the central region of the detector at a radius of 5, 7.5 and 10 m with regard to the interaction point, and in the End-Cap regions at z = 7 and 22 m. They are composed of MDT and CSC modules. the fast trigger chambers are present in the $|\eta|$ pseudo-rapidity region. They are composed of RPC for the barrel section and TGC for the end caps.

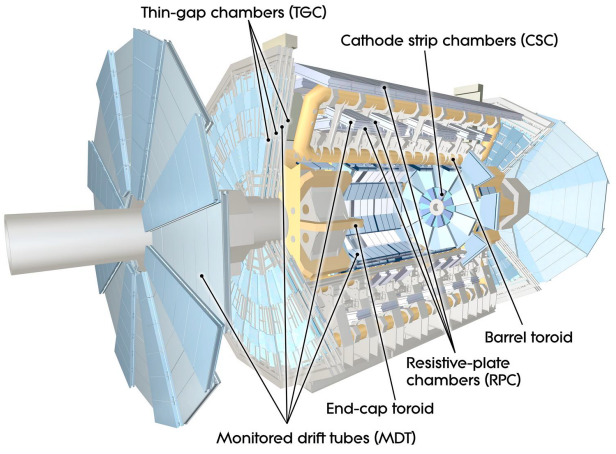

FIGURE 1.16 – The ATLAS Muon Spectrometer

The ATLAS detector has been recording data since november 23 2009. The readiness of all the subsystem has allowed a rapid progress in energy, luminosity and physics analysis. Figure 1.17 show an example of a Z muon candidate in the 2010 run data decaying into 2 back to back electrons with transverse energy of 40 and 45 GeV. The electron track reconstruction in the inner detector is shown, along with their measured energy in the electromagnetic calorimeter.

1.3 THe ATLAS upgrade projects

The LHC was designed to produce a luminosity of $10^{34} cm^{-2} s^{-1}$. An upgrade of the accelerator is planned to increase even further the luminosity delivered by the machine. Three phase have been planned in the upgrade project [8]. Phase 1 will consist of an

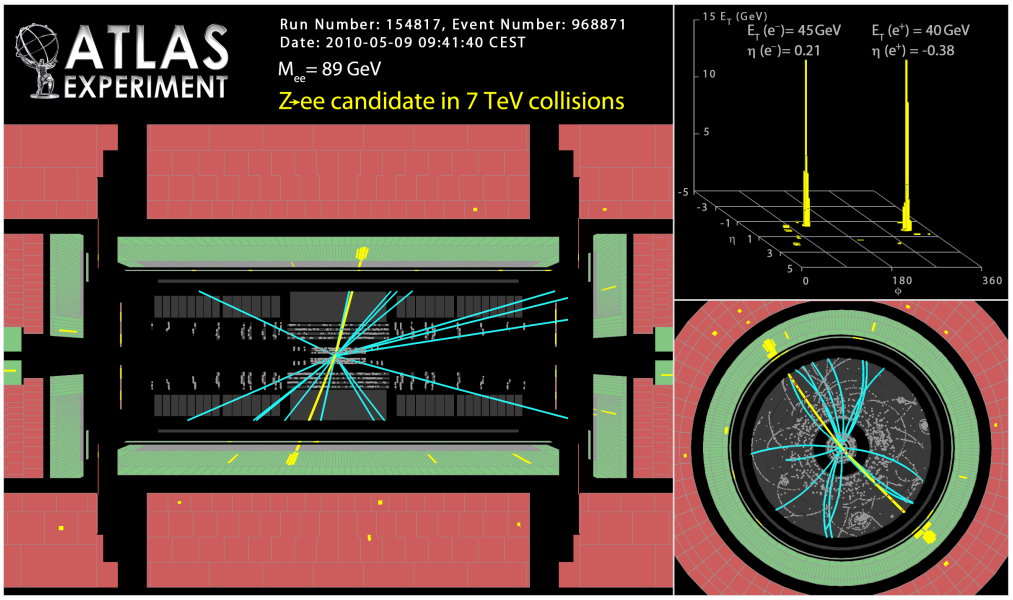

FIGURE 1.17 – Z boson candidate in the ATLAS detector

increase to a luminosity up to $2.3 \times 10^{34} cm^{-2} s^{-1}$ without any modifications to the machine itself by pushing the machine to its maximum performance. Phase 2, called the SLHC phase, would see a factor 10 increase in luminosity with regard to the nominal luminosity. Modification to the injection system will be performed to increase injection energy in the LHC at 1TeV, instead of the 450 GeV currently produced by the SPS. Modification to the insertion quadrupole and to the machine parameters would then allow to increase luminosity.

The ATLAS pixel detector, located very close to interaction point, will see a increasing amount of radiation as a consequence of the luminosity upgrade. The system was designed to operate at the actual nominal luminosity and modification to the system will be needed to cope with the increased pile-up of interaction at each bunch crossing to ensure a stable detection efficiency, independent of luminosity. Two upgrade projects are planned to add a new pixel layer and eventually replace the entire pixel detector to handle the problems brought by an increase in luminosity : The Insertable B-Layer (IBL) and the SLHC upgrade.

1.3.1 Phase 1 : The Insertable B-Layer (IBL)

The IBL project [9] consist in building a new layer for the pixel detector that will be inserted between the beampipe and the actual b-layer. The main motivation behind this detector upgrade are :

1. Tracking Robustness : Failure of actual module as they age and suffer from radiation damage will affect tracking efficiency and precision. The addition of an additional space point will provide a more robust tracking by compensating for the failed sensors and by giving information about tracks from a distance closer to interaction point.
2. Luminosity effects : Increase in luminosity will produce more tracks per bunch crossing to be reconstructed by the pixel detector. Readout inefficiencies on the current sensor will reduce the overall detection inefficiency and the IBL will provide a system with a increased occupancy capacity to compensate for this effect.
3. Tracking precision : The location of the IBL, closer to interaction point, will allow for more accurate reconstruction of the primary vertex and b-tagging. The insertion of the IBL will result in an increase in sensitivity to physics channel using these parameters.
4. Radiation Damage : The actual b-layer is foreseen to resist to radiation doses of $1 \times 10^{15} n_{eq} cm^{-2}$. In the best scenario of luminosity upgrade, radiation damage inflicted during pixel detector operation could eventually lead to a failure of the system due to radiation damage. The insertion of the IBL will provide a insurance policy against such problems if they were to occur.

The main parameters of the IBL are described in table 1.1. Two sensor candidate are currently considered to build the IBL : Planar Pixel Sensor and 3D Silicon Sensors. The two technology require different module design, with a single chip module being used for 3D sensors while a double chip module is to be used with Planar sensors. A new readout chip has been developed to replace the FE-I3 used in the current ATLAS pixel modules. Table 1.2 show a comparison of the main characteristics of the two readout chip. The FEI4 can be distinguished by it larger size, smaller pixels, increased radiation hardness and occupancy performance. The timing resolution is kept at the same level as before but

the energy deposition measurement resolution is reduced from 8 to 4 bits. The reduction of the resolution was done to allow higher occupancy in the readout chip.

TABLE 1.1 – Main IBL layout parameters [9]

Parameter	Value
Number of staves	14
Number of modules per stave (single/double FEI4)	32/16
Pixel size (ϕ,z)	50,250 μm
Module active size WxL (single/double FEI4 modules)	16.8 x 40.8/20.4 mm^2
Coverage in η	$\|\eta\| < 3.0$
Overlap in ϕ between staves	1.82 degree
Center of sensor radius	33.25 mm
Sensor thickness	150-250 μm
Radiation length at z=0	1.54% of X_0

TABLE 1.2 – Comparison of FE-I4 and FE-I3 readout chip

Parameter	FE-I4	FE-I3
Technology	IBM 130nm	IBM 250nm
Pixel size (μm)	250x50	400x50
Nr. of Channel	26880	2880
Matrix dimension hline Time-Over-Threshold resolution	80 column sx 336 rows 4 bits	18 columns x 164 rows 8 bits
Timing resolution	25 ns	25 ns
Hit Buffer	32 per 4 pixels	64 per column pair

The IBL will be positioned at 3.325 cm of the interaction point and it will be required to replace the actual beampipe , located at a radius of 2,9 cm, by a new beampipe with a radius of 2,5 cm to liberate space to insert the IBL in the ATLAS pixel detector. Figure

The planar pixel sensor candidate for IBL was developed within the Planar Pixel Upgrade Group. Three model were developed, using recommendation from the simulation work presented in this thesis :

– Conservative n-in-n : ATLAS Standard sensor with a reduction of the guard ring by removal of the 3 outer guard ring to obtain the edge width of 450 μm required for IBL

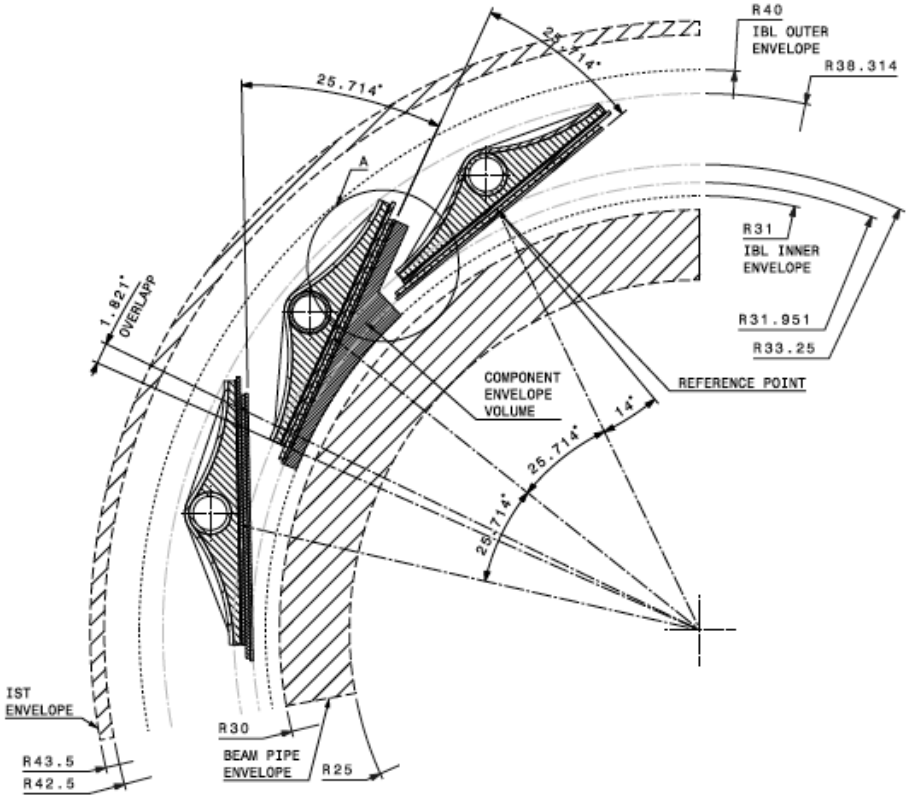

FIGURE 1.18 – IBL $r - \phi$ layout view

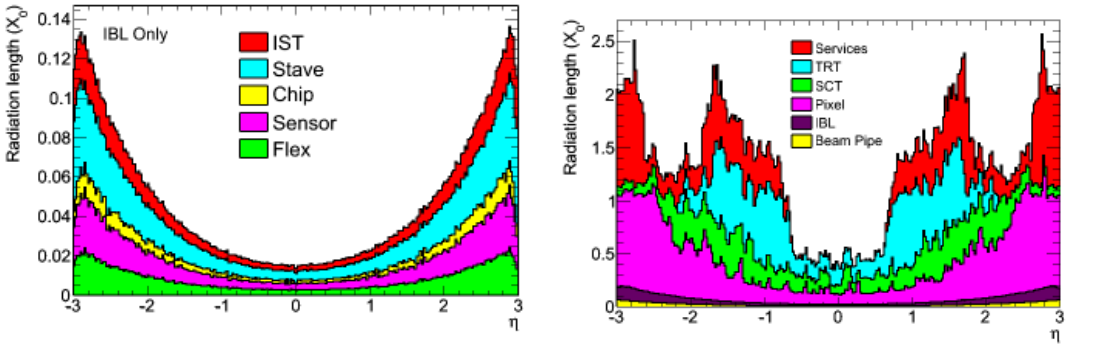

(a) IBL material budget

(b) FInner detector material budget (IBL included)

FIGURE 1.19 – Radiation length as a function of η in the IBL and inner detector

– Slim Edge n-in-n ATLAS sensor : ATLAS Standard sensor with 3 guard ring removed and guard ring shifted under the pixels to obtain an inactive edge of 100 μm.
– n-in-p sensor : Planar pixel sensor using a p substrate and a 450 μm reduced guard ring structure

Figure 1.20 shows the edge geometry for the three candidate. More details on the structure, their behavior and design will be given in the next chapters.

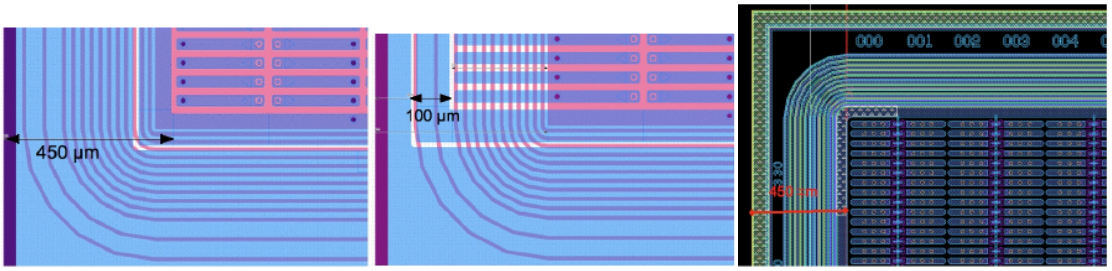

(a) Conservative n-in-n sensor (b) Slim edge n-in-n sensor (c) N-in-p sensor

FIGURE 1.20 – Planar pixel sensor candidates for IBL

1.3.2 Phase 2 : Upgrade for high luminosity

The phase two of LHC upgrade will require a completely new inner detector to survive luminosity and pile-up foreseen in LHC. The amount of radiation damage on the pixel sensors will increase by a factor 10 with regard to the current pixel detector which will not be able to cope with such occupancy and radiation damage. Research and development is now ongoing to design a new layout for the ATLAS super-LHC inner detector. Figure 1.21 shows the current accepted layout planned for the upgrade. The TRT is removed along with the whole actual inner detector and replaced by 4 layers of pixels, 3 layers of short strips and 2 layers of long strips [10].

Planar pixel sensor could be used for the SLHC pixel detector if it can yield enough signal at the $1 \times 10^{16} n_{eq} cm^{-2}$ fluence expected for the inner layer of the pixel detector. In chapter 3, a study of a new physical phenomenon observed in highly irradiated conditions has been performed to understand the physics mechanism behind the formation of collected signal in highly irradiated silicon sensors. The charge amplification can be explained by impact ionization current and trap-to-band tunneling in the bulk of the sensor and could

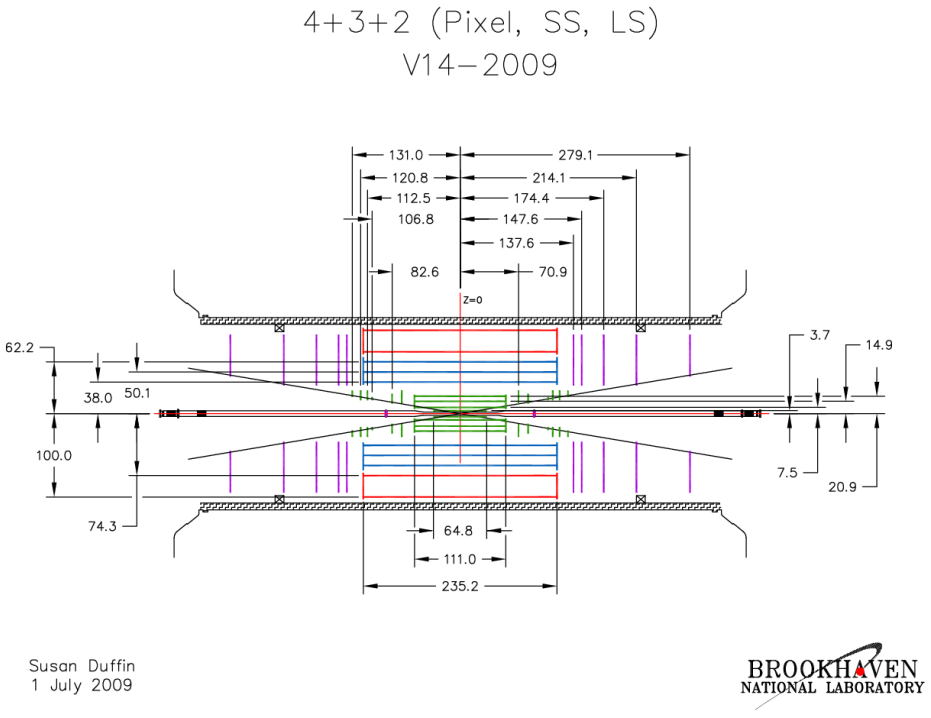

FIGURE 1.21 – ATLAS super-LHC inner detector planned $z - yi$ layout view

be used to design a new sensor able to survive the harsh environment of the SLHC ATLAS detector. The R&D done in the framework of the IBL upgrade also covers the needs of the SLHC detector and results presented in this work can also be applied to detectors in the SLHC environment,

Chapitre 2

Principles of Silicon pixel sensors

Silicon-based detector have been used for the last 60 years as an efficient mean to detect the presence of charged particles. Gold contact barrier, then p-n junction diodes were used between 1955 and 1965 as an efficient small size spectroscopic sensor to measure the ionizing energy deposition of β particles in silicon. The first HEP experiment to make a wide use of silicon as a tracking detector was CERN's NA11 and NA32 experiments [11]. The strip sensors used in their tracking system shown the possibility of large scale usage of these sensors in tracking applications in HEP.

Nowadays, the wide use of silicon diode based sensors allowed for the development of very sophisticated detectors used in large scale experiments where high resolution tracking of charged particles is required. Their increased exposure to radiation in high luminosity experiments due to their proximity to the interaction points remains a challenge as aging effects have been observed with increasing exposure to high energy particles. In this chapter I will describe the basic semiconductor physics behind the p-n junction based detectors and the mechanism that allow them to be used as efficient radiation detection devices. I will describe the ATLAS Hybrid planar pixel sensor which is the main study subject of this thesis. A quick survey of the concurrent technologies will be presented.

Finally, the physics behind the aging effects of silicon detectors due to exposure to radiation will be described. The empirical models developed in the recent years will be compared to the microscopic effects of radiation damage of silicon to provide an explanation of the behavior observed in irradiated silicon sensors.

2.1 The physics of Silicon

2.1.1 Semiconductors properties

Silicon used in particle detection is a semiconductor with a face-centered cubic crystalline structure, as shown in figure 2.1.

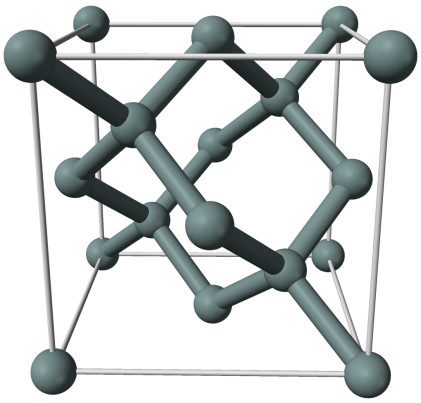

FIGURE 2.1 – Unit cell of silicon crystalline structure

The periodic nature of the silicon crystal lattice create the conditions for the electrons of the silicon atoms to arrange, in the energy-impulsion domain, in a band structure with forbidden zones where an electron cannot be found. This energy region where electrons cannot be found is called the bandgap. The height of this region is a unique property of each semiconductor.

The valence electrons of the silicons atoms are distributed between the conduction band and the valence band. The electrons in the conduction band are weakly bound to the lattice and can freely move through the material while the valence electrons are constrained to stay close the lattice structure. The Pauli exclusion principle forbids that two fermions, such as electrons, lie in the same energy-impulsion state. The energy distribution of this gas of fermions can be best described by the Fermi-Dirac distribution function (eq. 2.1) :

$$n_i = \frac{g_i}{e^{\frac{E_i - \mu}{k_B T}} + 1} \tag{2.1}$$

where g_i is the degeneracy factor of the energy state and μ is the Fermi-Dirac quasi-energy

level. At low temperature ($k_BT << \mu$), μ is the energy level under which all state are occupied. At high temperature ($k_BT >> \mu$),μ is the energy level over which a state has only a probability of 50% of being occupied. The Fermi-Dirac distribution at different temperature is shown in figure 2.2.

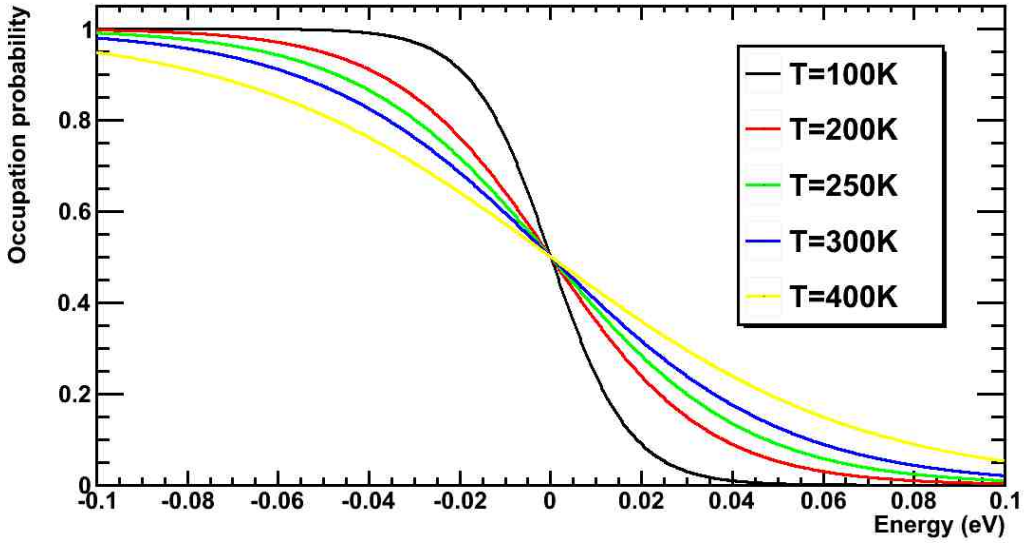

FIGURE 2.2 – Fermi-Dirac Distribution, $\mu = 0$, $g_i = 1$

This principle leads to the introduction of a virtual particle, the hole, as the carrier of the "absence of an electron" in the valence band of silicon. The addition of impurities to the crystalline structure modify the macroscopic properties of silicon. When impurities inserted in the crystal structure have a number of valence electrons (N_{ve}) different than 4, for silicon, extra electrons ($N_{ve} > 4$) or holes ($N_{ve} < 4$) are introduced in the band structure. The hole introducing dopant is called an acceptor and is found in p type silicon. The electron introducing impurities are called donors and are found in n type silicon. Both type of dopant can be present in silicon and will compensate each other in such way that only the net dopant concentration will be electrically active. In n type and p type semiconductors , the Fermi-Dirac quasi-energy level is found respectively close to the conduction or the valence band. The additional carriers will fill energy states not occupied in the intrinsic silicon modifying the position of the Fermi-Dirac quasi-energy level. At high

temperature typical of the operation of silicon sensors, most of the impurities additional carriers are added to the cloud of free carriers in the silicon crystalline structure, increasing the amount of carriers available for conduction. In highly doped silicon ($N_{D,A} > 10^{18} cm^{-3}$), the amount of additional carriers is such that energy levels in the valence band, for holes, or in the conduction band, for electrons, have a probability close or equal to 1 of being occupied. This lead to high conductivity of the material even at low temperature.

2.1.2 Charge transport

The dynamics of the carriers inside silicon can be described by the drift-diffusion equations (eq. 2.2 and 2.3) coupled to the Poisson (eq. 2.4) [12] :

$$\frac{dp}{dt} = \nabla \cdot D_h \nabla p + \nabla \cdot (p \mu_h \vec{E}) + G_h - R_h \tag{2.2}$$

$$\frac{dn}{dt} = \nabla \cdot D_e \nabla n - \nabla \cdot (n \mu_e \vec{E}) + G_e - R_e \tag{2.3}$$

$$-\nabla^2 V = \nabla \cdot \vec{E} = \frac{\rho}{\epsilon} \tag{2.4}$$

where p and n are respectively the density of holes and electrons in $[\frac{1}{cm^3}]$, D in $[\frac{cm^2}{s}]$, their respective diffusion coefficient, μ the mobility in $[cm^2/V/s]$. G is the generation rate and R, the recombination rate, both in $[1/cm^3/s]$. The h and e subscript respectively design holes and electrons. ρ is the net charge density in $[C/cm^3]$, where C are Coulomb.

Generation/Recombination terms are important to describe the behavior of silicon detectors. Generation is responsible for leakage current present in detectors under bias. Recombination occurs between free carriers and its rate is proportional to the concentration of the most rare carrier. Silicon being an indirect gap semiconductor, generation and recombination occurs mostly through the defect states that are present in the bandgap of Silicon.

2.1.3 The pn junction

When two regions of silicon containing different concentration of free carriers are put into contact, we form a junction if the two region are respectively of p and n type. At the contact region, the excess holes and electrons present create an electric field dragging free carriers on the other side of the junction . A space-charge region is created at the junction where the electric field is present. The rate of carriers entering the space-charge region by diffusion from the doped region is equal to the rate of carriers leaving this region by drifting in the electrical field built by the difference of carrier concentration on each side of the junction. A zone with very low concentration of free carriers that is created at the junction is called the depletion zone. The only free carriers present are coming from the thermally generated carriers created to replace the carriers drifting away in the electric field. The application of an additional electric field through electrodes in contact with each side of the junction will modify this equilibrium by dragging carriers from the doped regions away or within the junction and modify the width of the depletion zone.

The pn junction can be biased in two different manners, as illustrated in figure 2.3. If a negative voltage is applied on the n side and a positive voltage on the p side of the junction, the depletion zone tends to shrink and the electric field in the depletion zone is reduced, allowing more charge to cross the potential barrier and diffuse in the opposite side of the junction. This results in a reduction of the apparent resistance of the pn junction and a non-linear exponentially increasing current. In the opposite case , the depletion region will expand away from the junction and the electric field increases as the amount of space charge becomes more important. The only current flowing through the junction is the diffusion current from each depletion region edges, which saturates with distance, and the generation/recombination current from the depletion region.This result in an apparent increase of the resistance of the pn junction and results in a saturation of leakage current. Figure 4.21 show the typical Current versus bias of a pn junction.

The depleted zone in reverse bias mode represent the volume where particle energy deposition can be detected as carriers generated through this process can drift into the electric field and generate a signal. The width of the depletion zone can be calculated using

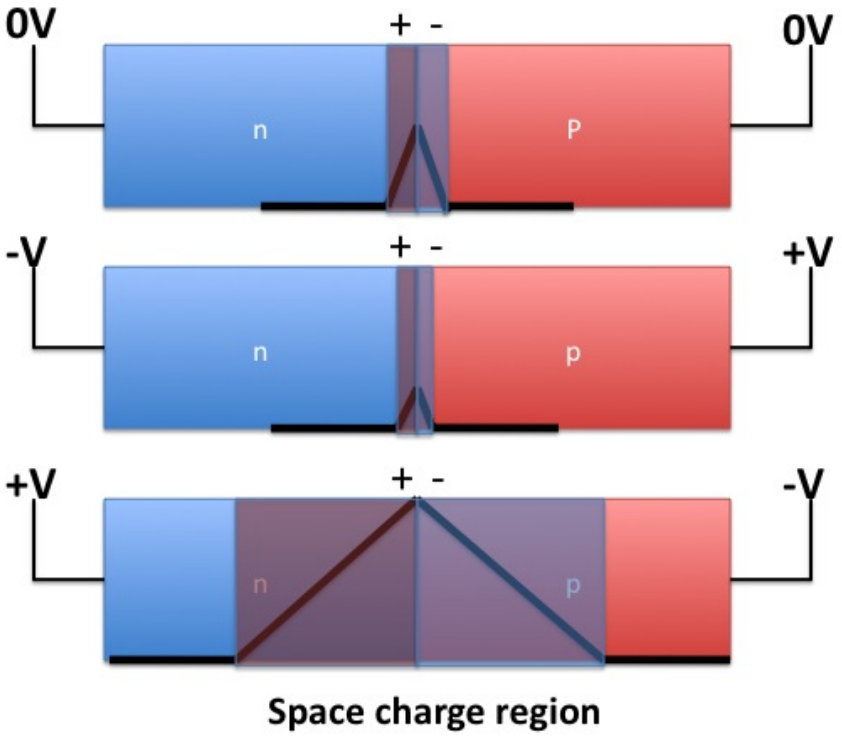

FIGURE 2.3 – The three possible state of a pn junction : at rest (top), forward bias (middle), reverse bias (bottom). The depletion region relative size is shown on the figure with the space-charge sign of each zone of the diode.

equation 2.5 [13].

$$d = \sqrt{\frac{2\epsilon V}{eN}} \tag{2.5}$$

Where ϵ is the electrical permittivity in silicon, V the applied bias voltage, e the electron charge and N the dopant concentration in the region where dopants are less concentrated. Dopant concentration can be linked to sensor resistivity using equation 2.6, details of the calculation are given in the annex.

$$\rho = \frac{1}{eN_{D,A}\mu n, p} \tag{2.6}$$

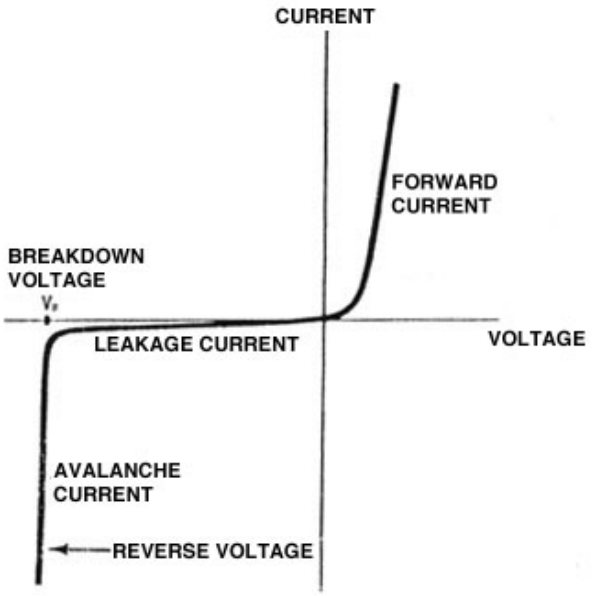

FIGURE 2.4 – Typical pn junction current versus bias characteristics.

Where $N_{D,A}$ is the donor or acceptor effective concentration.

2.1.4 Physical models

In order to simulate correctly the behavior of silicon detectors, the generation and recombination terms of the drift-diffusion equations, mobilities of the carriers, oxide-silicon interface and metal silicon interface physics must be correctly modeled. The dependence of models on electric field magnitude, temperature, dopant concentration must be taken into account correctly to obtain an accurate and quantitative simulation of a device.

2.1.4.1 Generation-Recombination

The rates of generation and recombination of thermally generated carriers are described by the modified Shockley-Read-Hall equation ([12]), which describes the generation-recombination in indirect-band gap semiconductors such as silicon. This model assumes that the transition of carriers between bands occurs through a single trap energy level

located deeply in the gap, E_{trap}.

$$R_{SRH} = \frac{pn - n_i^2}{\tau_p[n + n_i e^{\frac{E_{trap}}{k_b T}}]\tau_n[p + n_i e^{\frac{-E_{trap}}{k_b T}}]} \tag{2.7}$$

$$\tau_n = \frac{\tau_{n0}}{1 + \frac{N_{dopant}}{N_{SRHn}}} \tag{2.8}$$

$$\tau_p = \frac{\tau_{p0}}{1 + \frac{N_{dopant}}{N_{SRHp}}} \tag{2.9}$$

Equation (2.7) gives the Concentration-Dependent Shockley-Read-Hall Generation-Recombination model used in our simulation, where (2.8) and (2.9) explicit the concentration dependence. $\tau_{p,n}$ are the recombination lifetime for holes and electrons, $\tau_{n0}, \tau_{p0} = 10^{-5}\ s$ a material dependent parameter representing the recombination lifetime for low dopant concentration bulk, $N_{SRHp,n} = 5 \times 10^{16}\ cm^{-3}$ a material dependent empirical parameters and N_{dopant} the dopant concentration. The user dependent parameters must be chosen to represent the bulk material simulated. The values presented here were selected to represent a typical high resistivity bulk used for particle detectors that are not pure crystals. The presence of oxygen and other impurities affects its electrical properties. Dopant are also introduced during fabrication of the sensors whereas defects are introduced by high energy particles crossing the sensor. In the super-LHC environment , ATLAS inner tracker will be exposed to high level of radiation and the large introduction of structural defects must be taken into account in the design of the sensors. More sophisticated simulations of bulk properties like leakage current requires a more complex description of generation-recombination mechanisms.

Our simulation of irradiated sensors use the modified Shockley-Read-Hall Generation-Recombination model, which can take into account the presence of multiple trap levels in the band gap, introduced by radiation or native defects. Generation-Recombination terms for each trap are calculated using (2.7) and a global term R_{total} is calculated following

(2.10).

$$R_{total} = \sum_{\alpha=1}^{l} R_{D_\alpha} + \sum_{\beta=1}^{m} R_{A_\beta} \tag{2.10}$$

$$\tau_{n,p} = \frac{1}{N_t v_{th,n,p} \sigma_{n,p}} \tag{2.11}$$

l and m are the numbers of donors and acceptors traps,$R_{A,\beta}$ $R_{D,\alpha}$ the Generation-Recombination terms for respectively acceptors and donors traps. The density of traps N_t is taken into account through the parameters τ_n and τ_p used for each trap level, as shown in (2.11) .

Finally, charge states of traps are taken into account in Poisson equation right term. The amount of ionized trap is determined using Boltzmann statistics. This complex model take into account the variation of the effective doping density and temperature dependence and model correctly the contribution of thermally generated carriers of generation-recombination term of the transport equations. However, the presence of an intense electric field ($O(100kVcm^{-1})$) alter the bandgap structure of silicon and enhance the generation and recombination of carriers.

The electric field presence causes a bending of the bandgap structure in space, lowering the potential barrier faced by carriers to cross to or from the traps present in the bulk material, as shown in figure 2.5.

This affects the lifetime of electrons and holes trapped in the defects in the band gap of silicon. An increased electric field in the bulk of the sensor will bend the band gap of silicon modifying the energy level of the conduction and valence band between different space points. If this bending is sufficient, tunneling of the carriers trapped in the defects to the valence or conduction band can occur, reducing the effective lifetime of the trapped carrier and contributing to the leakage current and thus to the generation rate term of the drift-diffusion equations. This physical phenomenon is called trap-to-band phonon-assisted tunneling. A large amount of defects are present in irradiated silicon and high voltage operation is needed to obtain charge collection recovery. A model elaborated and introduced in our simulation is described in details in [14]. In this model, trap lifetime of

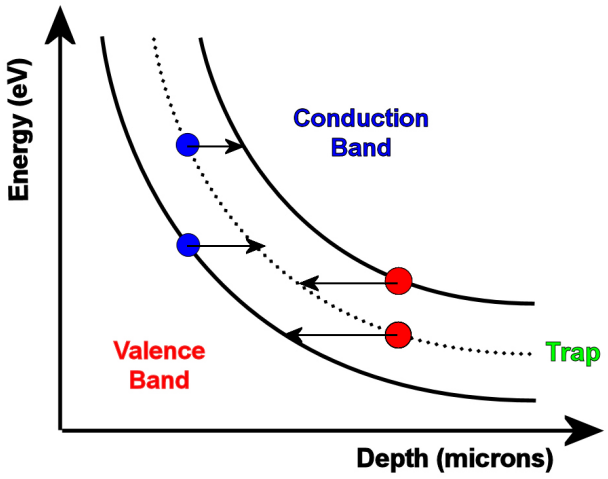

FIGURE 2.5 – Schematics of bandgap bending due to electric field and how it enhance the tunneling between traps and the bands.

the generation recombination terms of equation 2.8 and 2.9 is modified following equation 2.12

$$\tau_{p,n} = \frac{\tau^0_{p,n}}{1 + \Gamma^{Dirac}_{p,n}} \tag{2.12}$$

$$\Gamma^{Dirac}_{p,n} = \frac{\Delta E_{p,n}}{k_b T} \int_0^1 e^{(\frac{\Delta E_{p,n}}{k_b T} - K_{p,n} u^{3/2})} du \tag{2.13}$$

$$K_{p,n} = \frac{4}{3} \frac{\sqrt{2 m_0 m^* \Delta E^3_{p,n}}}{2 q \hbar E} \tag{2.14}$$

Where $\tau^0_{p,n}$ is the trap lifetime without electric field, $\Delta E_{p,n}$, the trap to band energy difference, m_0 the effective carrier mass, $m^* = 0.15$ the effective tunneling mass of the carrier, q the elementary charge, $\hbar$ the planck constant and E the local electric field magnitude.

Figure 2.6 shows the typical trapped charge lifetime dependence on electric field following the model introduced to the simulation. As the time scale of the charge drift in silicon sensors is $O(10\ ns)$ this effect can be important for the charge collection in irradiated sensors operated at high bias voltage. The effect of trap-to-band tunneling is taken into account in transient simulation by affecting the terms of equation 2.29

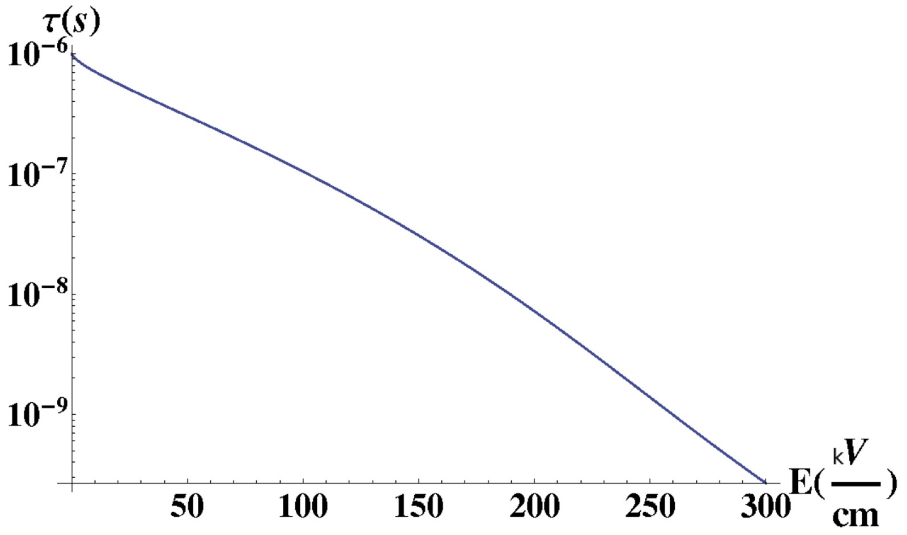

FIGURE 2.6 – Trapped charge lifetime dependence on electric field, $E_{trap} = E_c - 0.53\ eV$

The presence of an intense electric field in the bulk of silicon will lead to acceleration of carriers and generation of additional electron hole pairs by energy transfer from the accelerated carrier to the lattice electrons by coulombian scattering. This effects lead to breakdown of silicon sensors and must be modeled to reproduce this behavior in simulation. A model of impact ionization has also been implemented in the generation rate of the drift-diffusion equation. This model is the Selberherr Impact ionization model [15]. Equation (2.15) shows the relation used to obtain the generation rate contribution from impact ionization, with the electric field dependence detailed in equation (2.16).

$$G_{impact} = \alpha_n(\vec{E}) \left|\vec{J_n}\right| + \alpha_p(\vec{E}) \left|\vec{J_p}\right| \tag{2.15}$$

$$\alpha_{n,p}(\vec{E}) = A_{n,p} e^{-\frac{B_{n,p}}{\vec{E}}} \tag{2.16}$$

Coefficients $A_{n,p}$ and $B_{n,p}$ are determined experimentally and are chosen as a function of the material. Fig. 2.7 shows the electric field dependence of the impact ionization coefficient α_n. If the electric field inside the irradiated sensor bulk reaches a magnitude of the order of 100 $kVcm^{-1}$, some multiplication effects leading to increased leakage current are to be expected.

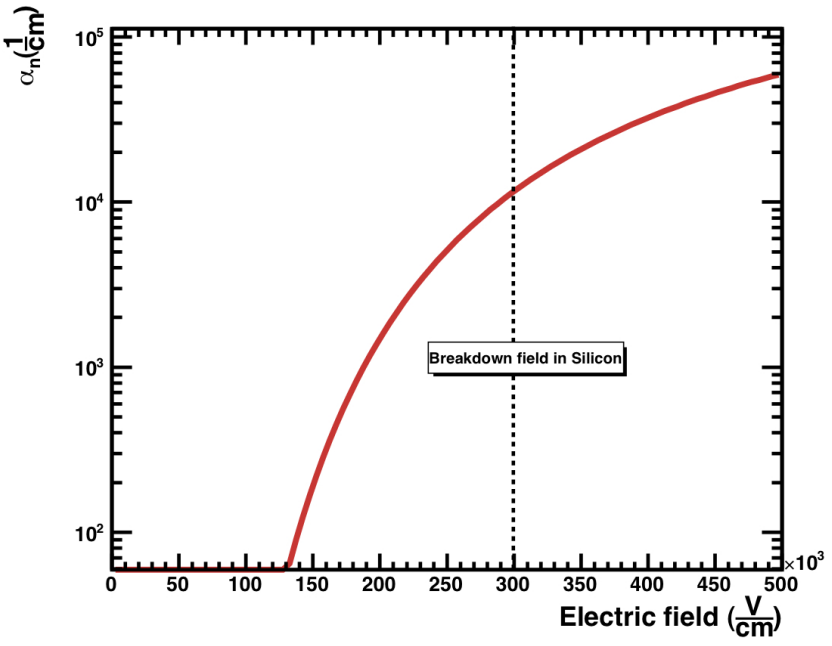

FIGURE 2.7 – Impact generation coefficient α_n dependence on electric field magnitude

2.1.4.2 Mobility

Mobility of charge carriers in silicon is influenced by the magnitude of the parallel electric field in which it is drifting. In a high electric field, free carrier's energy loss by inelastic scattering in the crystal lattice will balance with the energy gained from acceleration in the electric field. This leads to the saturation of the carrier's speed [12]. This effect can be expressed in terms of a variation of the mobility (μ) as a function of the parallel electric field magnitude [16]. Equation 2.17 and 2.18 show the typical expression used to model the parallel field dependence of mobility in Silicon.

$$\mu(E) = \mu_0 \left(\frac{1}{1 + \left(\frac{\mu_0 E}{v_{sat}}\right)^{\beta}}\right)^{-\beta} \tag{2.17}$$

$$v_{sat} = \frac{\alpha}{1 + \theta e^{\frac{T_L}{T_{nominal}}}} \tag{2.18}$$

Where T_L is the lattice temperature. Typical values used for this model are shown in

table 2.1.

TABLE 2.1 – Parallel field dependence mobility model parameters

Parameter	Electrons	holes
μ_0 $(cm^2/Vs\ at\ 300K)$	1400	450
β	2.0	1.0
α (cm/s)	2.4×10^{-7}	2.4×10^{-7}
θ	0.8	0.8
$T_{nominal}$ (K)	600	600

2.1.4.3 Magnetic field effects

Semiconductors sensors for particle tracking application are often used in a magnetic field to allow the measurement of the transverse momentum of incoming particles. While the presence of a field modify the behavior of the detectors, they can be operated in intense magnetic field without hurting the detector performances. The carriers inside the magnetic field are subject to the Lorentz force (equation 2.19), where is the velocity of the carrier and B the magnetic field intensity.

$$\vec{F} = q(\vec{E} + v \times \vec{B}) \tag{2.19}$$

The additional component of the force due to the magnetic field presence leads to carriers drifting away from the electric field lines with an angle determine by equation 2.20 [17], where *theta* is the angle between the electric field and the actual carrier drift trajectory and $\mu^H_{p,n}$ is the Hall mobility, which differs from normal mobility because of the effects of the presence of the magnetic field.

$$tan\theta_{p,n} = \mu^H_{p,n} B \tag{2.20}$$

2.2 Radiation detection

2.2.1 The energy deposition process

The reverse bias operation mode of the silicon pn diode presents interesting characteristics for charged particle and x-ray detection. The radiation interacting with silicon diodes through ionizing process such as photoelectric effect, Compton scattering and through transfer of energy to the bound carriers by coulombial scattering generate an amount of free carriers in electron-hole pairs, proportional to the amount of energy deposited in the diode through these ionizing processes. The mean amount of carriers generated in such process ($N_{e,h}$) is given by eq. 2.21 where E_d is the deposited energy and E_g is the pair production energy, 3.64eV for silicon.

$$N_{e,h} = \frac{E_d}{E_g} \tag{2.21}$$

The pair production process is an almost stochastic one, but the pair production process is not independent from pair to pair as the energy deposition occurs in a cascade of energy transfers from the incoming particle to the carriers and from excited carriers to other carriers. This correlation between the different pair production events gives rise to the Fano factor (F=0.118 for silicon [18])in the intrinsic energy resolution equation (eq. 2.22) of semiconductor sensors to account for the lower standard deviation observed with regard to the Poisson predicted standard deviation.

$$\sigma_{Si} = \sqrt{FN_{e,h}} \tag{2.22}$$

In a silicon diode used as a particle sensor, a diode is biased and the depleted region represents the active detection region. A particle deposit its energy and a cloud of electron-hole pairs are created. Following the electric field, they drift toward the electrodes generating an additional current in the diode that can be measured using detection electronics, as shown in figure 2.8.

The low reverse biased diode leakage current represent an advantage of silicon sensors. This leakage current is caused by electron-hole pairs being thermally generated in the the

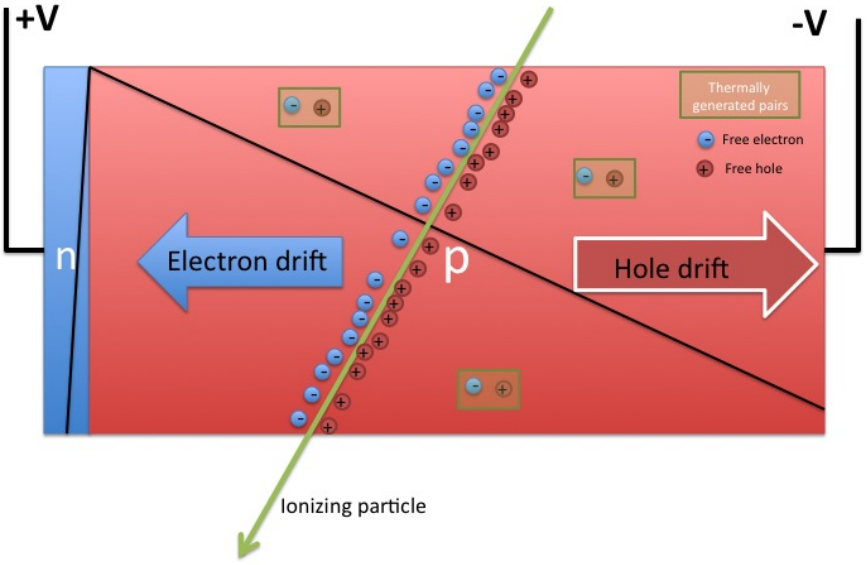

FIGURE 2.8 – Schematics of ionizing particle detection in a reverse biased diode. The free electron hole pairs produced by the particle energy loss drift in the electric field and produce a current in the diode. Thermally generated (green boxes) are also generated in the depleted zone of the diode.

depleted zone of the diode. These pairs also induce signal on the read-out electrode and are emitted randomly thus subject to statistical variations. This increases the noise in the sensor and low leakage current present in reverse-biased diodes makes it a perfect detection medium for ionizing radiation.

2.2.2 Signal formation

The signal induced on a readout electrode is not due to the collection of the free carriers themselves. The charge's electric field flux inside the readout electrode varies as the charge drift into the sensor and displacement current is created and generate the detectable signal. The real signal can be calculated using the Ramo theorem [19], as shown in 2.23.

$$Q_k = \sum_i q_i \phi_k(\vec{r_i}_{final}) - \sum_i q_i \phi_k(\vec{r_i}_0) \tag{2.23}$$

Where Q_k is the charge induced on electrode k, q_i is the charge of the carrier i, $\vec{r_i}$ its

position and ϕ_k the Ramo potential of electrode k. The Ramo potential is calculated by solving the Laplace's equation in the geometry of the detector while imposing a Dirichlet boundary condition at the electrodes, with $\phi = 1$ at the k'th electrode and 0 at the other present electrode and a Neumann boundary condition ($\vec{\nabla}\phi \cdot \vec{n} = 0$, $\vec{n}$ is the vector normal to the boundary) at the rest of the boundaries. This theorem can be applied to a variety of detection medium ranging from plasma to solid-state detectors. The presence of space charge do not influence the calculation of the Ramo potential [20; 21]

2.3 The Hybrid Planar Pixel Sensor

The planar pixel sensor (figure 2.9) consists of an array of small rectangular diodes built by implanting dopant in a Silicon wafer to form junctions. A structure of guard rings is disposed around the array of pixels to insure a smooth transition of the surface bias potential from the active area to the edge of the sensor. Each of the concentric rings is self-biased with the inner ring taking the pixel or backside electrode potential and the outer ring taking the edge potential, usually the same as the verso of the edge. Details on the guard ring structure will be given in chapter 3. Lithography methods are used to create the individual pixels diodes and contact electrode. An implant and a metallization on the backside of the wafer is created with a dopant type opposite of the pixel's implant type. This create an ohmic contact. Bias is applied between each side of the wafer to deplete the sensor and create an electric field in the bulk of the sensor allowing the drift of free carriers generated by ionizing particles. The carrier cloud generated is localized in a small region around the particle track allowing to measure the particle position in the sensor using signal induced on the individual pixels. An integrated circuit, called a front-end, is also built with individual cells of signal lecture and digitization electronics matching the pixels on the planar sensor. The integrated circuits individual channels are coupled to the diodes using the bump-bonding technique. Each channel can then be read individually in a digital format to obtain the information on the position and energy of the detected particles. The assembly is then mounted on a PCB or a Flex-Hybrid containing the circuits to bias the sensors and the integrated circuits and readout and transmit the acquired data. The final assembly is call hybrid Planar pixel sensor module and can be used to form large system

of particle tracking used in large HEP experiments such as ATLAS.

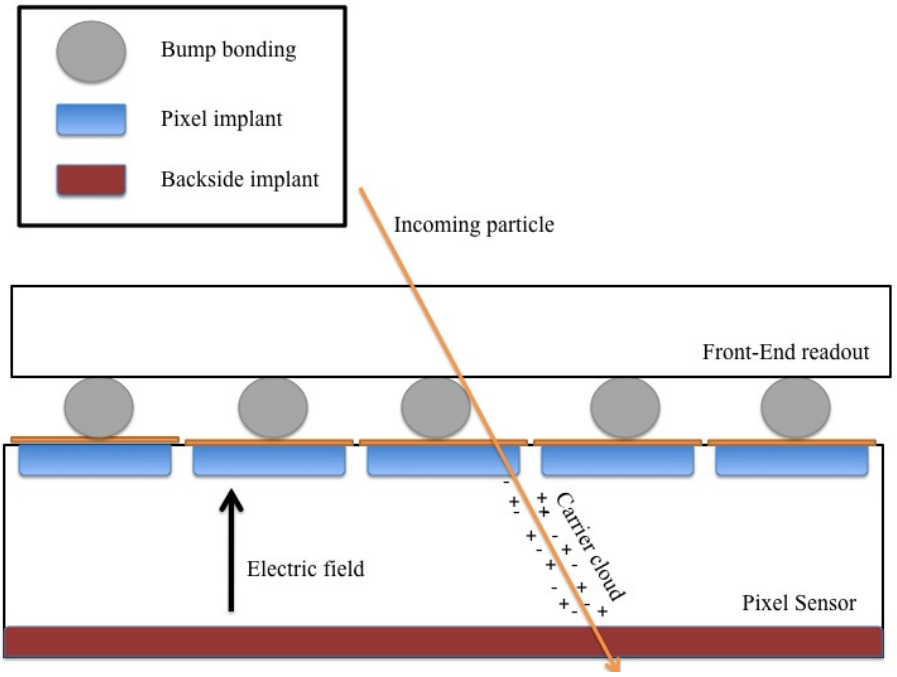

FIGURE 2.9 – Schematics of the hybrid planar pixel sensor.

Planar pixel sensors can be used in 4 configuration of implants and bulk with each their advantage and inconvenient. Figure 2.10 describe the possible geometries of pixel and guard ring that are suitable for pixel sensors.

The electrode readout implant type is chosen to select the main signal carrier of the sensor. N implant are used for readout of electrons which travel faster is silicon due to their higher mobility. They are favored for radiation hard sensor as they are less prone to trapping. Bulk type is chosen as a function of desired guard ring side and radiation hardness issues. As N type bulk invert to P type-like bulk and depletion voltage rise after irradiation due to space charge sign inversion, the depleted zone, which expands from the pn junction side towards the other junction, could not be maintained for p-in-n and p-in-p sensors when depletion voltage gets to high for the power supply. For n-in-n sensors, space charge sign inversion is actually beneficial as the detector is always depleted under the readout electrodes. Before inversion, depletion voltage is reduced with regard to the initial value hence the sensor can always be fully depleted. N-in-p sensors are unaffected by this

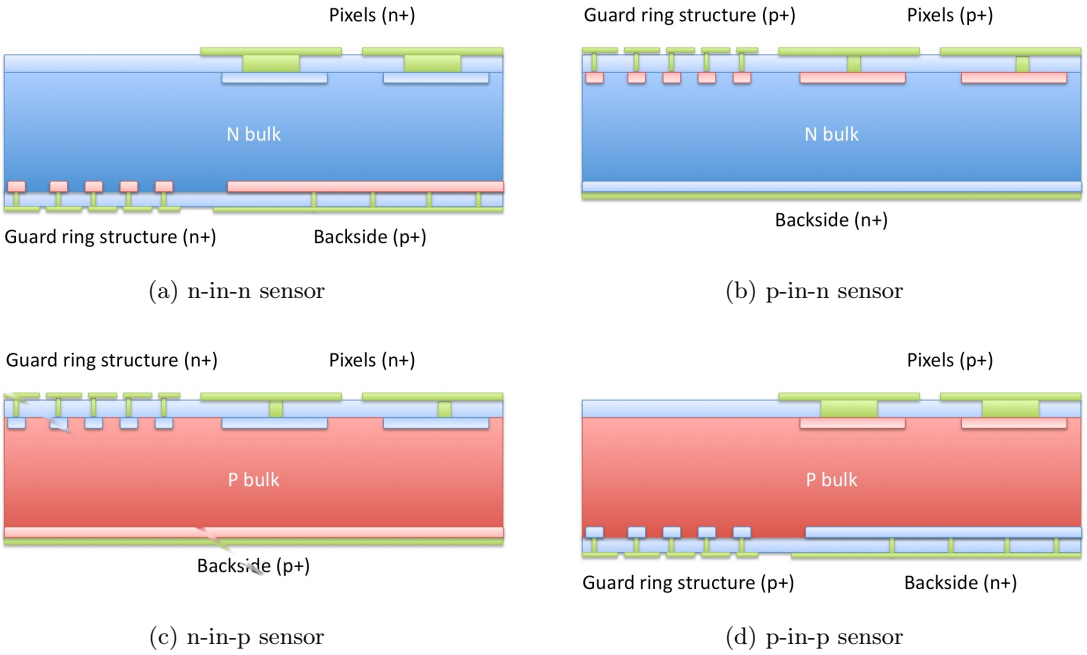

(a) n-in-n sensor

(b) p-in-n sensor

(c) n-in-p sensor

(d) p-in-p sensor

FIGURE 2.10 – Schematics of the possible pixel sensor implant and bulk configurations.

as the depletion always occurs from the pixel side of the sensor. Finally, the guard ring, to be functional, must be located on the pn junction side of the sensor. In the n-in-p and p-in-n sensor case, this mean some high voltage, coming from the backside, will be present in the guard ring region and might be detrimental to the chip also located on the readout electrode side. However, in the case of these detector, all lithography to build the electrode structure is located on the same side of the wafer, reducing the fabrication cost of the detectors. Table 2.2 summarized the characteristics of each configuration.

The ATLAS pixel detector is built with n-in-n planar pixel sensors. This technology was chosen for it many advantages and is the planar pixel sensor candidate technology for the Insertable b-layer.

2.4 Other Silicon sensors

In the recent years, new technologies have been developed to build pixel sensors for particle detection. The goal of these new technologies is to increase the signal formation speed, reduce inactive zones of the sensor, build thinner sensor and increase radiation hardness

TABLE 2.2 – Summary of planar pixel sensor configurations

Sensor Type	Advantages	inconvenients
n-in-n	– electron signal – inversion of depletion direction after SCSI – guard rings on backside	– double-sided process
n-in-p	– electron signal – no SCSI – single-sided process	– guard ring on pixel side
p-in-n	– single-sided process	– guard ring on pixel side – hole signal – hard to fully deplete after SCSI
p-in-p	– no SCSI – guard rings on backside	– hole signal – hard to deplete with increasing radiation – double-sided process

for applications where such characteristics are required. The two main new technologies are the 3D pixel sensor and the High Resistivity Monolithic Active Pixel Sensor (MAPS).

2.4.1 the 3D pixel sensor

The main difference between the planar pixel sensors and the 3D variety is the orientation of the electrode implant in the wafer. Through chemical etching techniques, deep holes are created in the wafer and implants are created on the surface of the holes, forming p-type and n-type columns in the wafer. They are then filled with a conductive material to form the anodes and the cathodes. The bias is applied between the two type of columns and drift of the carriers occurs laterally, as shown in figure 2.11. For sensors with a pixel pitch smaller than the wafer thickness, this leads to a faster signal and smaller depletion voltage. The possibility to bias literally avoid the problem of high voltage distribution at edges present in planar pixel sensors, discussed in chapter 3 of this thesis, allowing for small inactive edges. Finally , the short drift distances of the carriers reduce the signal loss due to trapping during long charge drift makes the 3D sensors more radiation hard by design, since, as it will be discussed in the next section of this chapter, radiation damage induced charge loss by trapping of carriers in discrete energy levels present in the band-gap of the sensor's material.

2.4.2 High Resistivity Monolithic Active Pixel Sensors (MAPS)

MAPS sensors are built on a single high resistivity silicon wafer where a low resistivity silicon layer have been grown by epitaxy. A small subsection of the pixel surface is occupied by a detection diode depleting in the high resistivity buried layer, while the rest of the surface is occupied by CMOS electronics in the low resistivity bulk, forming the readout electronics of the diode, as shown in figure 2.12. A small electric field is present in the depleted region and a small signal is generated in the detection diode. The signal is then amplified and digitize on the same wafer by the readout electronics. The presence of the amplifier so close to the detection diode allows low noise operation even with the small signal produced by the passage of a particle. The presence of the electronics on the same wafer used for detection eliminated the need for a front-end integrated circuits and the

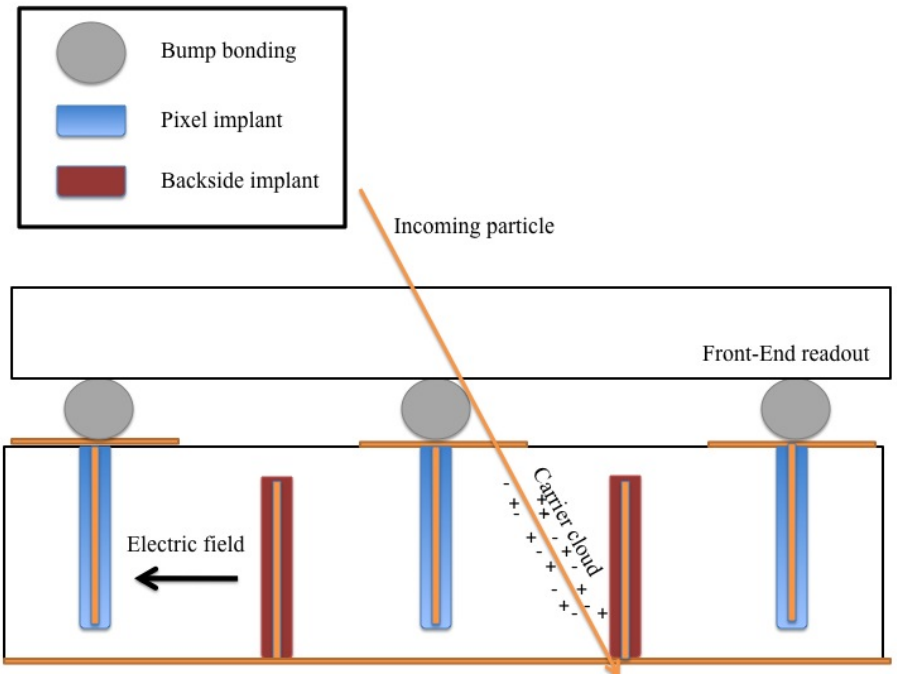

FIGURE 2.11 – Schematics of the hybrid 3D pixel sensor.

small thickness of the epitaxial layer and detection layer (down to 50 μm) allows to build very thin sensors for low material budget applications.

2.5 Radiation damage in Silicon sensors

Silicon sensors can be damaged by the exposure to radiation. Several effects need to be taken into account to design radiation hard sensors for use in harsh environment such as in ATLAS inner detector. Two kind of radiation damage are important in the case of silicon sensors : Non-ionizing and ionizing energy loss by particles interacting with the sensor's material. Each effect lead to specific changes in the sensors operation conditions and electrical characteristics.

2.5.1 Non-ionizing Energy Loss (NIEL)

Exposure of planar pixel sensor to non-ionizing energy loss from protons, pions and neutrons modify its electrical properties in the following ways :

– Space-Charge Sign Inversion (SCSI)

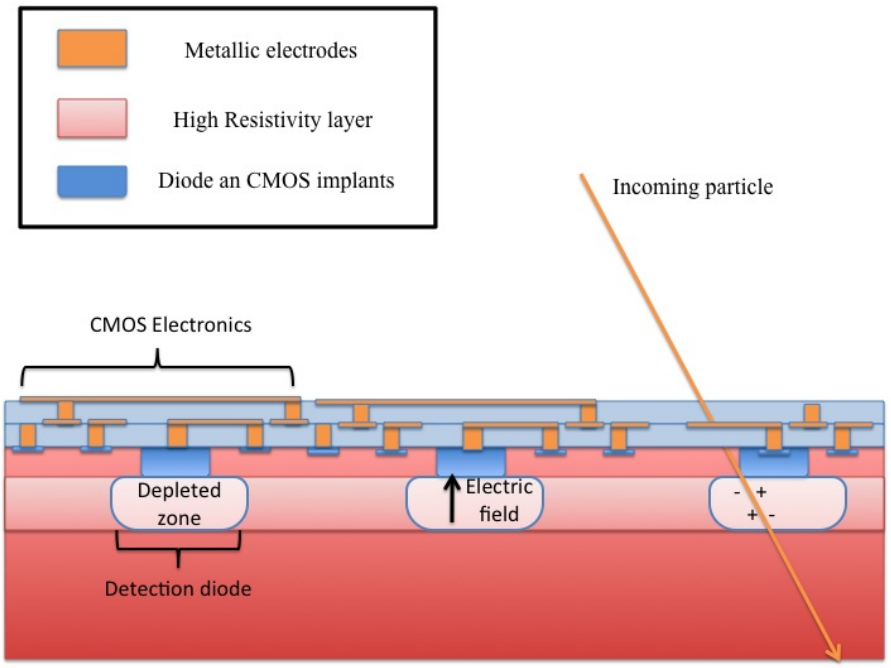

FIGURE 2.12 – Schematics of the High Resistivity Monolithic active pixel sensor (MAPS).

– Modification of full depletion potential (V_{fd}) (high voltage operation after high-dose)
– Increased trapping
– Leakage current increase

NIEL is usually expressed, for silicon sensors, in 1 MeV neutron-equivalent by square centimeter, (n_eq/cm^2). The energy loss by exposure to different particle types and energies can be calculated by scaling the flux of the incoming particle on the sensor surface by the ratio between the NIEL in the bulk for that particle and the NIEL for a 1 MeV neutron. A large number of publication measuring the NIEL scaling factor for various type of particle is available in the litterature.

SCSI effect was first predicted then measured experimentally [5; 6]. It is expressed through an inversion of the space charge sign in the depleted region of silicon sensors. This inversion has been shown to be due to the introduction of electrically active defects in the bulk that compensate for the natively present defects. This leads to an apparent change of the bulk type, changing the wafer side where the high electric field is present and eventually leading to a complex distribution of space charge in the bulk leading to the formation of

a high field region on both side of the silicon wafer ($N^+ - p - n - p^+$ structures). From equation 2.5, we can observe that an apparent charge in the bulk's acceptor or donor net quantity will also lead to a variation of the depletion voltage needed to fully deplete the silicon sensor. The steady introduction of these electrically active defects will eventually lead to an increase of the need depletion voltage and may limit the capacity to deplete the sensor completely.

Signal carriers are subject to recombination with the same probability as thermally generated carriers. The introduction of defects in the bulk will lead to a lower characteristic recombination time of the free carriers through these defects. If this time is of the order, or lower than expected collection time, it will lead to a reduction of the collected charge with regard to the expected value before the introduction of the defects. This radiation damage effect will lead to lower detection efficiency, reduced resolution, lower signal to noise ratio and will force frequent recalibration of the sensor's readout electronics.

Finally, the traps in the band-gap are possible mediator for generation and recombination of carriers in indirect band-gap semiconductors. The addition of new trap in the sensor material will then lead to an increased probability of thermal emission of carriers leading to an increased leakage current. This represent an issue reducing the detector performance by increasing the noise and can lead to cooling problems and thermal runaway as the dissipated energy becomes more important. Finally, if the current leaking through the sensor is too important for the front-end readout out current compensation circuit capacity , it can lead to non-linear behavior of the electronics reducing the detector overall performances.

For a trap t, introduced by radiation or present in the original detector material, four processes can be enhanced : hole capture (R_h^t), hole emission (G_h^t), electron capture (R_e^t) and electron emission (G_h^t). Equations 2.24,2.25,2.26 and 2.27 ([17]) show the rate of each these processes as a function of the trap's capture cross-section ($\sigma_{p,n}^t$), thermal velocity (v_{th}), trap density (N_t), free carrier concentration (p, n),hole or electron emission probability ($\epsilon_{p,n}^t$) and occupancy of the trap (P_t).

$$R_h^t = v_{th,p}\sigma_p^t p N_t P_t \tag{2.24}$$

$$G_h^t = v_{th,p}\epsilon_p^t N_t(1 - P_t) \tag{2.25}$$

$$R_e^t = v_{th,n}\sigma_n^t n N_t(1 - P_t) \tag{2.26}$$

$$G_e^t = v_{th,n}\epsilon_n^t N_t P_t \tag{2.27}$$

At equilibrium, the sum all recombination and generation rates must equal 0 (equation 2.28). In this state, some concentration of defects can remain charged and modify the space charge distribution in the sensor, as seen in the SCSI effect. An increased trap density lead to bigger generation term and higher leakage current in reverse biased diode where recombination terms are kept low due to low free carrier density.

$$\sum_t G_{e,h}^t = \sum_t R_{e,h}^t \tag{2.28}$$

During collection time in the depleted zone of a reverse biased diode where carrier density is low, a quasi-static approximation, as shown in equation 2.29 can be used to determine the behavior of the signal's carriers during charge collection. This model supposes no carriers exchange between the different defects present, which is a valid approximation if defect density is low. The localized higher carrier density (n, p) in the charge cloud generated by the energy deposition of a particle, recombination terms are enhanced and lead to trapping of the signal if a large density of trap is present. A radiation damage increase, more trapping will occur and lead to lower charge collection efficiency.

$$\frac{dn, p}{dt} = \sum_t G_{e,h}^t - \sum_t R_{e,h}^t \tag{2.29}$$

For a distribution of carriers drifting in a reverse biased diode, one can compute the current induced on an electrode w using Ramo's field ($\vec{\Phi}_w$), as a function of genera-

tion/recombination rate, as shown in equation 2.30.

$$I_w(t) = \int_{volume} \rho(\vec{x}, \sum_t R^t_{e,h}(\vec{x}), \sum_t G^t_{e,h}(\vec{x}))\vec{\nabla}\Phi_w d\vec{x} \tag{2.30}$$

This equation is however complex to solve and one can approximate the collected charge by supposing a uniform distribution of traps, a constant electrical field and a punctual charge, neglecting generation of carriers. The recombination rate of the traps can be then expressed in term of the trap characteristic lifetime ($R_e, h = 1/\tau_t^{e,h}$). An average characteristic lifetime can be calculated using equation 2.31 and the collected charge can be expressed using equation 2.32.

$$\frac{1}{\tau} = \sum_t \frac{1}{\tau_t} \tag{2.31}$$

$$Q_f = \int_{t_0}^{t_f} Q_0 \mu_{e,h} \vec{E} e^{-t/\tau} \vec{\nabla}\Phi_w(Q_0 \mu_{e,h} \vec{E} t) dt \tag{2.32}$$

The hadronic interactions of particles with the atoms of the crystal lattice transfers to them part of their kinetic energy and displaces them from their original position, creating disorder in the crystalline structure. The displaced atoms can be moved to interstitial space in the lattice, forming a defect, called interstitial defect, than can become electrically active and modify the band structure of the silicon. The vacancies in the lattice left by the knocked-off atom can also create an electrically active defect called the vacancy defect.

Moreover, the pre-exisisting defects and dopants in the silicon bulk can interact with the radiation induced defects to form more complex hybrid defects with different electrical behavior. The ROSE [22; 23; 24] and RD50 CERN collaboration [25; 26; 27; 28; 29] have worked to identify the defects that are important to understand the effects of non-ionizing radiation damage in silicon . The main important defects introduced in silicon by irradiation can be found in table 2.3. The introduction rate of these different defects vary with the type and energy of the particle causing the damage, the present concentration of Oxygen in the bulk and of the thermal history of the silicon sample. Defect engineering can be performed by favoring the formation of non electrically active defects such as the ($V-O_{2i}$) defect which

is enhanced by the presence of Oxygen dimers (O_{2i}). Oxygenated high resistivity silicon exhibit a high concentration of such dimer and therefore can substain higher radiation doses before effects detrimental to the operation of the planar pixel sensor becomes significant.

TABLE 2.3 – Important defects introduced by NIEL in silicon ([17; 27])

Defect type	Charge state	Energy level (eV)
Interstitial (I)	I^-	$E_C - 0.39$
	I^0	
	I^-	$E_V + 0.4$
Vacancy (V)	V^{--}	$E_C - 0.09$
	V^-	$E_C - 0.4$
	V^0	
	V^+	$E_V + 0.05$
	V^{++}	$E_V + 0.13$
Divacancy (V_2)	V_2^{--}	$E_C - 0.23$
	V_2^-	$E_C - 0.39$
	V_2^0	
	V_2^+	$E_V + 0.21$
A-Center (V-O)	$(V-O)^-$	$E_C - 0.18$
	$(V-O)^0$	
Divacancy Oxygen complex ($V_2 - O$)		
Vacancy Oxygen dimer complex ($V - O_{2i}$)	$(V - O_{2i})^0$	

The modeling of the complex chemistry of defects in irradiated silicon can be quite complex and unpractical for the modeling of irradiated pixel sensors. However simple parametrization reproducing well the different known effects observed in silicon has been developped in the recent years. A deep acceptor and a deep donor are introduced in the bulk to account for space charge sign inversion (SCSI), double junction effects [5; 6] and leakage current increase [5; 6; 30; 31]. In addition, to account for trapping and recombination of carrier induced by radiation damage, a shallow hole and electron trap must be added. The model we used is shown in tables 2.4 and 2.5 , based on the latest results from RD50 collaboration [29] and work of several groups [32; 33; 34].

TABLE 2.4 – n-type radiation damage model

Defect's energy (eV)	Introduction rate (cm^{-1})	Electron capture cross-section (cm^{-2})	Hole capture cross-section (cm^{-2})
$E_c - 0.42$	13	2.2e-15	1.2e-14
$E_c - 0.53$	0.08	4e-15	3.5e-14
$E_c - 0.18$	100	1e-14	1e-16
$E_v + 0.36$	1.1	2e-18	2.5e-15

TABLE 2.5 – p-type radiation damage model

Defect's energy (eV)	Introduction rate (cm^{-1})	Electron capture cross-section (cm^{-2})	Hole capture cross-section (cm^{-2})
$E_c - 0.42$	1.613	2.e-15	2e-14
$E_c - 0.46$	0.9	5e-15	5e-14
$E_c - 0.10$	100	2e-15	2.5e-15
$E_v + 0.36$	0.9	2.5e-14	2.5e-15

These parameters must be adjusted using a fit method to determine adequate introduction rates, level and capture cross-section for each type of silicon used.

A simpler parametric model has been developed by the ROSE and RD50 collaboration to evaluate the evolution of leakage current, average trap characteristic lifetime and net dopant/defect concentration in irradiated sensors. The Variation of leakage current density in the bulk of a depleted sensor is parametrized following equation 2.33

$$\frac{\Delta I_{vol}}{V} = \alpha\Phi \tag{2.33}$$

Where I_{vol} is the volume generated current, V the bias potential, α the leakage damage constant and Φ the exposed fluence in n_{eq}/cm^2. The average trap characteristic lifetime can be also be expressed as a function of fluence as shown in equation 2.34, where τ_{t0} is the original trapping time.

$$\frac{1}{\tau_t(\Phi)} = \frac{1}{\tau_{t0}} + \beta\Phi \tag{2.34}$$

Finally, the net dopant/defect concentration is expressed following equation 2.35, where N_{D0} is the initial donor concentration, N_{A0} the initial acceptor concentration and N the net dopant concentration. From N, it is possible to compute the depletion potential following

equation 2.5. Acceptor removal and donor creation have not been observed experimentally, explaining the absence of such term in this equation. 0

$$N(\Phi) = N_{D0}e^{-c\Phi} - N_{A0} - b\Phi \tag{2.35}$$

Table 2.6 show typical value for the radiation damage constants of this model.

TABLE 2.6 – Typical radiation damage constants [35]

constant	value
α	$8.0 \times 10^{-17}\ Acm$
β	$0{,}24 \times 10^{-6}\ cm^2 s^{-1}$
c	$3.54 \times 10^{-13}\ cm^2$
b	$7.94 \times 10^{-2}\ cm^{-1}$

2.5.2 Ionizing energy loss

Silicon dioxide present at the surface is the main material damaged by ionizing energy loss . The dose of ionizing energy loss radiation damage is usually expressed in Rad, which represent 6.24×10^{10} MeV of ionizing energy deposition per kilogram of material.

SiO2's Oxygen valence electrons present at the interface and uncompensated by a Silicon atom create local traps for holes, as shown in figure 2.13. Holes from electron-hole pairs generated by ionizing particles crossing the oxide can be trapped in this layer. Electrons have higher mobility ($20\ cm^2/Vs$) than holes ($2 \times 10^{-5}\ cm^2/Vs$) in SiO2 and collect rapidly while holes accumulates in the traps present near the interface [36]. The electrical field created by this sheet of positive charge attracts silicon's free electrons that then for a compensating layer of free carrier at the Si-SiO2 interface. Few carriers can cross the interface potential barrier by tunneling and recombine with their opposite carrier, leaving the charge layer, called inversion layer, almost permanently at the interface.

The charge density at the interface is known to vary almost linearly with exposed fluence from $10^{11}\ cm^{-2}$ to $10^{12}\ cm^{-2}$ between 0 and $1 \times 10^8\ Rad$, usually equivalent in ATLAS inner detector to exposition to a NIEL of 0 to $1 \times 10^{15}\ n_{eq}/cm^2$. We then consider the charge layer to be saturated for higher fluences, as observed experimentally

[37]. Oxide charge saturation concentration is process dependent [38] so the saturation fluence and charge concentration can be chosen for modelisation to be coherent with the data presented in literature.

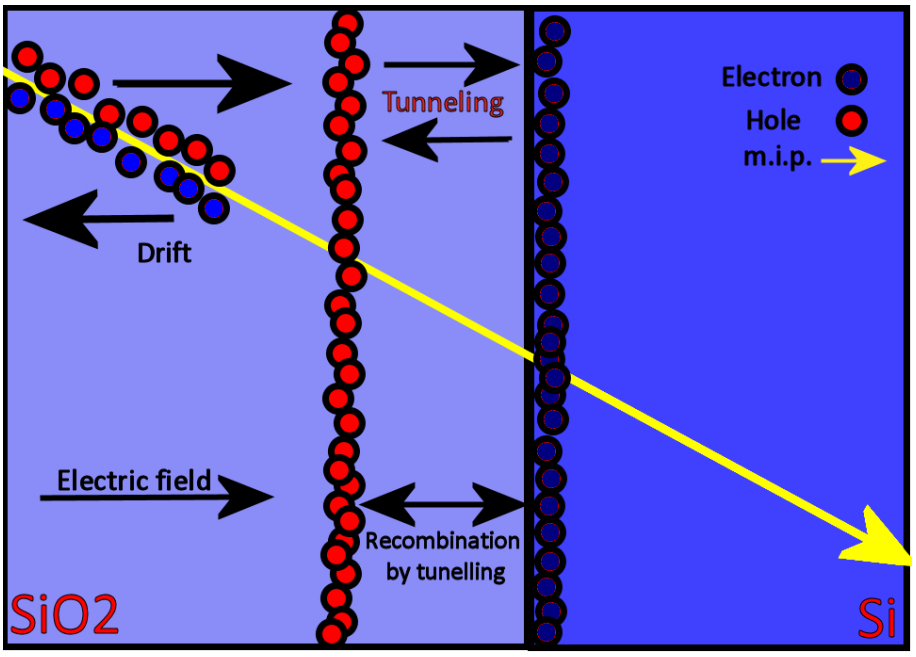

FIGURE 2.13 – Schematics of radiation damage effect at the silicon-silicon dioxide interface in silicon sensors.

The presence of this electron layer at the interface can form a conductive path between different electrodes, increasing crosstalk and leading to unwanted parasitic leakage path in the sensor. Mitigation methods to prevent this effect will be presented in next chapter.

Chapitre 3

TCAD Simulation models

Technology Computer-Assisted Design (TCAD) uses our present knowledge of the partial differential equations describing charge carrier's motion and interactions with the crystal lattice in semiconductors, detailed in equations 2.2, 2.3 and 2.4 coupled to finite element method to simulate the electrical parameters of the device. Finite element method use a linearized version of the transport equation to describe the problem in terms of a linear system of equation that can be solved by linear algebra methods. To obtain a solution to the variables of the transport equations (n,p,V) in a arbitrary geometry, we must subdivide the surface or volume in rectangular, triangular, prismatic or pyramidal sub-elements small enough that the solution in locally polynomial in this domain and can be approximated by a polynomial Φ. The sum of all sub-elements covering the simulation geometry is call the mesh, as seen in the example for a simple geometry in figure 3.1.

To obtain a good approximation of the solution using this method, mesh element's domain size must be chosen to be sufficiently small to be able to do this approximation. Region where the solution is expected to vary rapidly must be subdivided in small region until the solution can be represented as a locally polynomial function. TCAD software are bundled with meshing algorithm that can use know quantities in the geometry, such as impurity concentration, to generate the sub-elements covering the domain to simulate. However, no perfect method exist to determine the perfect mesh and case-by-case study of the mesh to use must be perform to ensure the validity of the solution obtained over this discretization. The solution to the equations, once meshing and interpolation equations are

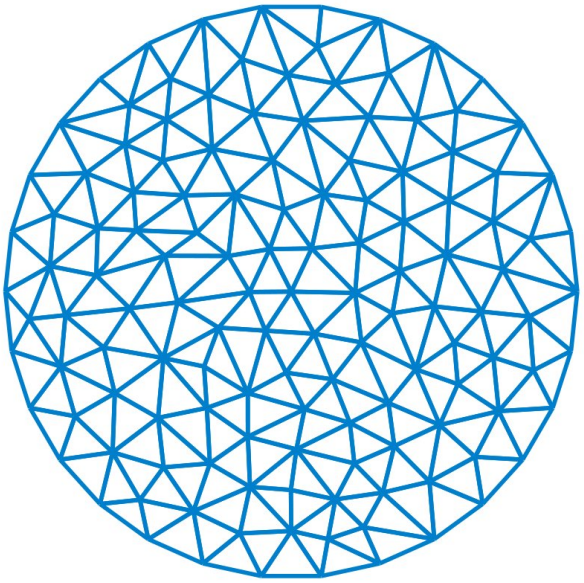

FIGURE 3.1 – Meshing of a disc surface using triangular sub-elements

chosen, can then be expressed as :

$$V, p, n = \sum_{i}^{n} a_i^{V,p,n} \Phi_i \tag{3.1}$$

Where i is the indice of an intersection of the sub-elements. The function Φ are usually chosen to be equal to 1 at element intersection i and 0 at all other surrounding intersection. Figure 3.2 show an example of functions Φ that can be selected in a simple 1D geometry to approximate a semi-spherical function.

This method can be used to explore different designs of semiconductor detectors before their production and optimize its electrical parameters. We used this method to explore different possible designs for the IBL and super-LHC ATLAS planar pixel detector. The influence of many design parameters as the number and spacing of guard rings, sensor's thickness and inactive edge width on sensor electrical characteristics have been simulated, giving insight on the effects of sensor design and processing on the devices performances. Radiation damage can also be included in the physical model used in the simulation, allowing to extract macroscopic effects caused by change in bandgap structure detailed in

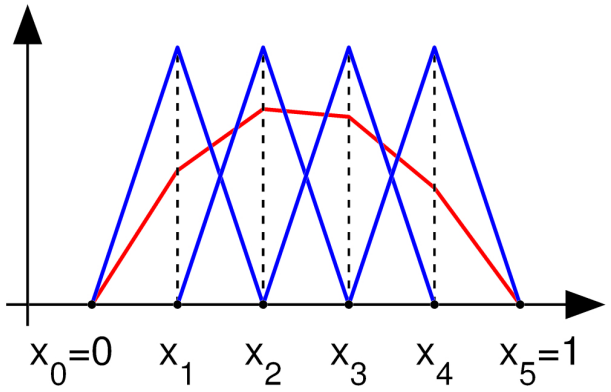

FIGURE 3.2 – Simple linear interpolation function used to approximate a function in 1D

chapter 2.

3.1 Process simulation

The first step to obtain a realistic simulation of a sensor is to obtain an accurate description of its geometry. Most TCAD simulation software include a process simulation package that allow to simulate the fabrication process of silicon sensors. The main step to produce a realistic process simulation of a pn junction are as follow :

1. Oxidation
2. Nitride deposition and etching
3. Insulation implantation
4. Oxide etching
5. Implantation
6. Thermal annealing
7. Via etching and electrode deposition
8. Passivation and passivation etching

In typical silicon detectors, an additional implant must be created to insulate the electrodes from each other before creating the main implant. As it was seen in chapter 2,

ionizing radiation damage cause the formation of an inversion layer at the silicon-oxide interface that can shortcut the different implants. To prevent this, an low dose p+ implant is created on the n+ side of the pixel sensors. This implant's excess of free holes will compensate the inversion layer created by the accumulation of electrons and interrupt the channel that forms at the surface. Three type of insulating implants are used in the industry. The most simple is the p-spray technique, which consist in the implantation of a uniform p dose across the full wafer. A different technique , called p-stop, use an additional nitride layer deposited over the oxide layer to stop the dopant ion beam and create segmented p+ implants where nitride was etched between the main n+ ones. Finally, an hybrid method, called moderated p-spray, combines both method. The thickness of the layer of nitride is chosen to let some of the ions reach the silicon, creating a uniform implant across the wafer and stronger and deeper implants where nitride was etched, between the n+ implants. Figure 3.3 shows the two first type of insulation. The moderated p-spray is simply a combination of both method. The insulation implants form junctions with the main n+ implant and high electric field will be present in this region. Each method need to be optimized to avoid creating high electric field that may lead to breakdown while providing sufficient insulation for operation after irradiation.

The second step in the process consist in heating the bare wafer of silicon in a oxygen atmosphere to grow a layer of silicon dioxide at the surface of the wafer ($O(200\ nm)$) . This layer is then etched down to a very thin layer ($O(40\ nm)$) using lithography, to form the shape of the implants. A beam of mono-energetic ions ($O(10-120\ keV)$) is then directed to the surface of the wafer and a fixed dose of ion by surface unit ($O(10^{15}\ cm^{-2})$) is delivered. In the area where a thick film of oxide has been left, the stopping power of the layer is sufficient to completely absorb the incoming ions while in the etched region, ions will travel into silicon forming an implant with a shape and magnitude determined by the implantation dose, the beam energy and orientation and the thickness of the oxide layer left in the implant area.

One all implants have been created, the wafer must undergo an annealing step, where it is heated for sometime at very high temperature. This step is needed to activate the dopant introduced in silicon. To be electrically active, dopant atoms must be correctly placed in

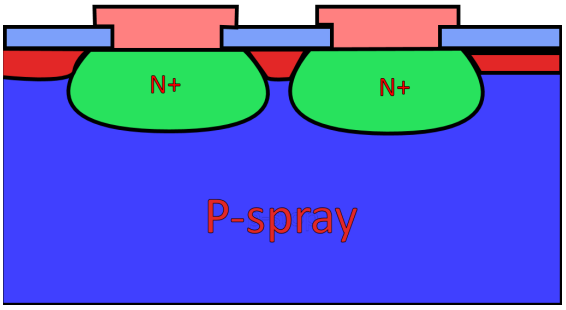

(a) p-spray insulation

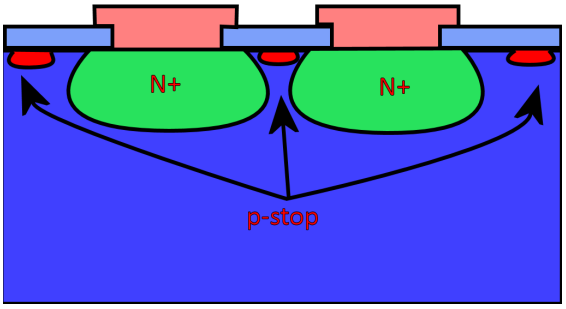

(b) p-stop insulation

FIGURE 3.3 – The two main type of implant insulation used in pixel sensors.

the crystal lattice. The heating process gives the kinetic energy to the dopants to diffuse through the bulk and react with the lattice structure to become electrically active. During this process, the shape of the implant is modified as dopants migrate by diffusion further into the silicon bulk. The annealing temperature and time are important parameters to determine the final shape of the junction.

The final step of the process consist in opening small holes, called via, in the oxide in the n+ implant area reaching the surface of the silicon (nitride has previously been opened in this area to allow access to the oxide at this step). An aluminum layer ($O(800\ nm)$) is then deposited and etched outside electrode area to produce the electrical contacts to the n+ implants. Finally, a thick layer of a passivating material is deposited over the area uncovered by the electrodes to provide a good protection of the surface.

The parameters of the process affecting the implant profile need to be known to create accurate representation of the device we wish to simulate. The process details we use in our simulation have been obtained through discussion with designers and manufacturer of silicon devices. Some parameters are however hard to determine from accessible data and are not disclosed by the manufacturer. These values can however be obtained through experimental methods as will be shown in the rest of this chapter.

3.2 Device simulation

Device simulation is used to obtain electrical parameters of a geometry we built through process simulation. For a device simulation, the geometry to be simulated must be carefully chosen to avoid increasing the computational complexity of the problem to be solved. Boundary conditions must also be selected to represent the operation conditions of the device.

3.2.1 Geometry

Full simulation of a pixel sensor is impossible to perform in modern computers as the number of mesh point needed to accurately describe the solution to the equations in the three-dimensional domain is too important to be handled by computers. Simulation performed in the next section are done in two dimension to reduce the simulation time. Periodicity and symmetry of the geometry can be exploited to reduce the size of the problem to be solved. Figure 3.4 shows how pixel sensor quasi-periodicity and symmetry can be used to define a two-dimensional geometry that can be simulated with a TCAD software. We consider a Y-Z oriented cut plane in a semi-infinite sensor with its guard ring structure and cutting edge and a plane of pixels extending extending infinitely in the $\pm X$ and $+Y$ direction. This represent a good approximation for a pixel sensor far from the corners of the device. The edges not represented in the two dimensional representation are supposed to not interfere with the local electrical behavior of the simulated geometry.

To obtain the solution to the differential equations describing the charge transport and Poisson equation, we must provide the boundary conditions as fixed values of the variables

to be solved, the electron and hole concentration (n,p) and the electrostatic potential(V) or their derivative, current densities ($\vec{J_{p,n}}$) and electric field ($\vec{E}$). Real operation conditions of the simulated sensors cannot be completely described in this manner and approximation must done to obtain a solvable problem. The simulation geometry must be selected to allow a solution that represent correctly the real operation conditions.

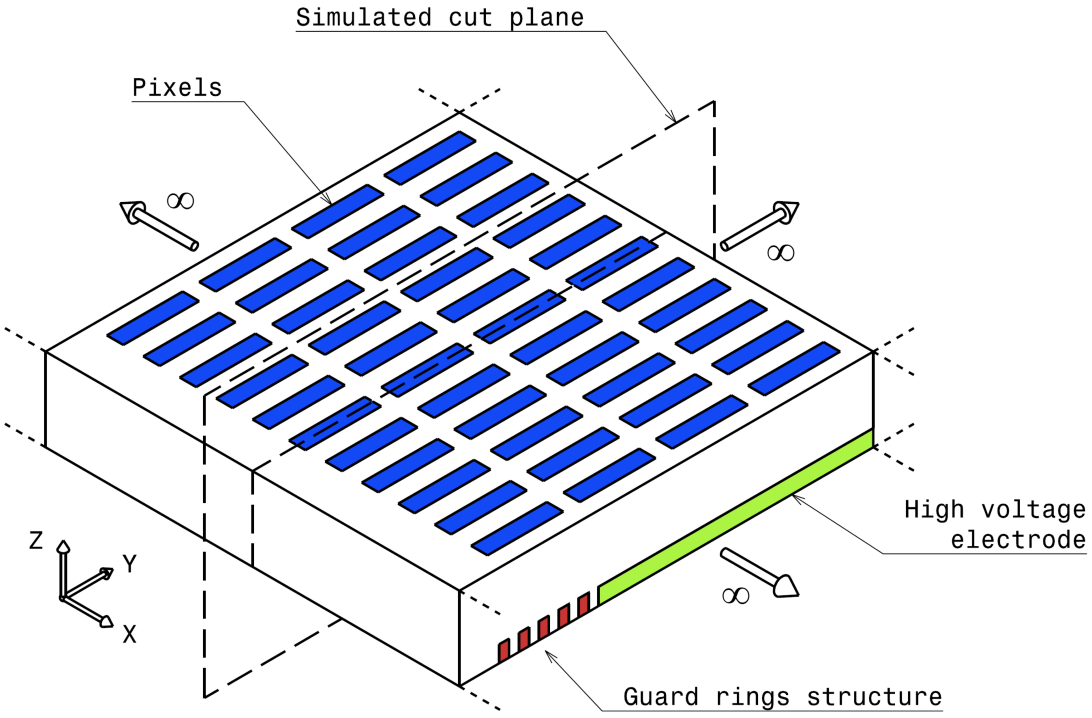

FIGURE 3.4 – Simplification of a n-in-n planar pixel sensor geometry for TCAD simulation

3.2.2 boundary conditions

To solve our set of differential equations we need to restrict ourselves to a solution in a bounded domain, the sensor. We must choose boundary conditions reflecting the properties of the system we want to simulate. Three types of boundaries were used during our simulation, representing the oxide-silicon interface, the electrode interface, and the periodicity boundary. In addition we need a model for the cutting edge of the sensor.

The boundaries between silicon dioxide and silicon is a semiconductor/insulator boundary characterized by the presence of an accumulated charge layer at the interface. The

boundary condition applied to these surfaces for the Poisson equation is the Neumann boundary condition (3.2) that takes into account the charge layer density (ρ_s) present at the surface . Also, electrons and holes concentrations are set to zero on this boundary and the current is not allowed to flow through this surface.

$$\hat{n} \cdot \epsilon_1 \vec{\nabla} \Phi_1 - \hat{n} \cdot \epsilon_2 \vec{\nabla} \Phi_2 = \rho_s \tag{3.2}$$

Metal-semiconductor surfaces are the boundaries between the silicon bulk and the metallic electrodes. This is usually a ohmic contact and the current is allowed to flow through them. The voltage Φ is constant and equals the bias voltage applied to the sensor by an external power supply. The concentration of carriers (p_s,n_s) at the surface of the contact is determined by equations (3.3), (3.4), derived for Boltzmann's statistics, knowing the bias voltage applied at the electrodes. The effect of the contact work function is considered negligible as highly doped regions are located below the electrodes.

$$n_s = \frac{1}{2}[(N_D^+ - N_A^-) + \sqrt{(N_D^+ - N_A^-)^2 + 4n_i^2}] \tag{3.3}$$

$$p_s = \frac{n_i^2}{n_s} \tag{3.4}$$

Where N_D^+, N_A^- are the ionized donors concentration and ionized acceptors concentration in cm^{-3}.

Guard ring structures are metal semiconductor interfaces where the metallic electrode self-biased. To represent this case, we must impose a null current flow on this contact. The bias voltages taken by the floating contacts are then found by the solver of the TCAD software.

To reduce the size of the problem to be solved, we can use periodicity boundary conditions using geometric properties of the sensor. In our simulation, we will be interested to the solution on the sides of the sensor. Knowing the solution will become quasi-periodic in the X-Y plane when approaching the center of the device. Far from the edge , we can truncate our model at a distance large enough to consider the solution will become as if it

was periodic at this point. We then impose the periodicity condition (3.5) at the surface for electrons and holes concentration and for the bias voltage.

$$\begin{aligned} \vec{\nabla} V \cdot \hat{n} &= 0 \\ \vec{\nabla} n \cdot \hat{n} &= 0 \\ \vec{\nabla} p \cdot \hat{n} &= 0 \end{aligned} \tag{3.5}$$

Where $\hat{n}$ is the unitary normal vector of the boundary. Physically, this represent the condition where no current is flowing out or in the geometry and no electric field lines flow out of the simulated boundary.

The dicing of pixel sensors from their originating wafer creates structural damage that affects the properties of the edge. A dead edge width must be included in the design to exclude this zone from the sensible part of the sensor. This dead edge is added to inactive part of the sensor and must be kept as small as possible.

A special attention must be taken to model the cutting edge of a silicon sensor. Dicing mechanism induces structural damages in the Silicon crystal lattice near the cutting region. This induces a process of amorphization of silicon. Amorphous silicon is a complex material where no short or long distance orders exists in the crystal lattice. A method to model amorphous silicon is to introduce a high number of defects in the band gap of Silicon. As the crystal lattice of the Silicon is highly perturbed in the cutting edge region, trap states are created by the defects in the crystal lattice that are introduced. To represent such a distribution of defects in the band gap, we use a continuous density of states distribution to describe the band gap defects distribution. This distribution can then be tuned to reflect the behavior of real sensors measured in the laboratory. The generation-recombination term related is calculated using an integral form of equation 2.10. Equation (3.6)[39] shows how we describe the defect distribution in the band gap.

$$g(E) = g_{TA}(E) + g_{TD}(E) + g_{GA}(E) + g_{GD}(E)$$

$$\begin{aligned} t_A(E) &= N_{TA} e^{\frac{E-E_c}{W_{TA}}} \\ t_D(E) &= N_{TD} e^{\frac{E_v-E}{W_{TD}}} \\ g_A(E) &= N_{GA} e^{(\frac{E_{GA}-E}{W_{GA}})^2} \\ g_D(E) &= N_{GD} e^{(\frac{E-E_{GD}}{W_{GD}})^2} \end{aligned} \tag{3.6}$$

The density distribution function consists of two exponential tails functions (TD, TA) and two Gaussian function distributions for donors and acceptors (GD, GA) giving the energy distribution in cm^{-3}. Table 3.1 shows the default parameters used for this model in our simulation. The defect density distribution that is created by these parameters is represented in figure 3.5. $E_v = -1.12\,eV$ is the valence band energy and $E_c = 0$ the conduction band energy. The model used in these simulations was proposed by *E. Noschis and al.* [40]

TABLE 3.1 – Default defect density of states distribution parameters in SILVACO TCAD software

Parameters	Values
N_{TA}	$1.12 \times 10^{21}\ cm^{-3}/eV$
N_{TD}	$4.00x10^{20}\ cm^{-3}/eV$
N_{GA}	$5.00 \times 10^{17}\ cm^{-3}/eV$
N_{GD}	$1.50 \times 10^{18}\ cm^{-3}/eV$
E_{GA}	$0.4\,eV$
E_{GD}	$0.4\,eV$
W_{TA}	$0.025\,eV$
W_{TD}	$0.050\,eV$
W_{GA}	$0.100\,eV$
W_{GD}	$0.100\,eV$

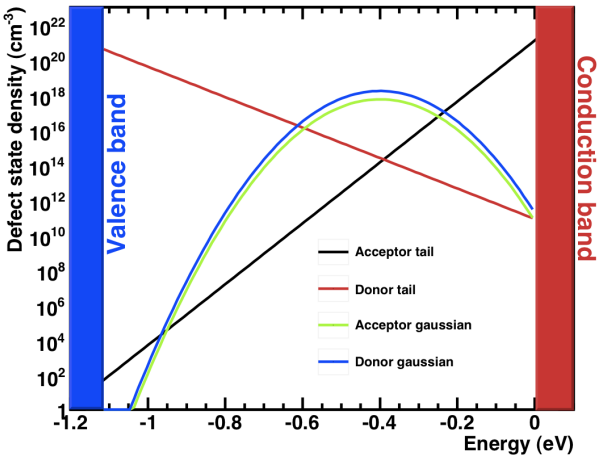

FIGURE 3.5 – Defect density distribution in the band gap of amorphous silicon used for our simulation

3.3 The Multi-Guard Ring structure

The goal of the guard ring structure present next to the high-voltage electrode or the pixel matrix is to ensure a smooth transition from high voltage to ground while approaching the outer edge of the device. The edge usually takes the same potential as the backside of the sensor as the high amount of defects at the cutting edge render it conductive and electrically link the two sides together. Each guard ring acquire its bias voltage by a punch-trough mechanism forming a smooth transition from high bias voltage to ground at the edge of the sensor. This is needed to ensure that no bias voltage difference exist between the two sides of the wafer, close to the edge. This bias would generate excessive current detrimental to the operation of the sensor [36]. The inner ring can also be used, if connected to bias, to collect leakage and surface current that would increase the noise when collected by the pixels. This principle is called a current-terminating structure (CTS) [40].

In ATLAS actual design of the pixel sensor, the number of guard ring is fixed to 16, with an implant width of 10 microns. The electrodes covering the guard ring implants are 16 to 22 μm wide with the largest at the outer side of the structure. They overshoot the implant by 2 μm in the edge direction and 1 to 40 μm in the active area direction. Distance between them varying from 15 to 8 μm. The guard rings represent a dead zone in pixel sensors, meaning no particle is detected close to the structure. This corner of a IBL prototype sensor with its guard ring is represented in figure 3.6. The presence of these inactive zones surrounding the sensor force the overlapping of the sensors in ATLAS tracker to avoid detection gap between sensors. This overlap increase the amount of material present in the tracker and should be avoided to reduce the material budget of the inner detector and increase the simplicity of its configuration. Reduction of the guard ring area for the sensors to be used in IBL are a key to minimize its material budget and its inactive zones.

The goals of the simulation performed in this chapter are to evaluate the effects of modifying the number of guard rings and their spacing factors that can reduce the dead zone while maintaining adequate operation conditions for the sensor and exploring the effect of radiation damage on the efficiency of guard ring structure. This was used to determine how modifications to the sensor and guard rings geometry can be used to reduce inactive

area while keeping guard rings active.

3.3.1 Principles of guard ring structures

The guard rings are used to control the potential drop from electrodes in the active area of the sensor to the cutting edge of the device, as shown in figure 3.7 for the example of a n-in-n sensor. This provide a reliable way to control the potential at the surface of the sensor edges. Without guard rings, the potential distribution at this surface would be largely influenced by its processing quality. The presence of an inversion channel,which magnitude is related to surface quality, render the surface conductive, and potential drop only occur in resistive regions of the surface. The presence of defects at the interface will affect the resistivity of the surface and can be detrimental to detector operation by causing the presence of sharp electric field peaks in the more resistive regions and eventually breakdown of the sensor. The guard rings help to control the surface behavior and render the sensor detector more stable and independent of the surface state by imposing a gradual surface potential drop through a bulk process, independent of the surface state.

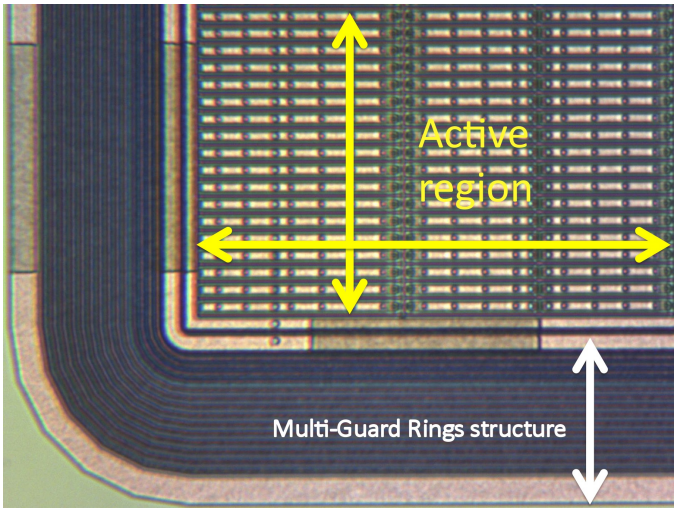

FIGURE 3.6 – Corner view of a FE-I4 n-in-p pixel sensor structure showing the guard ring structure and the 3 first column and 18 first row of pixels.

Fig. 3.8 shows guard ring geometry, with its metal overhangs covering the oxide. Guard rings are biased by a punch-trough mechanism creating a current circulating between the guard rings. The punch-trough occurs when the depletion region of both guard rings are in contact. This happens as the depletion region of the pixels or high voltage electrode expands as bias increase and reach the different guard rings. The vicinity of a guard ring metal electrode is biased at the same potential as the silicon implant region, reducing the vertical electric field in the oxide under the guard ring overhangs. This has the effect of

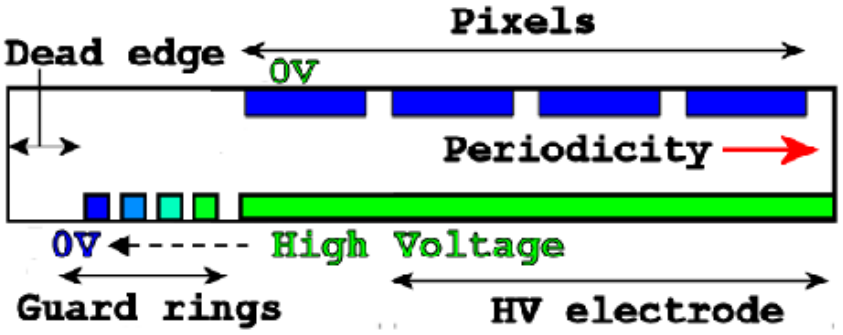

FIGURE 3.7 – Guard ring electrical behavior (n-bulk)

interrupting the inversion channel formation at the $Si - SiO_2$ interface, problematic for n- in-p sensors, as shown on figure 3.8. This channel is caused by the presence of hole traps near the SiO_2 boundary with Silicon, as explained in chapter 2. These traps become positively charged as they are filled by holes created by an incident ionizing particle or thermal generation [41]. In the case of n-in-p sensors, the guard rings are located on the same surface as the pixels, collecting electrons. The orientation of the electric field inside the oxide will favor the drift of holes to the silicon silicon dioxide interface and increase the magnitude of the inversion layer charge density depending on the local current density in the oxide. Close to the guard rings, reduced electric field will inhibit the drift of the hole in the oxide and cause this interruption of the inversion channel

A set of two guard rings can be seen as a blocked MOSFET with the source connected to gate. The transistor is kept in an off state with the punch-trough voltage and gate to drain resistance determining the guard ring bias behavior. The guard ring metallic overhangs, are used to reduce the electric field present on this side of the guard ring at the interface and interrupt the electron channel by suppressing the vertical electric field in this region. The long overhang, oriented towards the pixel region, is used to suppress the punch-trough hole current and increase the punch-trough voltage [36]. The p-spray, p-stop and moderated p-spray methods are also used to mitigate the effects of the formation of this inversion channel. A drawback of this method is the apparition of electric field peaks at the sides

of the guard ring's implant junction with the p-spray implant, making this region a weak point for breakdown formation.

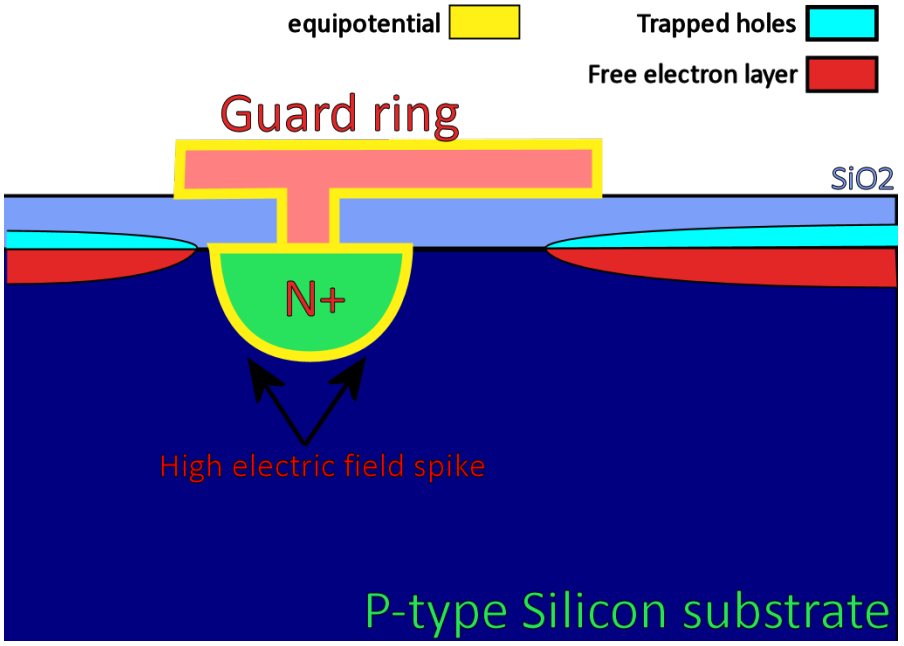

FIGURE 3.8 – Guard ring schematic representing the interruption of the inversion channel (p-bulk)

The multi guard ring structure geometrical and electrical parameters such as the doping profile of the implant, the overhangs length and the distance between guard rings influence the electrical behavior of the guard rings. The voltage drop between guard rings will be modified if these parameters are changed as punch-through voltage and currents will be affected by these modifications. The punch-trough mechanism occurs at depletion and guard rings become active when lateral depletion zone reach them. As we know from equation 2.5, depletion depth is proportional to the square root of the applied bias voltage. For guard rings located close to the pixel region, the overhang directed toward the pixel must be kept small to favor higher punch-trough currents and bigger voltage drop on shorter distance. TCAD simulation represent the perfect tool to study the potential distribution of guard ring geometries and to optimize them to improve the performances of the pixel sensors

3.3.2 Optimization of guard ring structures for reduction of inactive area and radiation hardness

TCAD simulation focuses on comparing electrical parameters of different multi-guard ring structures before and after irradiation. Figure 3.9 shows the geometry of the three structures simulated. The first one is the ATLAS actual pixel sensor, an n-in-n structure. The two others are n-in-p designs proposed as candidate for IBL and super LHC pixel sensor replacement. Detectors with these new multi-guard ring structure designs have been produced in collaboration with the laboratories forming the ATLAS Planar Pixel Sensor Upgrade group. P-bulk and n-bulk productions of pixel sensors including other structures, labeled in this document as respectively PPSU09-n and PPSU09-p, were organized and based on the knowledge gathered from the simulation presented here and experimental studies from collaborating laboratories.

Simple $6x6\ mm$ diodes with a number of guard rings varying from 1 to 4 were placed on the production to help with simulation model calibration by providing a simple geometry for comparison with TCAD results. The large size of the diode guard ring allow easy measurement in clean room of their potential and were also used to study the evolution of guard ring behavior for this production under irradiation.

The simulation studies performed prior to the production of the sensors [42; 43; 44; 45; 46] have shown that the results of the simulation, regarding guard ring behavior and breakdown voltage was dependent on doping profile of the implants forming the guard ring structure and pixels. A dedicated test structure was placed on each of the PPSU09 wafer production to eventually measure the profile of the implants using various techniques. Results of these measurements will be presented in the next chapter. Simulation presented in this section are based on the measured implant parameters for the PPSU09 production and simulation done prior to it have been reprocessed with the correct implantation parameters. Bulk resistivity was fixed to 5000 Ωcm for all simulation. Temperature was 300 K for unirradiated sensors and 250 K for irradiated ones.

In this section, I present simulation performed to reduce the span of the multi guard-ring structure through reduction of the number of guard rings and shift of the structure under the pixels. Radiation damage effects on guard rings were simulated to evaluate the

behavior of the new guard ring structure under irradiation. Following the results of these simulations, the method was used for the final n-in-n planar sensor candidate for the IBL in the PPSU09 production.

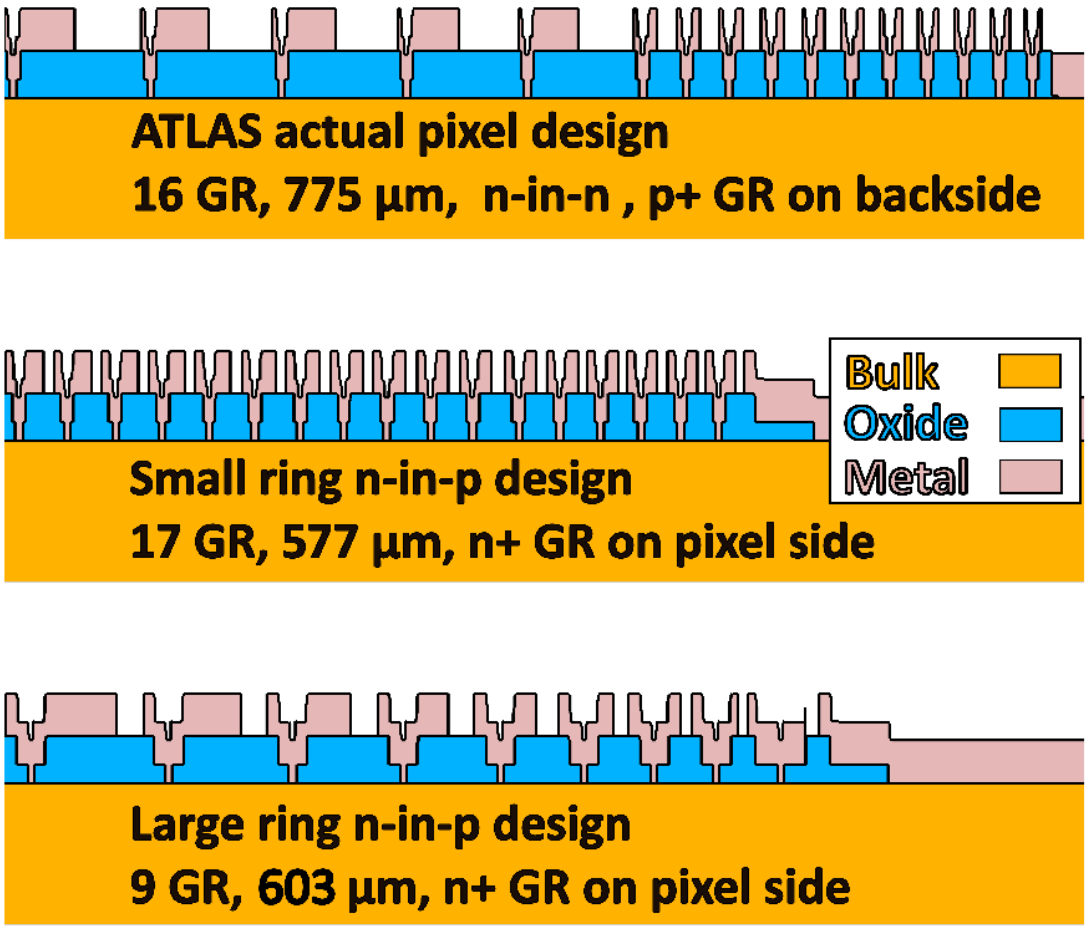

FIGURE 3.9 – Multi-guard ring structures used for simulation, obtained from process simulation

Simulation of the current ATLAS planar pixel sensor design was first performed up to 500 V for unirradiated and irradiated sensors up to 10^{15} $n_{eq}cm^{-2}$, the foreseen fluence for the actual sensor in LHC. The radiation damage model presented in table 2.4 was used. Figure 3.11 shows the simulated bias voltage for the Actual ATLAS pixel design for irradiated and unirradiated case. The irradiated case is simulated at the working operation bias voltage of 150 V. The irradiated model simulation were performed at 500V, the maximum

possible bias voltage reachable with the current power supplies. One pixel is included along with the guard rings (to the left of the figures). As fluence seen by the sensor increase, the space charge sign invert and depletion occurs from pixel toward the backplane like in a n-in-p sensor design. Figure 3.10 show the potential distribution on the guard rings of the ATLAS model as a function of the bias voltage. Comparison with experimental data is also shown. More details on experimental validation will be given in next chapter.

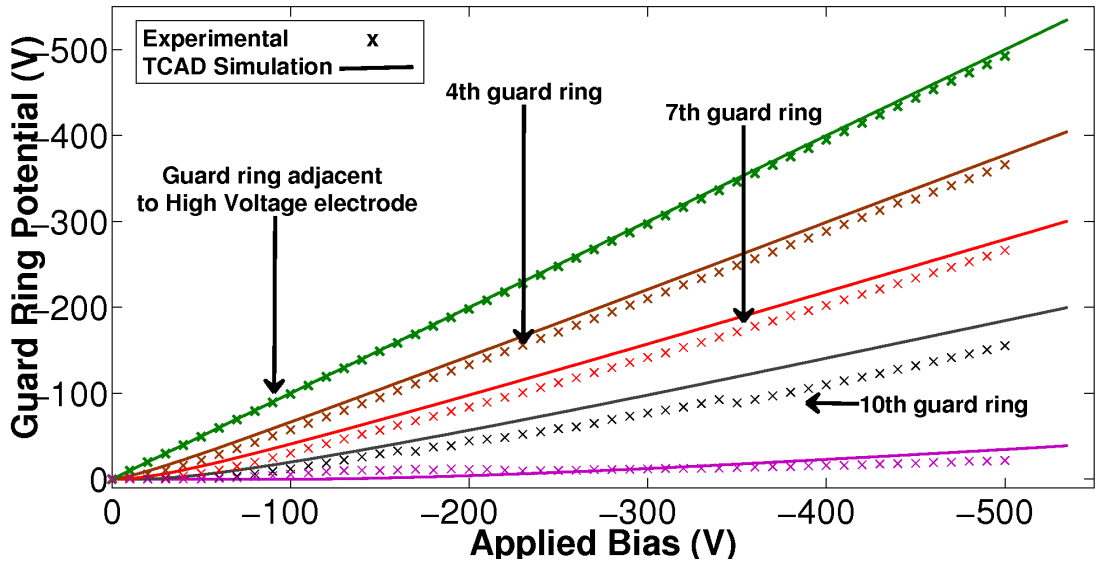

FIGURE 3.10 – Potential distribution in the ATLAS standard n-in-n Multi-Guard Ring Structure, simulated and measured

Figure 3.12 shows the electron concentration in the sensor for different fluences. The results of Space charge sign inversion (SCSI) is the replacement of electrons by holes as the majority carrier. This is shown in figure 3.13 representing hole concentration increasing as electron concentration decrease, mainly in the undepleted region. The undepleted volume for an unirradiated sensor extends on 900 microns from the edge of the sensor. The depletion zone never reach the edge of the device because of the large 500 μm safety edge left after the guard rings. This edge width could be modified to reduce the inactive edge of the sensor while keeping a safe margin between the cutting edge and the depletion region. This width is retained until space charge sign inversion but it is then replaced by a holes undepleted area , as seen in figure 3.13.

The n-in-p structures shown in figure 3.9 were also simulated in the IBL conditions

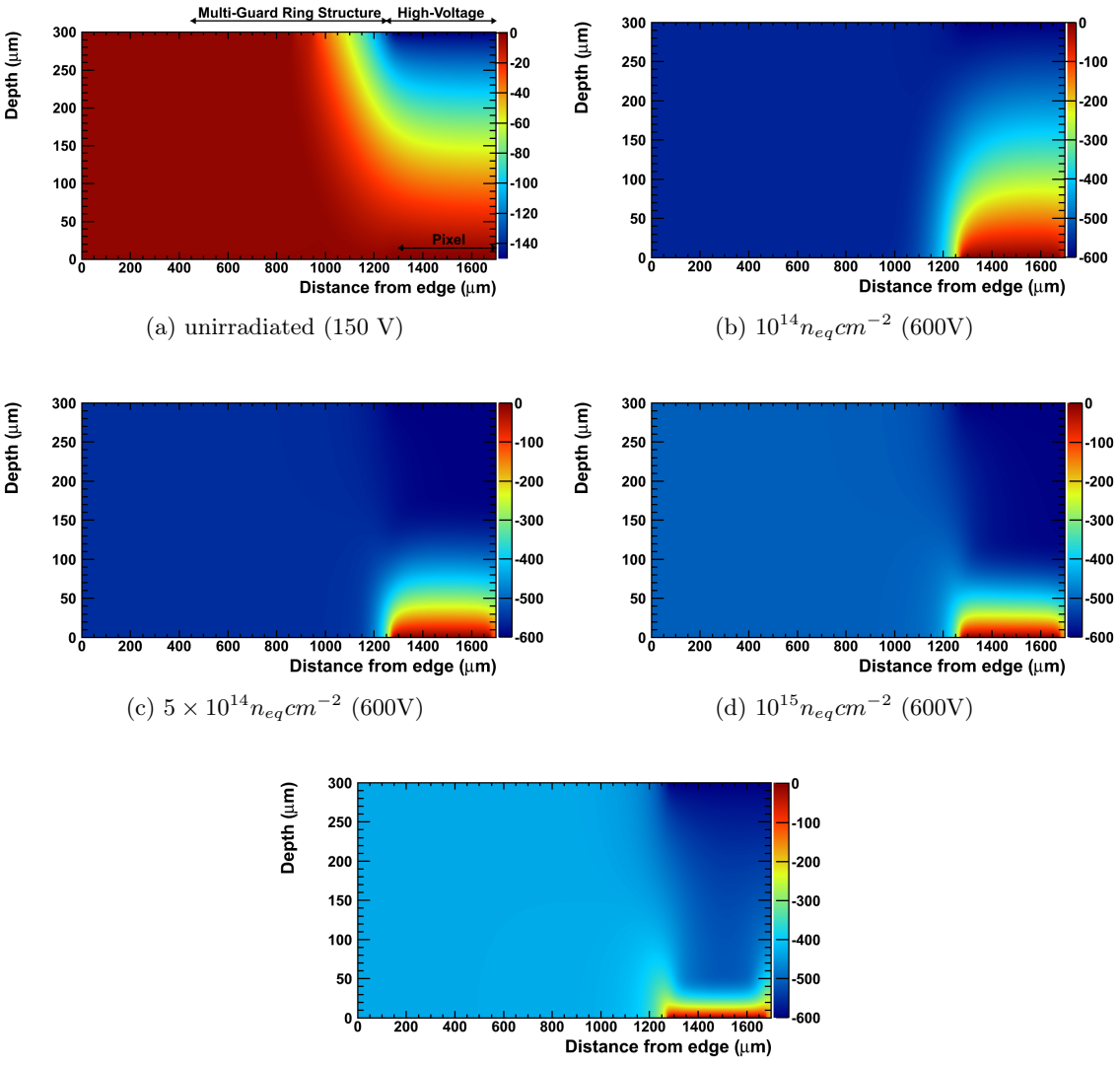

(a) unirradiated (150 V)

(b) $10^{14} n_{eq} cm^{-2}$ (600V)

(c) $5 \times 10^{14} n_{eq} cm^{-2}$ (600V)

(d) $10^{15} n_{eq} cm^{-2}$ (600V)

(e) $5 \times 10^{15} n_{eq} cm^{-2}$ (600V)

FIGURE 3.11 – Simulated 2D voltage profile for ATLAS n-in-n pixel sensor (300 μm thickness, 1700μm width. Color scale in Volt)

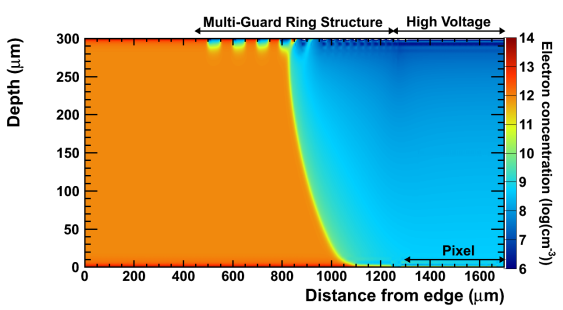

(a) unirradiated (150 V)

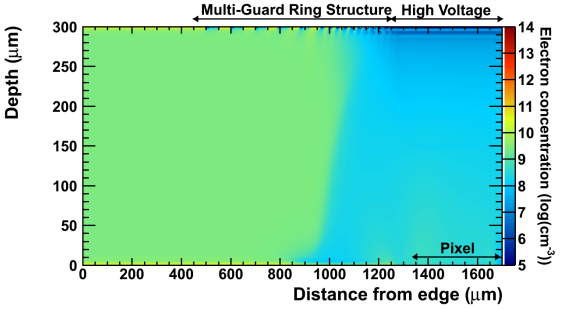

(b) $10^{14} n_{eq} cm^{-2}$ (600V)

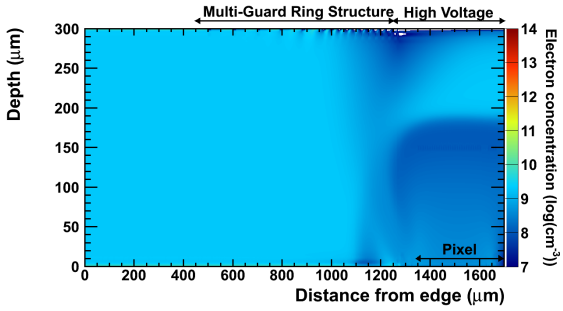

(c) $5 \times 10^{14} n_{eq} cm^{-2}$ (600V)

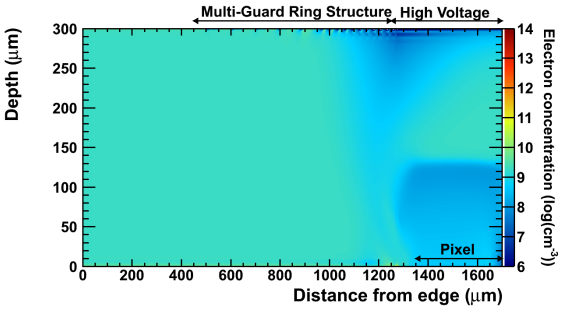

(d) $10^{15} n_{eq} cm^{-2}$ (600V)

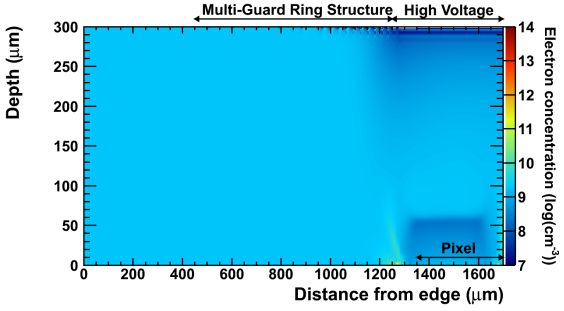

(e) $5 \times 10^{15} n_{eq} cm^{-2}$ (600V)

FIGURE 3.12 – Simulated 2D electron concentration profile for ATLAS pixel sensor (300 μm thickness, 2500μm width)

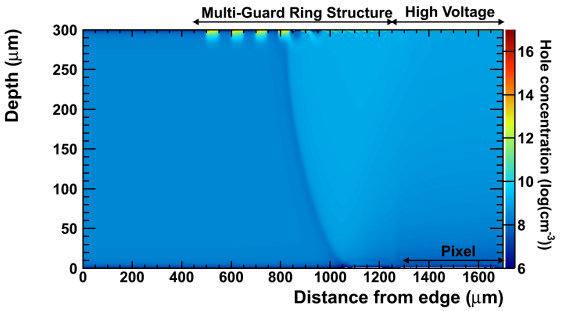

(a) unirradiated (150 V)

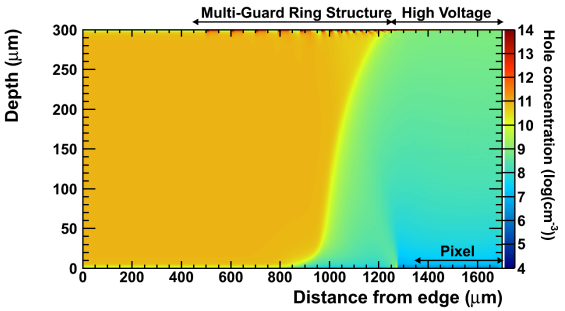

(b) $10^{14} n_{eq} cm^{-2}$ (600V)

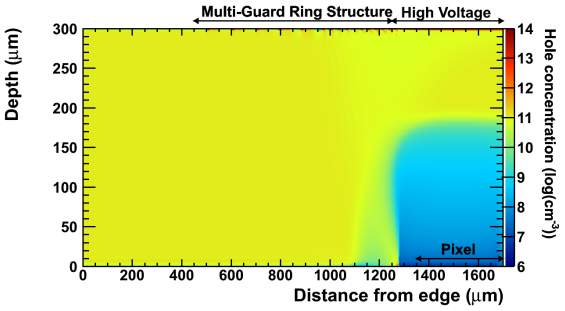

(c) $5 \times 10^{14} n_{eq} cm^{-2}$ (600V)

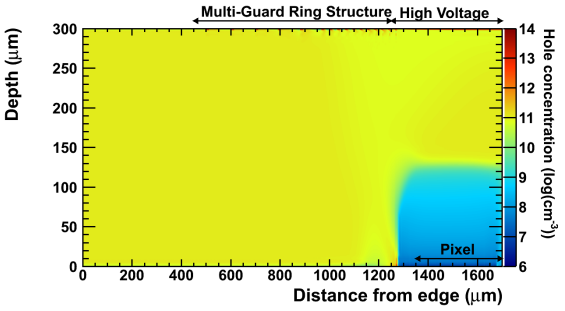

(d) $10^{15} n_{eq} cm^{-2}$ (600V)

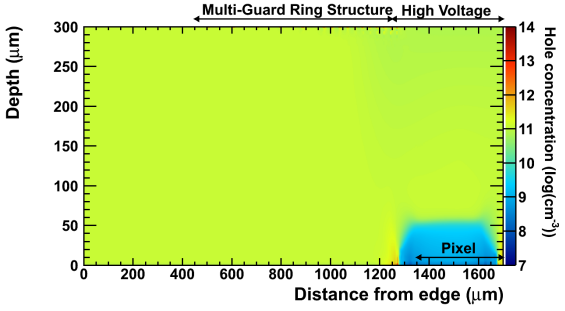

(e) $5 \times 10^{15} n_{eq} cm^{-2}$ (600V)

FIGURE 3.13 – Simulated 2D hole concentration profile for ATLAS pixel sensor (300 μm thickness, 2500μm width)

(250 microns edges, 1000V bias voltage, up to 10^{16} $n_{eq}cm^{-2}$). These n-in-p guard ring design were proposed to reduce the span of the guard ring structure currently used by reducing the size of the different guard rings or by reducing their number of them. The first design uses 17 very small guard rings while the second model use 9 larger guard rings and both represent an approximative reduction of the guard ring span by 200 μm. Figure 3.14 shows the hole concentration in the small guard ring sensor at various levels of irradiation. Resistivity of the silicon is reduced by the radiation damage and depletion potential should be increased. This result in a reduction of the visible depth of the depleted region for a given bias voltage. The depletion region never reaches the cutting edge of the sensor indicating that the 100 μm safety margin is safe enough for this type of n-in-p sensors. The large guard ring model show hole concentration distribution compatible with the small guard ring model and is not represented here.

Figure 3.16 show the distribution of potential on the guard rings of the three structures. The unirradiated structures are biased to voltage higher than breakdown voltage to observe the guard ring behavior and put in evidence the bend in the curves due to breakdown that should be observable experimentally. This simulation is possible because TCAD simulation does not include thermal simulation. Voltage curves shown in figure 3.15 are cut before the 1500 V bias voltage because of the divergence when simulating bias voltage much over breakdown voltage. This is due to a hard breakdown occurring on edge pixel side generating huge current. Guard rings are biased as the depletion zone limit approach toward them and as current begins to circulate between them by punch-trough mechanism. In n-in-n sensors, as depletion occurs from pixel side after SCSI, guard rings on the opposite side stay in the undepleted zone until full depletion of the sensor, making them ineffective to provide the smooth surface potential drop required for operating sensors with a high full depletion voltage. This situation also implies that a steep voltage variation is present at the surface between the pixels (0 V) and edges (High Voltage). This eventually creates a weak spot favoring breakdown in the sensor, as observed in the Current versus Voltage curves in figure 3.15. The guard rings of the n-in-p structures have a similar behavior before and after irradiation as the depletion still occurs from the pixel side towards the high voltage electrode side. The difference in the bias potential of each guard ring at different

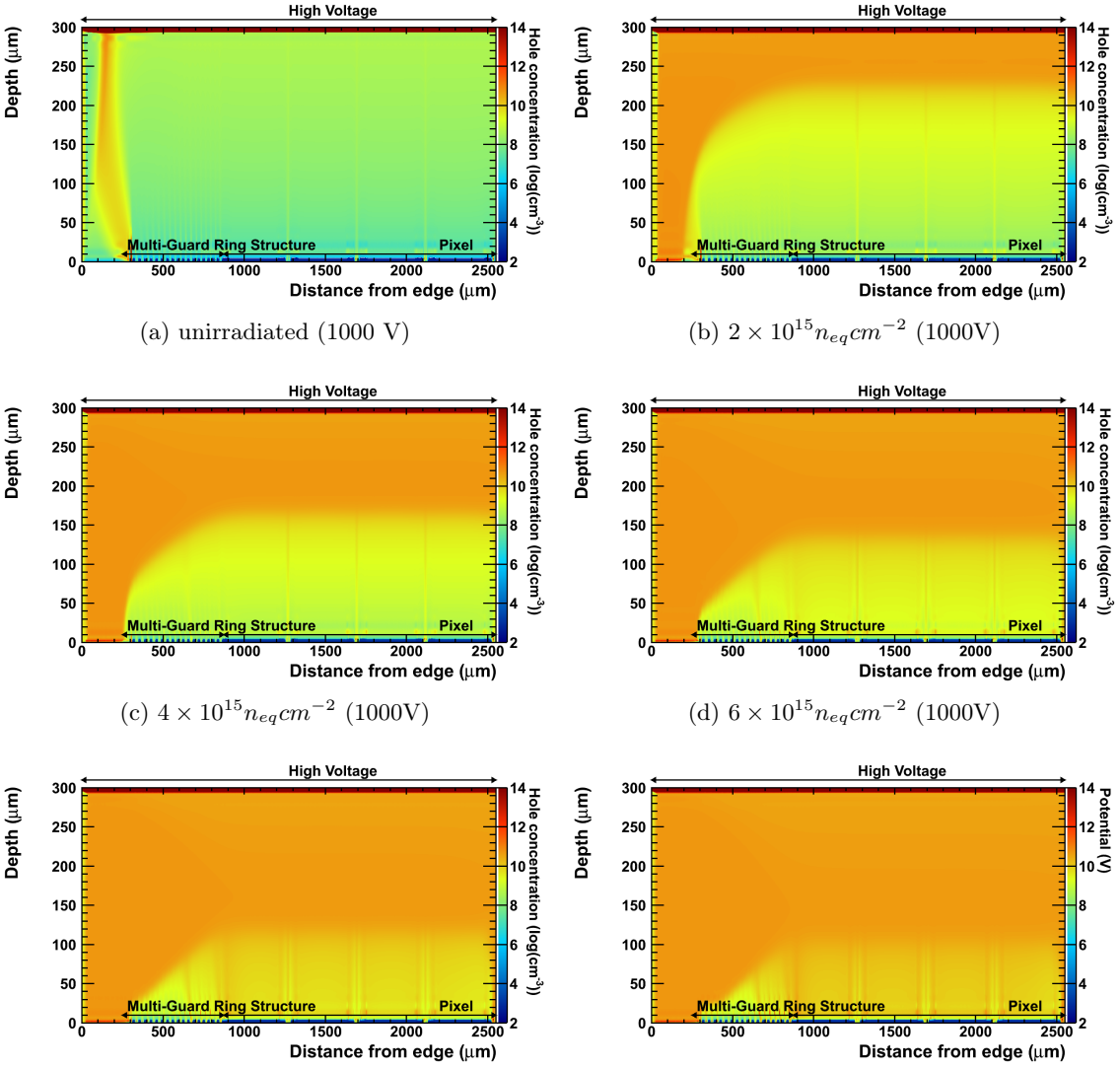

(a) unirradiated (1000 V)

(b) $2 \times 10^{15} n_{eq} cm^{-2}$ (1000V)

(c) $4 \times 10^{15} n_{eq} cm^{-2}$ (1000V)

(d) $6 \times 10^{15} n_{eq} cm^{-2}$ (1000V)

(e) $8 \times 10^{15} n_{eq} cm^{-2}$ (1000V)

(f) $10^{16} n_{eq} cm^{-2}$ (1000V)

FIGURE 3.14 – Simulated 2D hole concentration profile for n-in-p small guard ring type pixel sensor (300 μm thickness, 2500μm width)

fluences is due to the damage in the oxide which accumulate charge at the silicon-oxide interface and to a modification of the position of the depletion region limits. The change in space charge density modify the effective doping concentration that determines the full depletion potential of the sensor. As guard rings are biased by a punch-trough mechanism, the position of the depleted region limit relative to the guard rings position determines the bias potential of guard rings as a function of high voltage bias. The bent observed in guard ring potential curves at high voltage is directly related to the current being generated in the guard ring vicinity by impact ionization and can be correlated to the breakdown in figure 3.15.

Figure 3.17 show the electric field distribution at 1 μm under the guard ring for the three model under study at 400V. The electric field peak value are the lowest for the ATLAS actual design however the structure is also the largest. The two n-in-p model show different distribution of peaks with the highest one located in the small guard ring structure. The large guard ring structure exhibit more peaks with higher value.

Simulations also have shown that depletion for highly irradiated sensors is an ill defined concept as carrier concentration becomes very low in what is considered to be the undepleted zone, as seen on figure 3.13 and 3.14. Some low electric field (O(1000 kV/cm)) is present in the simulation in this region that is usually considered undepleted and charge deposited in this region could still be collected as its recombination probability is much lower than in the undepleted regions of an unirradiated sensor. Figure 3.18 show the electric field distribution as a function of the depth under a pixel for the ATLAS standard model irradiated at a fluence of $5 \times 10^{15} n_{eq} cm^{-2}$. The electric field in the undepleted portion of the bulk, from 100 to 300 μm is only an order of magnitude lower than in the undepleted region. Since the velocity of carrier saturate and is reduced by an order of magnitude in the high electric field present in the depleted region, the drift in each zone would be almost equivalent.

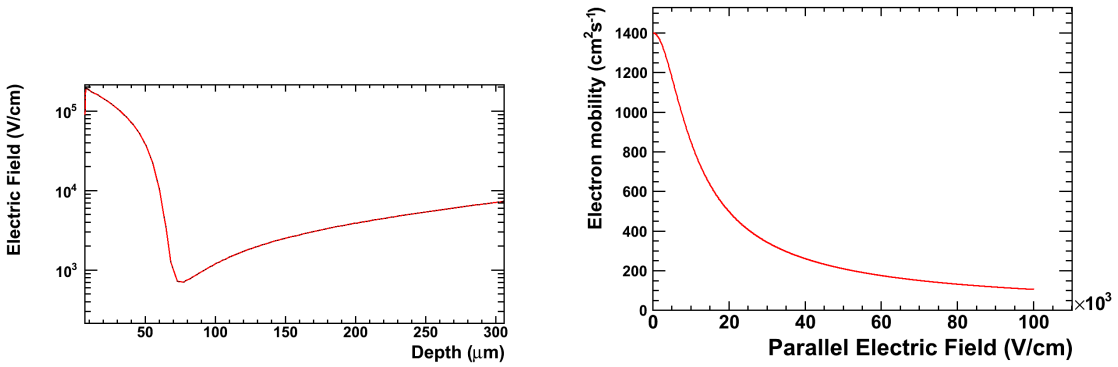

FIGURE 3.18 – Electric field magnitude in the bulk of an ATLAS sensor, under a pixel, irradiated to a fluence of $5 \times 10^{15} n_{eq} cm^{-2}$ and mobility as a function of parallel electric field for electrons

The simulation of the guard ring structure after irradiation suggests that n-in-p structures should offer better resistance to irradiation at high fluences as the guard ring structure will continue to be effective during all the detector's operation time. This also suggests that placing a guard ring structure on the n side of the n-in-n pixel design could allow operation after exposition to the required dose. The small guard ring design endure an higher breakdown voltage when compared to the large guard rings design. Behavior after irradiation is however very similar. Smaller guard rings exhibit lower electric field peak in average, but the structure simulated is ideal. In reality, smaller guard rings might have higher probability of defects in process, thus creating weak spot where breakdown could occur. The highest peak was also found in the small guard ring model.

Tu be used in IBL conditions, the ATLAS standard structure dead region must be reduced to the level of the n-in-p structures. Simulation have been performed to explore the possibility of reducing the dead area of the sensor that span from the edge to the first guard ring. Simulation for edges ranging from of 100 to 300 μm have been performed. Figure 3.19 shows the electron concentration for an unirradiated sensor of different dead edge widths.

We can observe in these simulation that there is no correlation between guard ring behavior and the width of the zone between the outer guard ring and the cutting edge of the sensor. The potential and electric field distribution along the guard ring was found to

be also the same for each model. After irradiation and SCSI, an undepleted zone remains visible even for a small edge width of 100 microns. Reduction of the dead edge outside the guard ring structure appear to be a valid method to reduce the inactive area of the sensor. Figure 3.20 show the the majority carrier concentration profile at half depth in the three models under study, unirradiated, as a function of distance from the cutting edge. The lateral depletion limit can be seen for each model as the distance where the concentration start to fall rapidly. This figure shows that the lateral depletion seems to be little influenced by the type of guard ring structure used in a sensor.

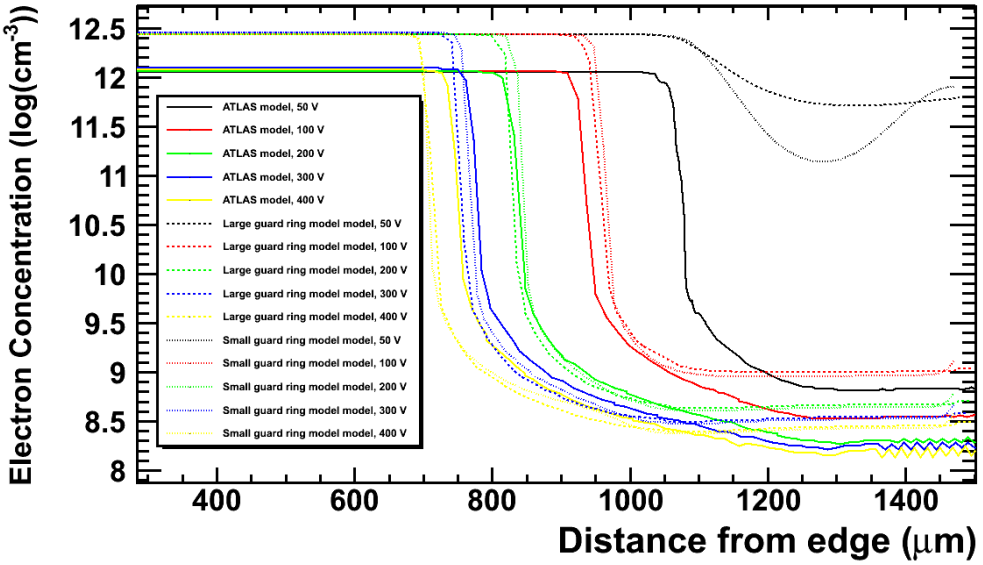

FIGURE 3.20 – Comparison of lateral depletion for the three model of guard ring structure under study

The guard rings structure itself also represent an inactive area of the sensor and must be reduced, The actual ATLAS pixel sensor has been simulated with 0,1,3,4 of the outer guard ring removed. Figure 3.21 shows the bias voltage distribution taken by the guard rings for the different simulated structures with an applied bias of 500 V. It is shown that the bias voltage of the guard rings are almost the same as before their removal, with the outer guard rings moving closer to ground while never reaching it in the case where 6 or 10 guard rings were removed. The rest of the transition occur on the surface of the safety

edge. Once the guard ring structure get smaller than the lateral depletion zone, it loses its effectiveness at ensuring a complete transition from high voltage to ground. This limits the number of guard rings that can be safely removed from the actual structure.

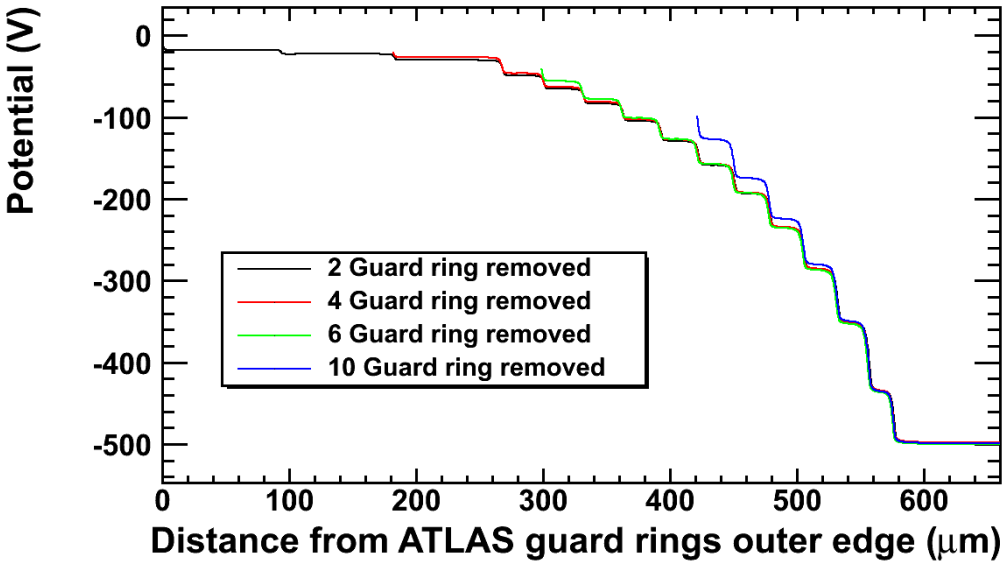

FIGURE 3.21 – Simulated bias voltage distribution for actual ATLAS sensor with 2,4,6 and 10 of the outer guard rings removed

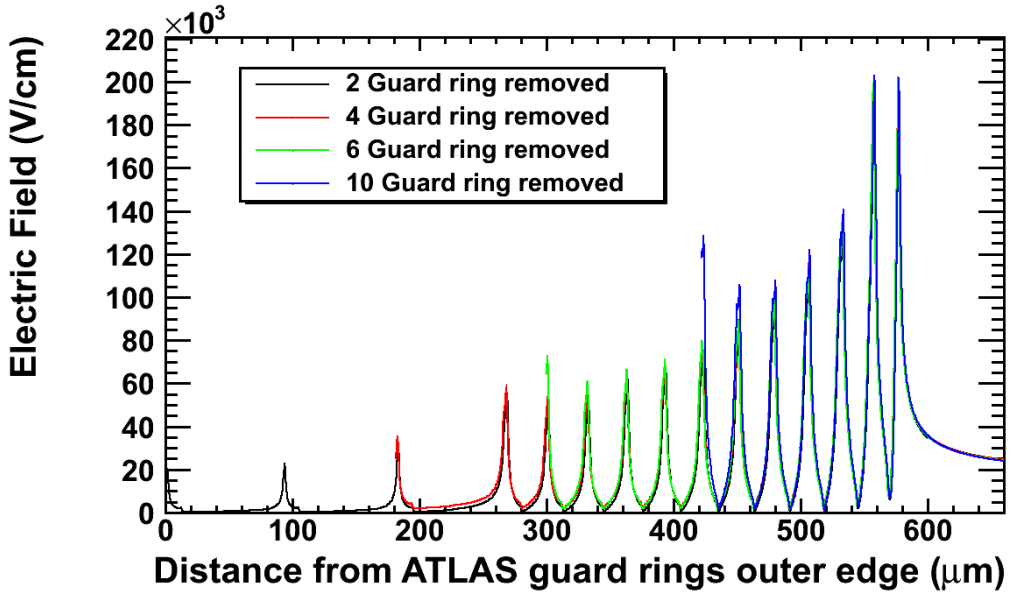

FIGURE 3.22 – Simulated electric field distribution, 0.1 μm under surface, for actual ATLAS sensor with 2,4,6 and 10 of the outer guard rings removed

Figure 3.22 shows the electric field distribution at 0.1 μm under the guard rings for the different simulated structures with an applied bias of 500 V. The high peak next to outer guard ring is due to the rapid bias voltage drop from outer guard ring to passivated edge as the lateral depletion limit pass the outermost guard ring to extend in the outer edge of the structure. Removal of 4 guard rings could be use to reduce the width of the actual structure as the electric field at the outer of remains small compared to the breakdown electric field in silicon, valued at 300 kV/cm. If more guard rings are removed , the breakdown probability is increased by the incapacity of the guard ring to provide a complete transition from edge to pixel voltage. The peak value at the outer edge of the guard ring can become big enough to generate a breakdown and electric field present close to the edge can cause excessive leakage current.

Thinning of a pixel sensor can be beneficial to a detector in high fluence environment. Charge collection occurs in a small region as trapping time becomes smaller than the drift time of the charge deposited in the sensor. Charge deposited deeper in the sensor can never reach the collecting electrode and do no generate signal, leaving most of the sensor useless.

Lower bias voltage is needed and trapping is reduced due to small travel distance of holes and electrons in the bulk in thinner sensors. I performed simulation of the actual ATLAS pixel design with a thickness of 150, 200 and 250 μm. Figure 3.23 shows the electric field distribution 1 μm under the pixels. for a bias voltage of 150 V. We can observe that the peak electric field at the guard ring, for the same bias voltage, is not affected by the thickness of the sensor. This is because the field distribution is mainly related to the lateral depletion depth of the sensor. The lateral dimensions of the sensor are the same so the guard ring behave similarly in thinner and thicker sensors. The mean electric field inside the sensor is however higher due to reduced thickness. Lateral depletion at half-height, defined as the distance from edge where the silicon is undepleted, is 700 μm for the 150 μm thick model, 540 μm for the 200 μm thick model and 480 μm for the 250 μm thick model.

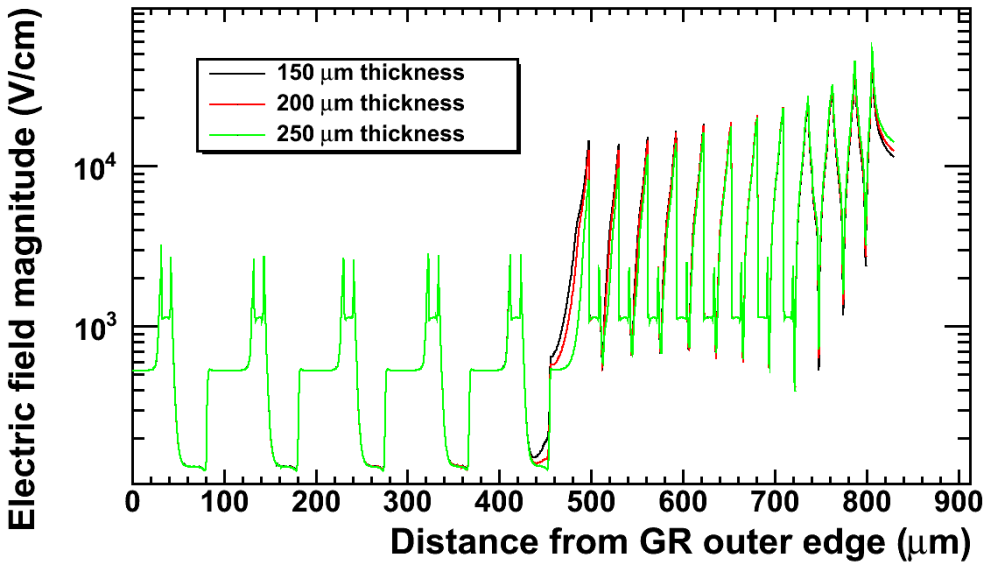

FIGURE 3.23 – Electric field 1 μm under the guard rings for different ATLAS pixel sensor thickness

For a given constant bias voltage, we notice that the depletion is more complete in the thinner sensor as the electric field is higher. This means that a thin sensor could be operated at lower voltage, with a guard ring structure behaving like in a thicker sensor. The breakdown occurring in guard rings are due to high electric field at the junction edge of the guard rings. Since this electric field distribution is not dependent on thickness, guard

ring structure are more effective in thinner sensor.

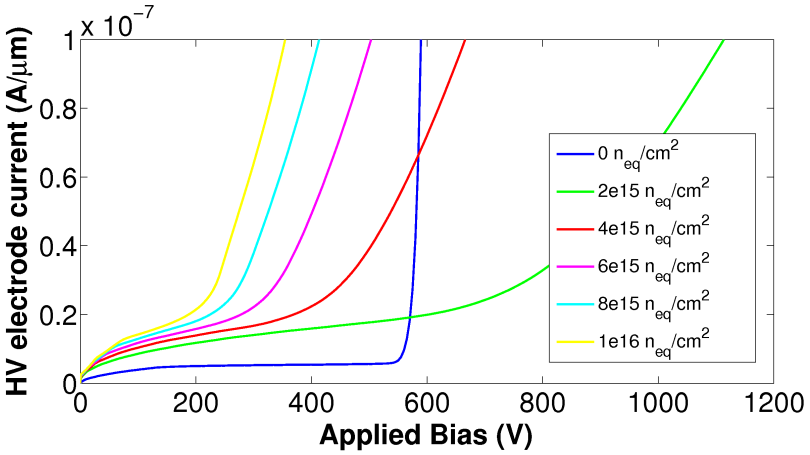

(a) ATLAS actual design, n-in-n

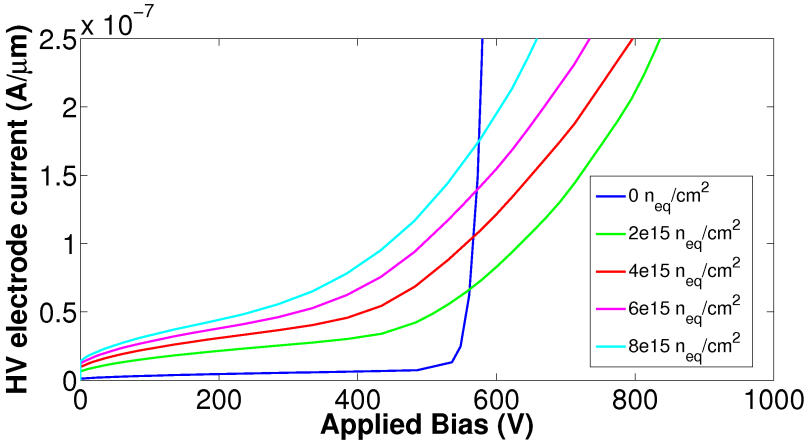

(b) Large guard rings, n-in-p design

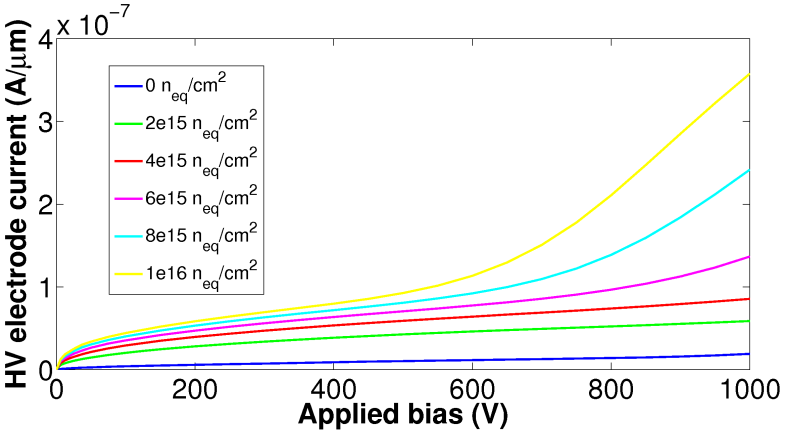

(c) Small guard rings n-in-p design

FIGURE 3.15 – Simulated backplane current vs bias potential, for different irradiation doses

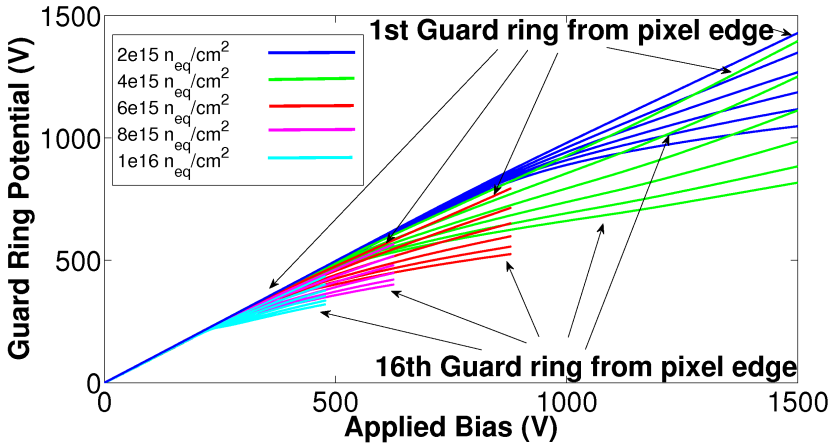

(a) ATLAS actual design, n-in-n

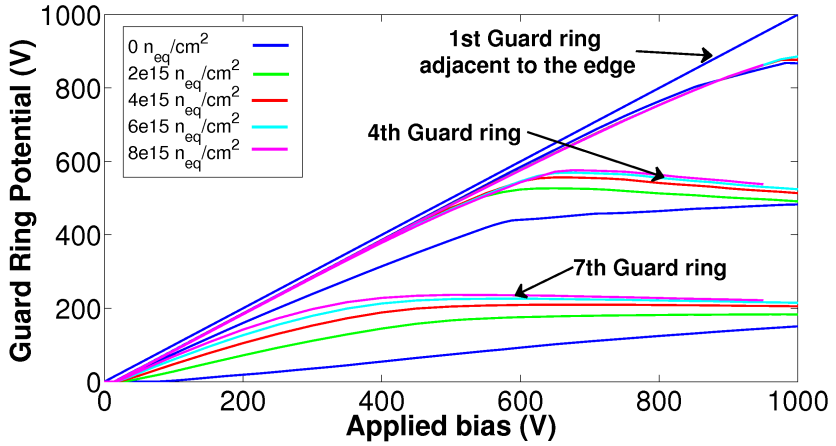

(b) Large guard rings, n-in-p design

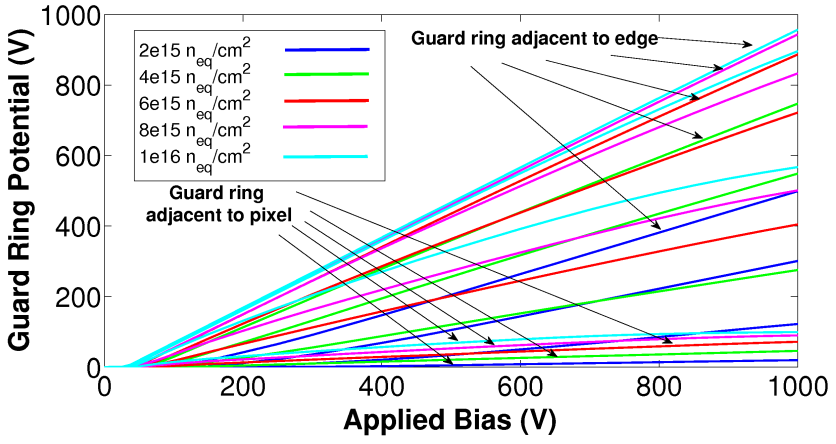

(c) Small guard rings n-in-p design

FIGURE 3.16 – Simulated guard rings potential vs bias potential, for different irradiation doses. Bias on, high voltage electrode, pixels at 0V

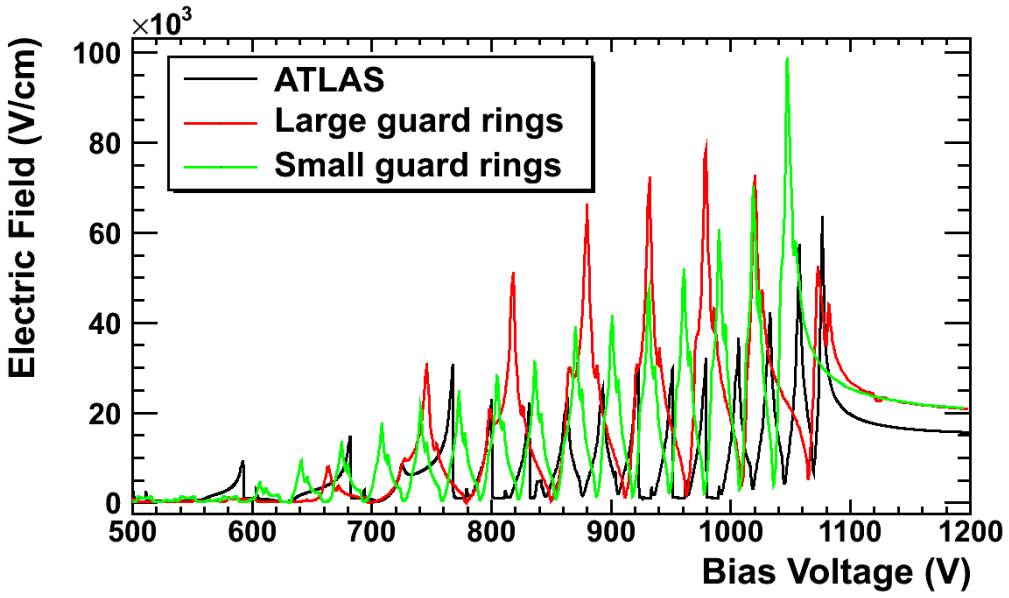

FIGURE 3.17 – Comparison of the electric field at 1 μm under the guard rings for the large ring and small ring n-in-p model and the ATLAS actual n-in-n model for a bias voltage of 400V.

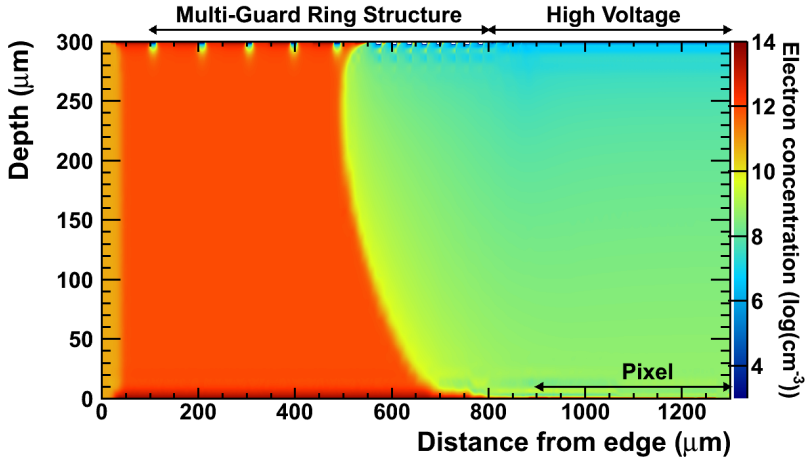

(a) 100 μm edge width

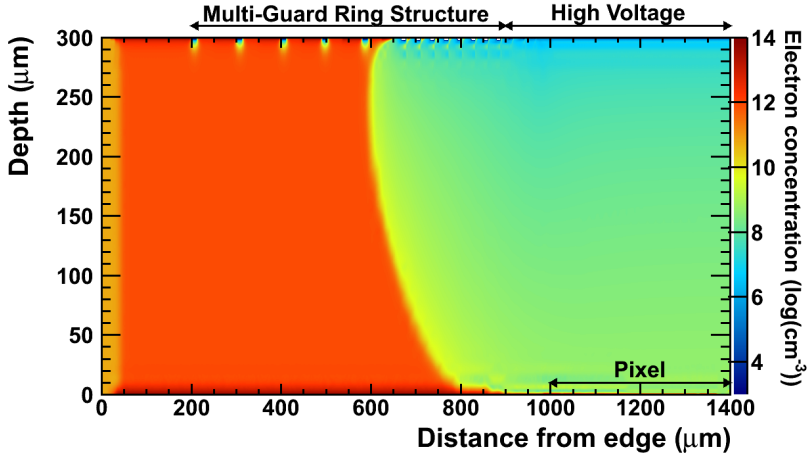

(b) 200 μm edge width

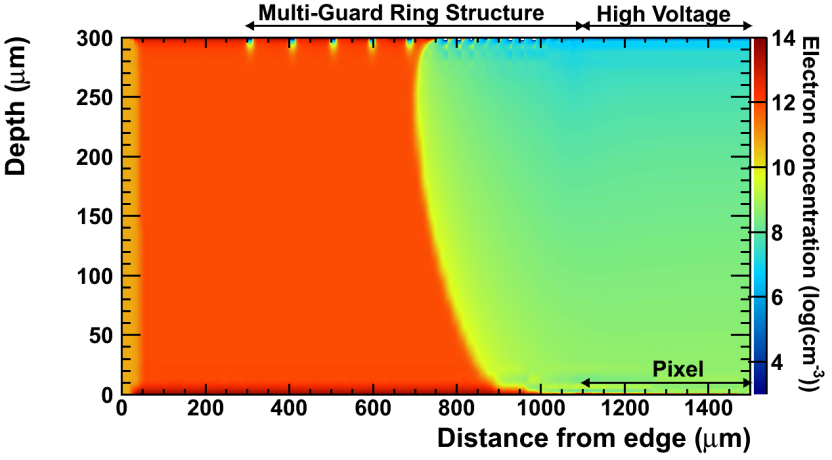

(c) 300 μm edge width

FIGURE 3.19 – Simulated electron concentration profile for an unirradiated ATLAS n-in-n pixel sensor for various dead edge width

3.3.3 The Slim Edge Guard Ring structure

It was proposed by the ATLAS Planar Pixel Sensor upgrade group to reduce further the inactive area of the n-in-n sensor by shifting the pixel under the pixel area, as shown in figure 3.24. This would reduce the area uncovered by pixel and consequently allow much smaller inactive edges.

This structure was simulated to obtain to understand the effects of this shift on the performance of the sensor. The model used was the ATLAS n-in-n standard guard ring shifted under the pixels by 100,200 and 400 μm. The edge was 500 microns but reduction of the dead edge does not affect the guard ring behavior and the result can be valid as long as the width of this edge stay within the 100 microns mentioned earlier. Bias Voltage was 150 V and detector thickness was 300 μm. Figure 3.25 show the electric field magnitude in the region of the edge pixel where overlap occur, for a shift of 100 and 200 μm. The presence of the guard ring affect the distribution of the field under the pixel and the field is weaker in the section of the pixel overlapping the guard ring. Figure 3.26a show the potential distribution in the 200 μm shift case. We can observe that the potential gradient in the overlap region will drag charge away from the pixel as the drift closer to it. This is because this part of the pixel is in the lateral depletion zone that is normally located outside the volume of the edge pixel. This region is the region where the Ramo potential of the edge pixel, shown in figure 3.26b, undergo the largest variation. This will lead to loss in charge collection. This can still be a beneficial method to reduce the edge of the sensor while keeping larger guard ring structures if the signal collected is still sufficient to obtain a good trigger efficiency.

The big advantage of the slim edge structure comes after irradiation. After SCSI, the depletion occurs from the pixel side and the guard ring become less efficient. The electric field distribution at the edge pixel is then changed and the problem of the lateral depletion zone go away. Figure 3.27 show the electric field configuration in the 200 μm shift model after a dose of $10^{15} n_{eq} cm^{-2}$ at a bias voltage of 1000 V.

As the detector at IBL and SLHC will be during its lifetime irradiated, this strategy is a good compromise to obtain a slim edge structure meeting the requirements of the IBL

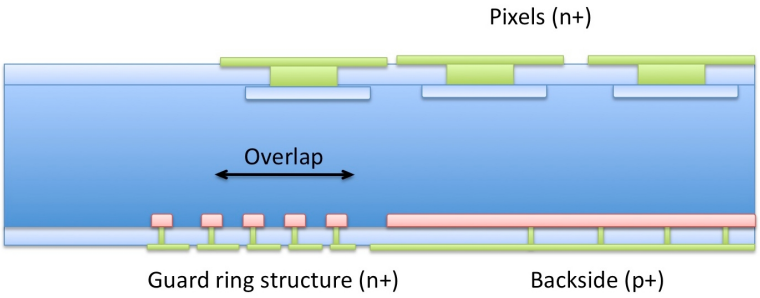

FIGURE 3.24 – Slim edge Multi Guard Ring structure showing the overlap of the pixel with the guard rings on the backside

while keeping a large Multi-Guard Ring Structure. This guard ring structure was proposed for the sensor candidate sensor for the IBL project. The shift is 250 μm in the case of the so called "Slim-Edge" candidate , and 100 μm in the case of the conservative candidate. Test structure with FE-I3 geometry were produced in the PPSU09 sensor production and were used in beam test to study the properties of the edge pixels. Results will be presented in the next chapter. The simulation made an important prediction on the behavior of the slim edge structure that were demonstrated in experiment : The loss of charge at the edge in the overlap zone between the pixel and guard rings. This phenomenon was later observed experimentally. The work done on TCAD simulation of guard ring structure has contributed to the design of the various planar pixel structure proposed for the upgrade projects. The simulation provided guidelines on the design change that would affect or not the performance of the detector. In the next chapter, a comparison of TCAD results with experimental data will show the good performance of the simulation in predicting device behavior before and after irradiation. Monte-Carlo Simulation of the charge transport was also performed to replicate the charge collection behavior observed experimentally.

For the detector irradiated at super LHC fluence ($5 - 10 \times 10^{15} n_{eq} cm^{-2}$), new physical phenomenon we observed experimentally. In the next section, I present a model that was elaborated using TCAD simulation to emulate the behavior of highly irradiated sensors.

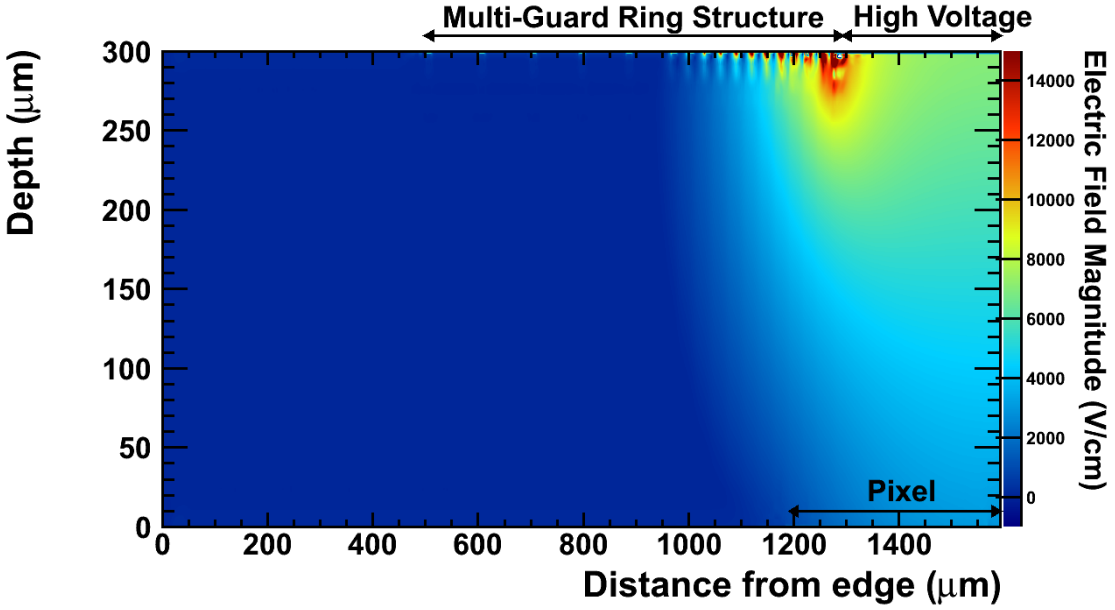

(a) 100 μm shift

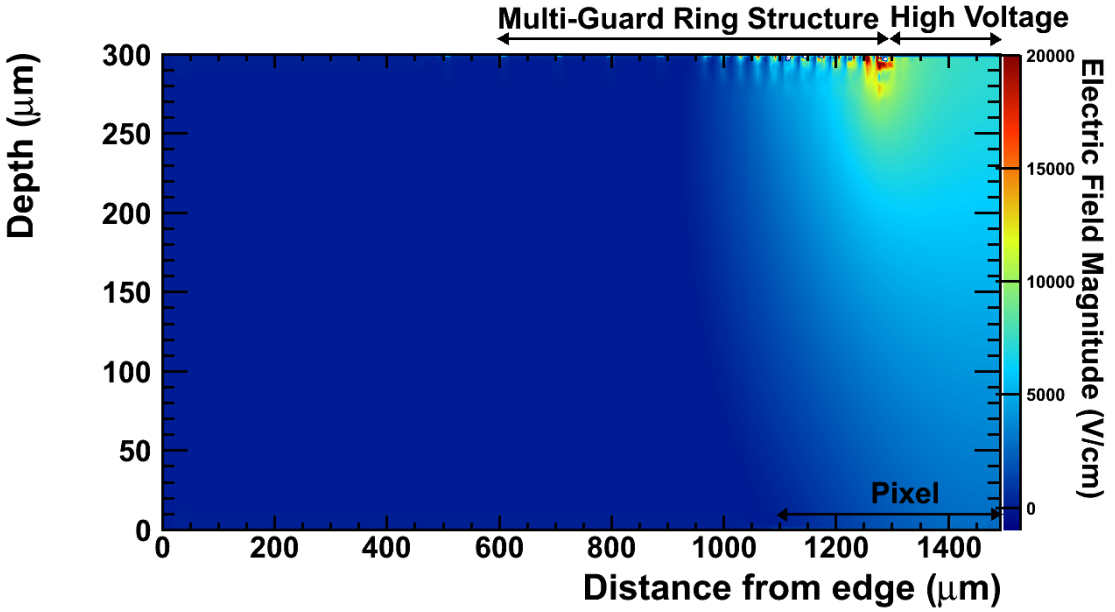

(b) 200 μm shift

FIGURE 3.25 – Electric field magnitude in Slim edge Multi-Guard ring structure with a shift of 100 and 200 μm

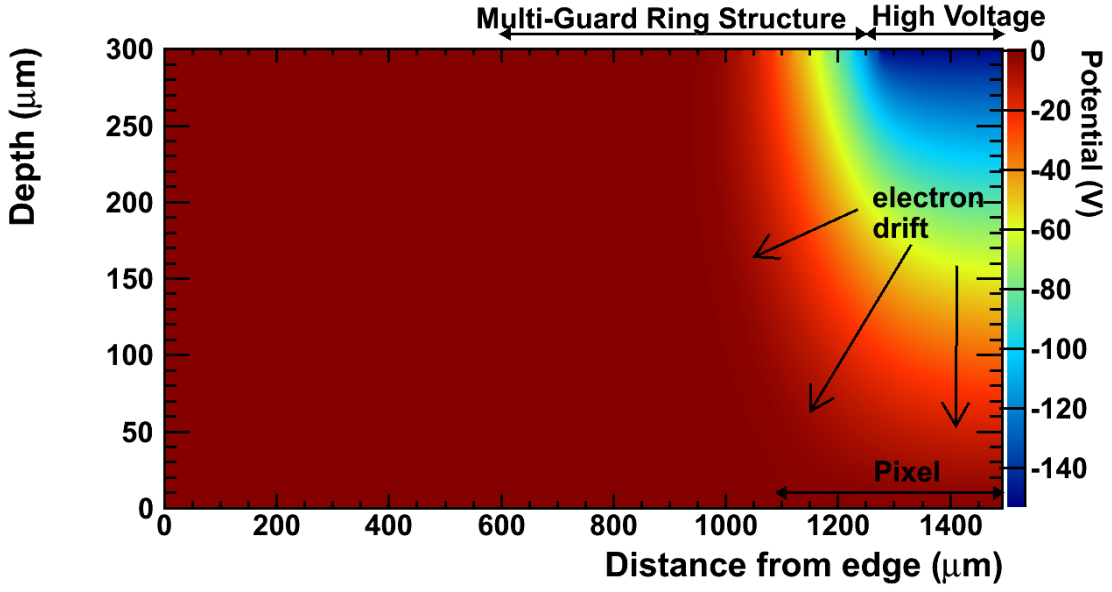

(a) Potential distribution

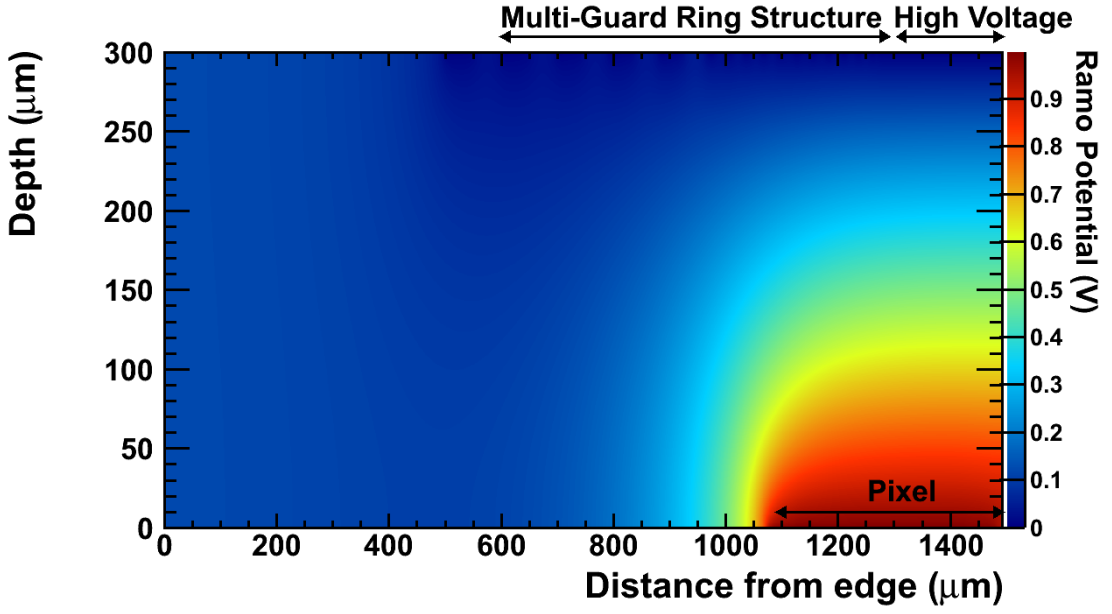

(b) Ramo Potential distribution

FIGURE 3.26 – Potential and Ramo Potential distribution in a Slim edge Multi-Guard Ring structure with a shift of 200 μm. Arrows show the drift direction of electrons

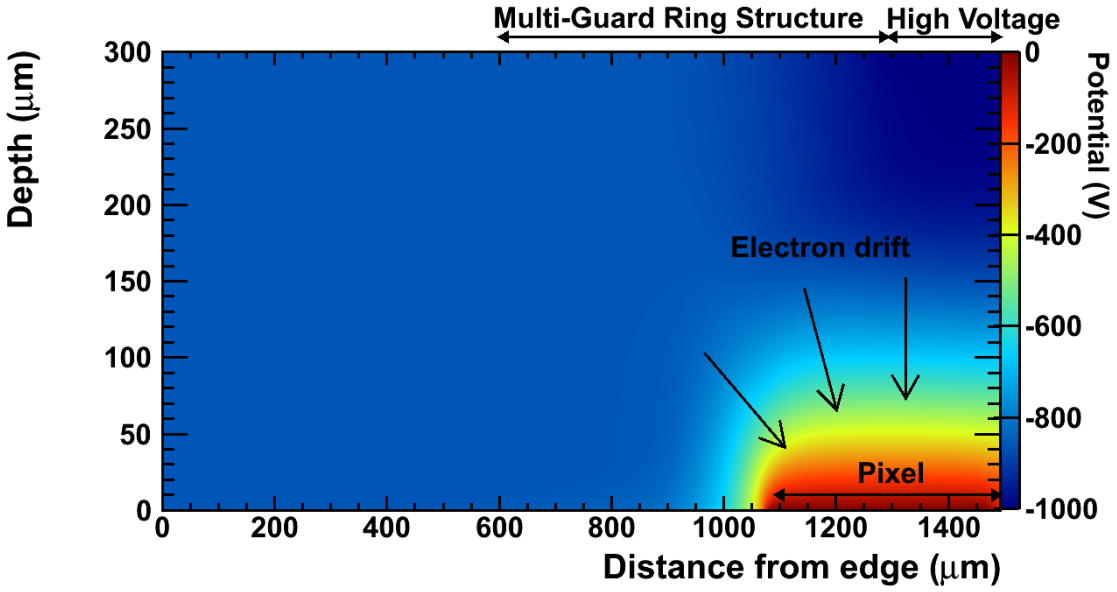

(a) Potential distribution

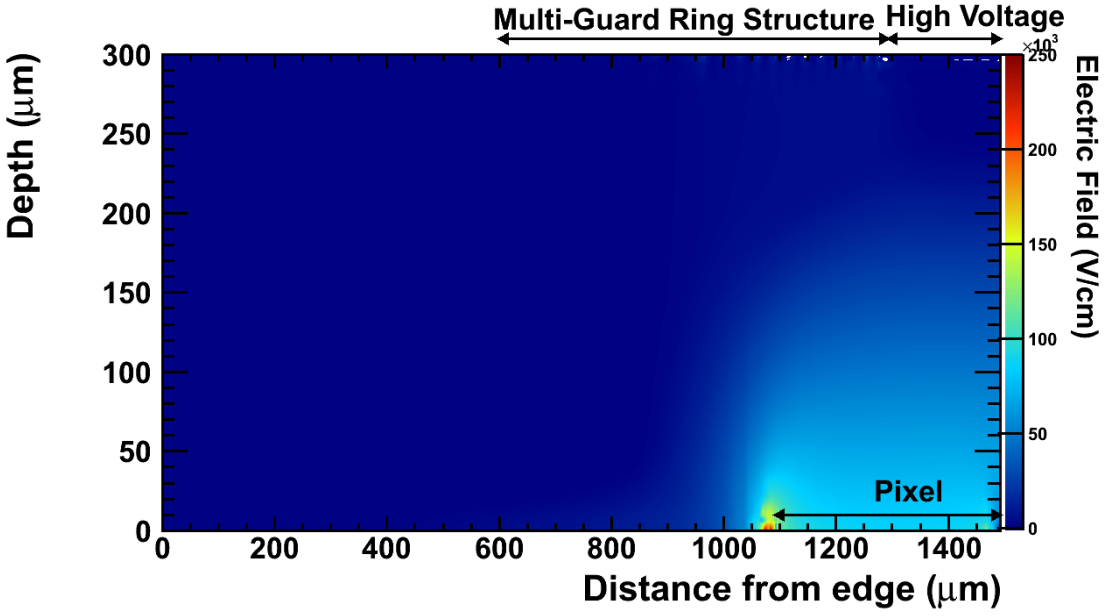

(b) Electrifc field distribution

FIGURE 3.27 – Potential and Electric field distribution in a Slim edge Multi-Guard Ring structure with a shift of 200 μm after an exposition to a fluence of $10^{15} n_{eq} cm^{-2}$. Arrows show the drift direction of electrons

3.4 The charge amplification mechanism in highly irradiated silicon sensors

Charge collection efficiency (CCE) of silicon planar pixel sensors used for charged particle detection in high energy physics is known to be reduced by increased exposition to radiation damage. However it has been observed experimentally [47; 48] that CCE of planar pixel sensors exposed to fluences of the order of 10^{15-16} $n_{eq}cm^{-2}$ can be increased by applying higher bias voltage to the sensor. Figure 3.28 show an example of unexpected charge collection in 80 μm pitch, 140 and 300 μm thick n-in-p strip sensors. In this section , I present a set of TCAD simulations that have been performed to explore the possible mechanisms behind this anomalous charge collection observed after exposition to high fluences of diode and strip sensors.

The simulations were performed on simple geometries to explore the effects of impact ionization and trap-to-band tunneling on the transient behaviors of planar silicon sensors. A simple one dimensional diode geometry was simulated. Implants parameters used were obtained from measurements from the PPSU09 production. Two dimensional simulation of a strip sensor was also performed but the computing time required to perform a transient simulation was too large to obtain a large number of simulation in a reasonable time. For numerical accuracy, the 1D simulation considers a width of 250 μm with laterally uniform conditions. The TCAD simulation have shown poor convergence when aspect ration of the structure is far from unity. DC simulation for a fluence of 2×10^{16} $n_{eq}cm^{-2}$ for a bias voltage up to 3000 V, when numerically possible, was performed for a thick (300 μm) and thin (140 μm) sensor,

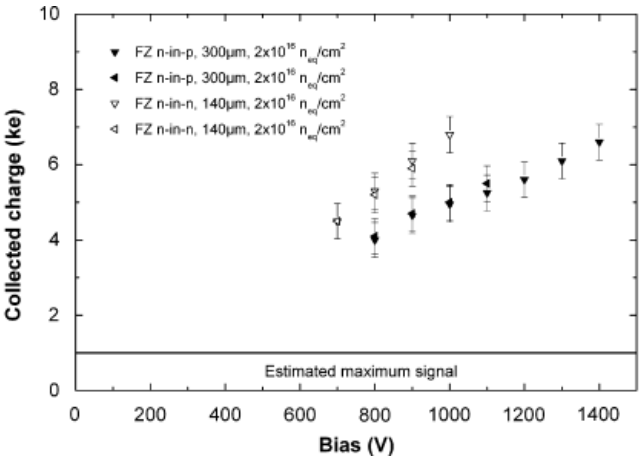

FIGURE 3.28 – Experimental charge collection in irradiated thin and thick n-in-p strip sensors showing evidence of charge amplification [47]

with impact ionization switched on and off, then with trap-to-band tunneling switched on and off. This allows to see the effect of each mechanism on the behavior of the sensors.

Transient simulation of the device was also performed. A 2 ns triangular 1060 nm laser pulse was sent perpendicular to the device surface. The TCAD software then calculates the ionization by the laser, mostly uniformly deposited in the bulk depth, and perform a transient simulation over 40 ns at different bias with the trap-to-band tunneling and the impact ionization turned on and off. The signal we obtain from the simulation is then integrated, with the pedestal subtracted, to obtain the collected charge. From simulation, we also obtained the initially deposited charge and we can then compute the CCE using equation (3.7).

$$CCE = \frac{Q_{collected}}{Q_{deposited}} \tag{3.7}$$

The DC simulations were performed on a non-irradiated diode, then on a heavily irradiated diode to a fluence of 2×10^{16} $n_{eq}cm^{-2}$. Fig. 3.29 shows the current circulating in the high voltage electrode for a thick and a thin diode with the impact ionization and trap-to-band tunneling successively turned off in the simulations. This allows us to see the contribution of the different physical phenomena to the DC characteristics of the sensors. Recombination lifetime was set to 1×10^{-5} s for a better simulation of leakage current in high resistivity silicon used for pixel sensors [49].

This parameter is not taken into account in irradiated diode simulation as it is overridden by the defect introduction model . Fig. 3.29(a) shows the IV curve before irradiation. A hard breakdown occurs at high voltage with a steep increase in leakage current. The contribution to leakage of impact ionization is negligible before breakdown, explaining why no charge multiplication is observed in non-irradiated sensors. The breakdown occurring in the diode is located inside the bulk under the implant, as electric field there becomes too elevated, as can be seen in the pre-breakdown electric field profile in Fig. 3.30(a), causing hole multiplication to occurs. Since this is a one dimensional simulation, no implant edge effects are considered. The contribution of trap-to-band tunneling to leakage current in the diode becomes important even for low bias voltage. As electric field increases in the bulk

of the sensor , this mechanism contribute to more and more of the leakage leading to this resistive behavior after depletion. Fig. 3.29(b) shows the IV curve for the same sensors after irradiation. The contribution of trap-to-band tunneling to leakage current becomes significant at higher bias voltages than before irradiation. The breakdown occurring in the sensors before irradiation is replaced by a soft breakdown where the current rises at a much lower rate even if the same high field region is observed in the thin diode electric field profile in fig. 3.30(b). This allows the operation of the sensor in this regime where multiplication effects are to be expected. This quenching of the avalanche mechanism can be explained by the increased trapping in irradiated sensors, where the mean free path of holes is reduced. This prevents the free holes of creating an avalanche and reduces the contribution from impact ionization to leakage current.

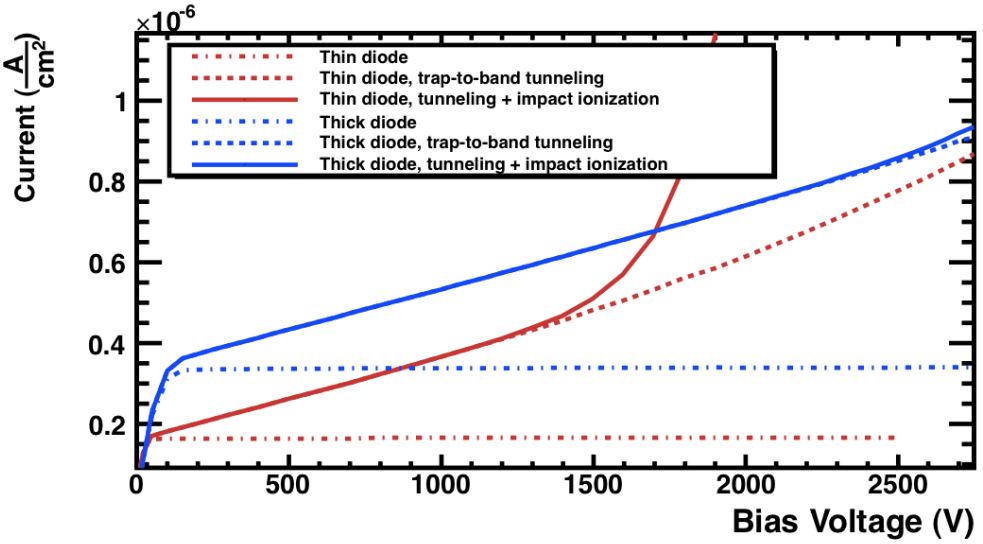

(a) Current versus bias voltage, non-irradiated 1D diode

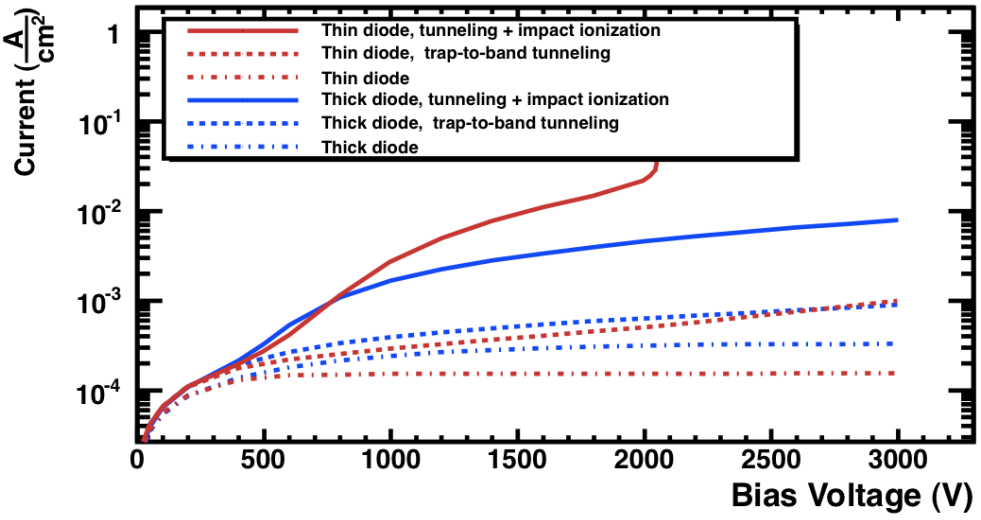

(b) Current versus bias voltage, 1D diode $\phi_{eq} = 2 \times 10^{16}\ n_{eq}cm^{-2}$

FIGURE 3.29 – Comparison of Current versus Voltage curves before and after irradiation.

The results of the transient simulation can be seen in fig. 3.31. The multiplication effect can be seen only at high voltage in non-irradiated sensors (fig.3.31(a)), much beyond the breakdown voltage. Charge collection follows the normal behavior for non-irradiated sensors, saturation at a CCE of 1. The multiplication effect in irradiated sensors can be seen in fig. 3.31(b). Trapping should normally prevent some charge of being collected. A small

part of the deposited charge is recovered by trap-to-band tunneling and impact ionization further improves the charge collection efficiency to a factor superior to 1. The electric field profile at a bias in the multiplication regime, as seen in fig. 3.30(b) explains the presence of such effect in the irradiated sensor. In this figure is represented the electric field in the bulk of the diodes at a bias voltage close to breakdown, for non-irradiated sensors, and in the multiplication regime for irradiated sensors. A high electric field, of the order of 100 kV/cm, exists in the bulk of the irradiated sensors leading to de-trapping and multiplication in the bulk , as seen in fig. 3.31(b). It should be noted that de-trapping alone cannot explain charge collection efficency over 1. For the non-irradiated diode, the electric field profile shown in fig. 3.30(a) shows the pinching if the electric field close to the readout implant that eventually cause a hard breakdown , as seen in fig. 3.29(a), at higher bias voltage. This breakdown prohibits the operation of non-irradiated diodes at such bias voltage. In case of irradiated diodes, the attenuation of impact ionization by trapping allows operation at higher voltage allowing to reach the multiplication regime.

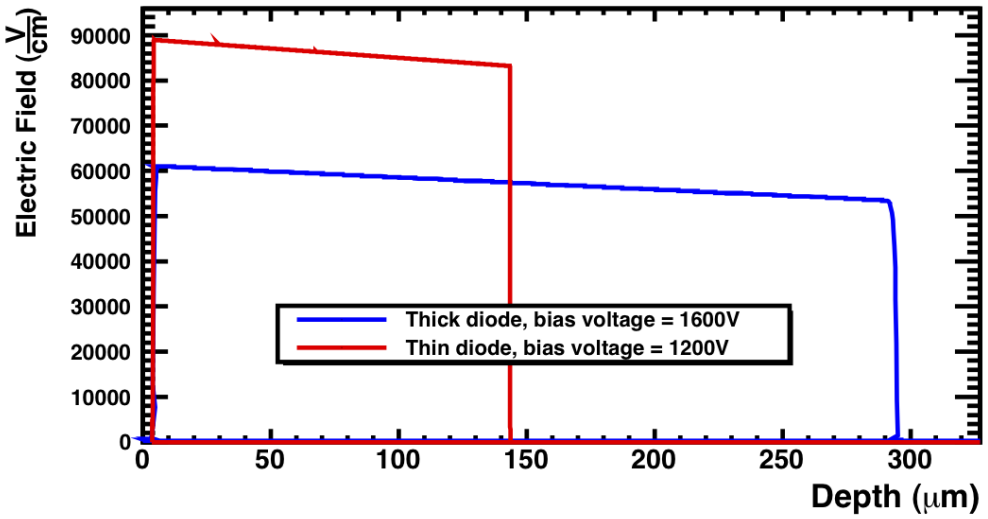

(a) Electric field at bias before breakdown, non-irradiated diodes

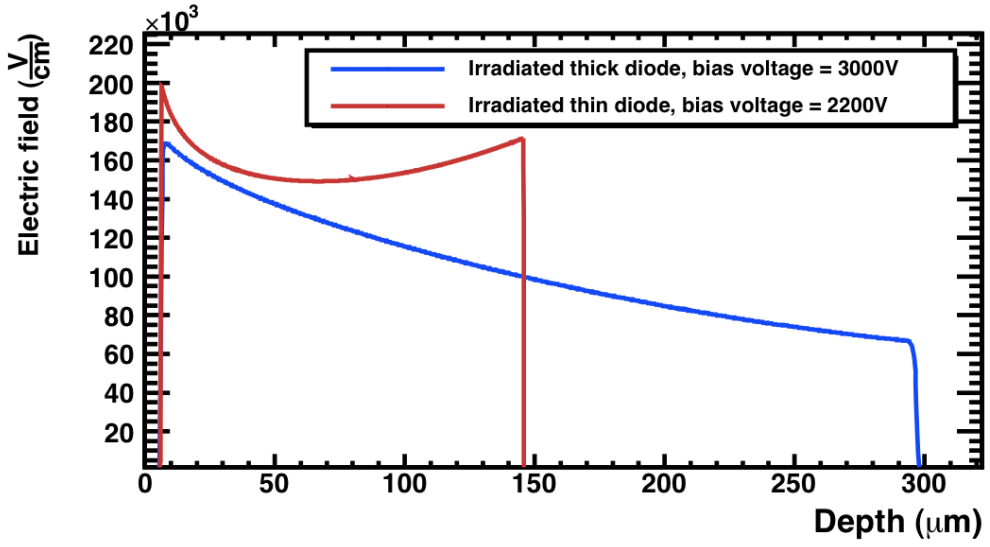

(b) Electric field at a bias voltage in the multiplication regime, irradiated diodes $\phi_{eq} = 2 \times 10^{16}\ n_{eq}cm^{-2}$

FIGURE 3.30 – Comparison of Electric field magnitude at a possible operation bias voltage before and after irradiation.

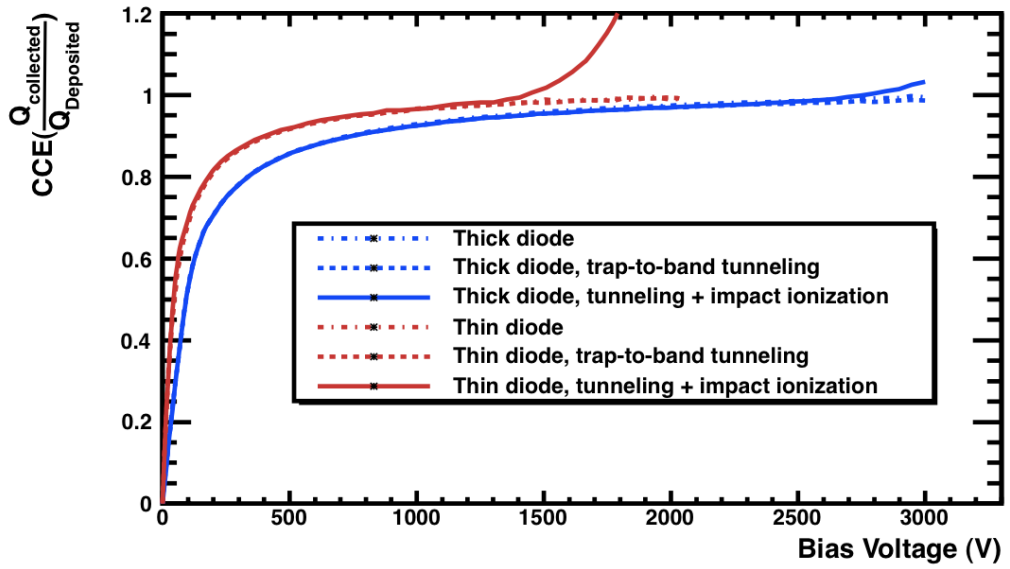

(a) CCE versus bias voltage, unirradiated 1D diode

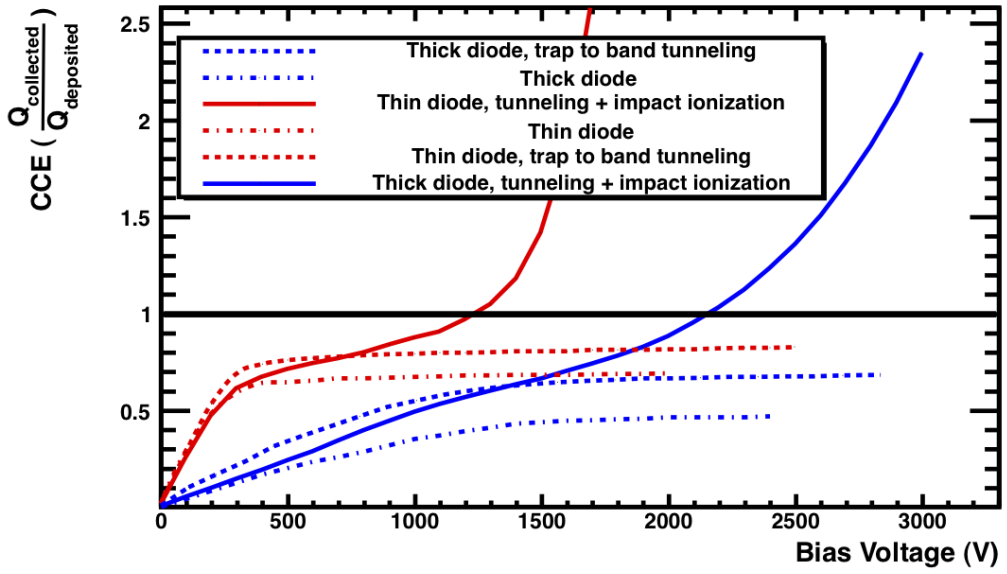

(b) CCE versus bias voltage, 1D diode $\phi_{eq} = 2 \times 10^{16}\ n_{eq}cm^{-2}$

FIGURE 3.31 – Comparison of CCE curves before and after irradiation.

The simulation performed demonstrates that the parametrization of radiation damage in terms of effective defects introduction, combined with trap-to-band tunneling and impact ionization qualitatively explains the charge recovery effect observed experimentally in highly irradiated n-in-p diodes. The high electric field present at the readout implant causing multiplication of free charges, combined with increased de-trapping caused by the

bending of the band gap structure by the electric field and the attenuation of the multiplication by increased trapping provides a physical explanation to the observed behavior of these diodes.

Chapitre 4

From TCAD simulation to experimental data

TCAD simulation models presented in the last chapter require the input of a large number of parameters to obtain quantitatively comparable results. Process parameters determine the shape and concentration profile of the implants forming the guard rings and the readout electrodes. Quality of the silicon dioxide and silicon interface is represented by the surface charge used. The resistivity of the bulk and recombination lifetime of the defects present in the bulk affect depletion potential and leakage current magnitude. Experimentation on test structure and sensors can help to obtain the parameters needed to tune the simulation models and obtain quantitative results.

Accurate TCAD simulation can offer better understanding of the behavior of the ATLAS existing and future pixel sensors. The inclusion of radiation damage behavior and edge effects using knowledge from TCAD simulation in the digitization of pixel sensors used in the ATHENA simulation of the ATLAS detector can improve the realism of the simulation and help understand effects observed during the lifetime of the inner detector. A Monte-Carlo charge transport code was built to study transient behavior of sensor using TCAD electric field and Ramo potential simulation as input and provide more information on sensor detection properties. As mentioned in the previous chapter, a sensor production including designed structure influenced by our TCAD simulation presented in this work was delivered to us in 2010. This production included many test structures to study our TCAD models. In this chapter, I present the experimental work that was performed to

calibrate the simulation models used in this work. Part of the work behind this has been to assemble test bench for low noise,low current and high voltage DC and transient characterization of silicon sensors. Clean room and test beam measurements were used to calibrate the parameters used in simulation and get more knowledge on the physics describing guard rings structure.

The PPSU09 production contained ATLAS pixel structure with FE-I3 geometry with many variations of slim edges structure and reduced number of guard rings. These sensors were bonded to FE-I3 chip and tested before and after irradiation with high energy protons and neutrons in test beam at CERN SPS and DESY electron synchrotron. The EUDET telescope was used to provide track information used to analyze the pixel sensor data. Results from reconstruction and analysis of these sensor have been used to validate predictions done using TCAD simulation. Finally , a digitization model for the FE-I3 and FE-I4 planar pixel sensors candidate for IBL was developed using knowledge gathered from GEANT4 Monte-Carlo and TCAD simulation. The GEANT4 simulation of the EUDET telescope setup was used to simulate test beam conditions including digitization method and was used to validate the model. Comparison of test beam data and simulation data show good agreements and reproduce well edge and radiation damage effects that will occurin the ATLAS detector after long operation time.

4.1 Experimental validation of TCAD simulation

The PPSU09 production contained a set of test structures that we included for to calibration of TCAD simulation models. Table 4.1 show the structure and their experimental purpose and figure **??** show the layout of the wafer for the n-in-n production.

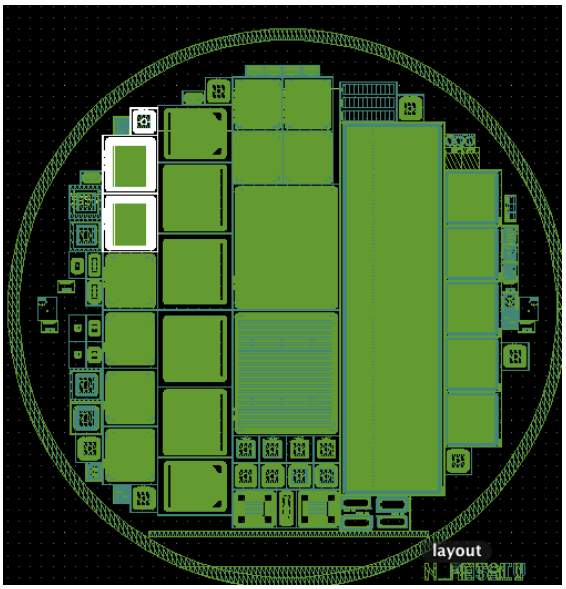

FIGURE 4.1 – N-in-N PPSU09 production wafer

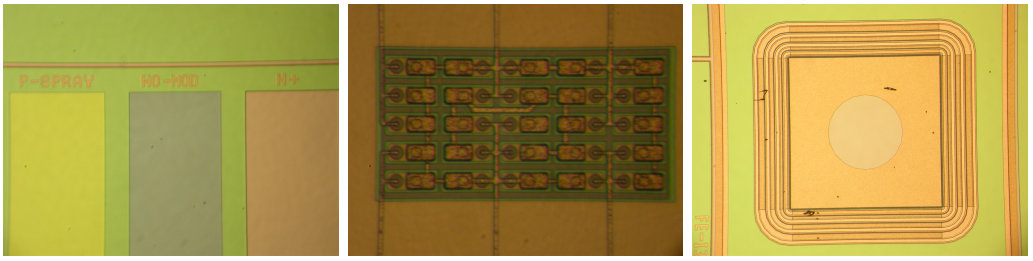

(a) doping profile structure (b) Inter-pixel capacitance structure (c) LAL diodes

FIGURE 4.2 – Test structure inserted in the PPSU09 production

The main goal of the production was to produce prototype of sensors with reduced edge for the IBL ATLAS pixel sensor. Several FEI3 pixel structure with guard ring removed were inserted in the production. The main detector occupying most of the wafer is a FEI4 sensor. The n-in-p production contained :

- 3 FE-I3 standard small guard ring design , p-spray
- 3 FE-I3 standard small guard ring design, moderated p-spray
- 3 FE-I3 small guard ring design, 8 guard rings, p-spray
- 3 FE-I3 small guard ring design, 15 guard rings, p-spray

TABLE 4.1 – Test structure inserted in PPSU09 production

Structure	Description	Purpose
Doping profile structure	Three 1.9 $mm \times 8.9$ mm zones with n+, p-spray and moderated p-spray implants on front side and p+ implant on backside. Figure 4.2a	Atomic Force Microscopy, Spreading Resistance Profiling (SRP) and Secondary Ion Mass Spectroscopy (SIMS).
Inter-Pixel Capacitance structure	5×5 pixel matrix surrounded by a standard guard ring structure. First neighbors of the central pixel are connected together and independently the second neighbor also. Pixel size of 50, 250 and 400 μm have been used. Figure 4.2b	Inter-pixel capacitance measurement in clean room.
LAL diodes	6×6 mm diodes with 1 to 4 large contactable guard rings. Figure 4.2c	Leakage current and guard ring potential measurement before and after irradiation.

– 1 FE-I4 small guard ring design, p-spray

– 1FE-I4 small guard ring design, moderated p-spray

The n-in-n production contained :

– FE-I3 ATLAS standard guard ring with 3,5,11 and 13 outer guard ring removed

– FE-I3 ATLAS standard guard ring with pixel shifted stepwise by 50 microns in 8 steps

– FE-I3 ATLAS standard guard ring with pixel shifted by 100 and 200 μm

– FE-I4 4 chip module with ATLAS standard guard ring

– FE-I4 ATLAS standard guard ring

A second n-in-n production was submitted to produce IBL planar sensors. Two FE-I4 sensor were used in this production. The conservative model has the ATLAS standard guard ring structure with the 3 outer guard ring removed, as suggested in last chapter. The Slim Edges design has also reduced guard ring, but pixel are also shifted 250 microns under the guard rings. The measurement presented in the next section were performed using the

structure from these productions.

4.1.1 Doping profile measurements

TCAD simulation results such as guard ring potential and breakdown voltage are dependent on the doping profile of the structure. Knowing the doping profile of the different implant is therefore an important step to validate the simulation model and obtain accurate simulation. Various method exist to obtain the dopant concentration profile of an implant. The method can be divided in the stoichiometric and the electric methods. The stoichiometric methods consist in measuring the total amount of dopant in the silicon bulk. One method used is Secondary Ion Mass Spectroscopy. It consists in sputtering the surface of a sample using an ion beam and analyze the ejected secondary ions using a mass spectrometer. The speed at which the ion beam dig in the sample is known and the amount of ions of each species measured in the spectrometer as a function of time can be converted into a concentration versus depth profile. The SIMS doping profile were performed at CNRS-Meudon.

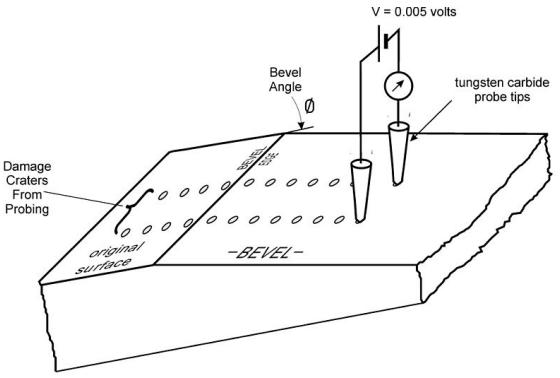

FIGURE 4.3 – Spreading Resistance Profiling technique

Two electrical methods were also used to characterize the implants. Electrical methods measure the carrier concentration in the implant, which is related to the electrically active dopant concentration. The first method used was Spreading Resistance profiling. This method consist in probing the local resistance between two very close point on the implant using small tungsten needles. The implanted structure is beveled with a small angle to reveal the implant at different depth. The needle probing is done at different points along the bevel to measure the local resistance between the two needle. The resistivity (ρ) of silicon vary with active dopant concentration hence the measure of the Resistance R can be converted into a active dopant profile. The distance from the surface on the beveled

plane can be converted to depth of the implant by multiplying the distance by the sinus of the bevel angle. Figure 4.3 show the principle of the measurement. The SRP measurements were performed by Evans Analytical Group. The second method that was investigated and developed was the Atomic Force Microscope Spreading Resistance Profiling (AFMSRP). This method is analogous to SRP done with the cantilever of an atomic for microscope that is electrically connected to an electrometer.

TABLE 4.2 – Comparison of SIMS and SRP method

Method	SRP	SIMS
Resolution	2%	5%
Sensibility (cm^{-3})	$10^{12} - 10^{20}$	$10^{15} - 10^{20}$
Sample size	several mm^2	>1 mm^2

The measurement were performed on the doping profile structure of the PPSU09 n-in-n and n-in-p production. This structure was designed to allow many kind of doping profile measurement methods on the same test structure. Three zone representing the readout n+ implant and the two p+ implant, one representing the p-spray implant and the other representing the non-moderated part of the moderated p-spray. The backside of the structure is covered by a p+ implant.

4.1.1.1 n-in-n production

Two samples , labeled 02-42 and 05-42, were tested using both SRP and SIMS method. figure 4.4 show to profile that were obtained from the SRP and SIMS method. The n+ implant corresponding to the pixels of the n-in-n sensors is shown in figure 4.4a. Measurement on both sample show the same profile showing a good uniformity of the phosphorus implantation on the different wafers of the production. Bulk effective dopant concentration of the sample can be determined from the concentration of active dopant far from the junction in the SRP measurement. For the n-in-n wafer sample tested, $N_{eff} = 4.15 \times 10^{12} cm^{-3}$ for sample 05-42 and $N_{eff} = 1.15 \times 10^{12} cm^{-3}$. Using equation 2.5 and 2.6, we can compute the expected depletion potential of a 285 μm sensor and compute its resistivity. Sample 02-42 has a resistivity of 4 $k\Omega cm^{-1}$ and a depletion voltage of 80V while sample 05-45 has

a resistivity of 2.2 $k\Omega cm^{-1}$ and a depletion voltage of 291V. The profile might however not have been performed deep enough to obtain bulk resistivity.

The p+ implant measurements, corresponding to the backside and guard ring implants in the n-in-n sensors, are shown in figure 4.4b. The pn junction is clearly visible by the drop in active dopant effective concentration as the silicon transition from p to n type. The depleted region of the junction is characterized by a low concentration as p and n type dopant compensate each other leading to a quasi null effective dopant concentration and very high resistivity. junction can be found at 582 nm for sample 02-42 and at 676 nm for sample 05-42. An order of magnitude is seen between the activated and total concentration of boron present in the implant possibly pointing to and incomplete activation of the implant or a compensating defect present in the bulk lowering the effective active dopant concentration. The effective active dopant for sample 02-42 in this measurement is $N_{eff} = 1.15 \times 10^{12} cm^{-3}$ for sample 02-42 and $N_{eff} = 1.85 \times 10^{13} cm^{-3}$ for sample 05-42. This yield to a resistivity of 248.4 Ωcm^{-1} and an unrealistic depletion voltage of 1300 V. This mean that doping profile was not performed deep enough to obtain bulk resistivity which is expected to be over 1000 Ωcm^{-1}. For sample 05-42, we obtain a bulk concentration of $N_{eff} = 1.15 \times 10^{12} cm^{-3}$ leading to a a resistivity of 4 $k\Omega cm^{-1}$ and a depletion voltage of 80V, compatible with sample 02-42 for the n implant measurement.

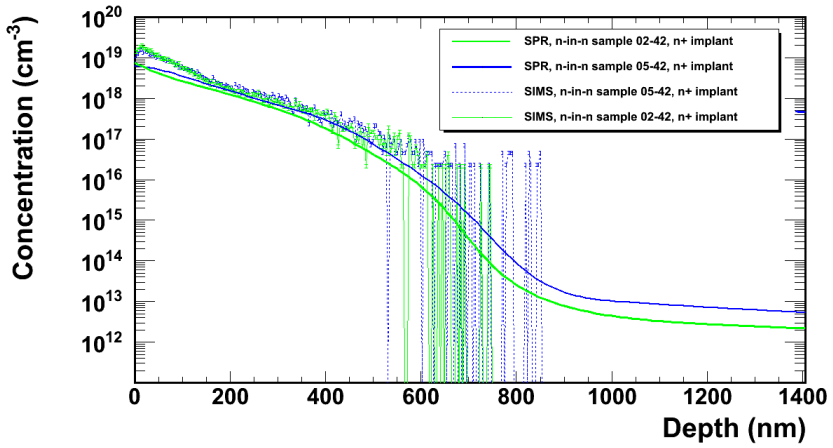

(a) N+ implant

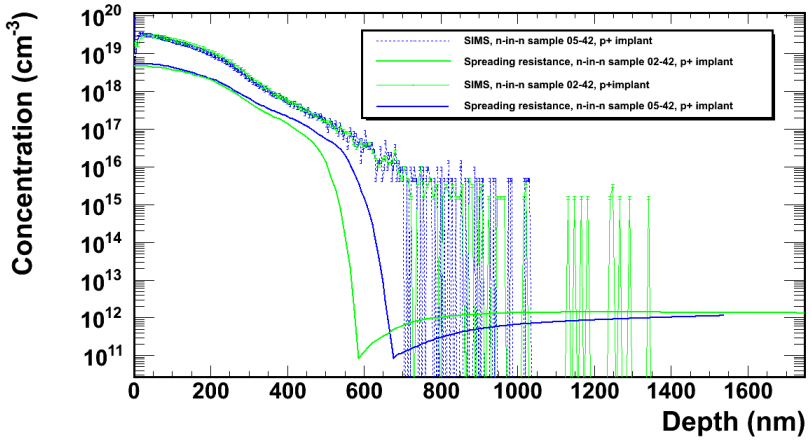

(b) P+ implant

FIGURE 4.4 – N+ and P+ Doping profiles measurement on the n-in-n samples of the PPSU09 production

P-spray and moderated p-spray implantation profiles were also measured on these test structure. The moderated p-spray correspond to a shallow low concentration boron implant while the p-spray correspond to a deeper implant with slightly higher concentration. The difference between both profiles, originationg from the same implantation of boron on the frontside of the wafer is the nitride layer that is used as a filter that is present for the case of low p-spray implant. Figure 4.5a and 4.5b show the two implant profiles measured by the SRP and SIMS method. SIMS measurement are uniform between sample and the

peak concentration of the p-spray implant is shifted with regard to the moderated p-spray implant as expected because of the presence of the additional nitride layer during implantation. SRP measurement, however, show no sign of a junction for all measurements except for the p-spray of sample 02-42. As boron presence is confirmed by SIMS, it is highly probable that the activation step of the p-spray implants was not completed correctly during the processing of the diodes . No p-spray was used in the simulation of the n-in-n sensor although it was implemented as a possible step in the simulation template.

4.1.1.2 n-in-p samples

The same measurements shown in last section were performed on a doping profile test structure and a standard diode of the n-in-p PPSU09 production from the same wafer. Figure 4.6a show the n implant representing the pixel and guard rings implants of the n-in-p pixel sensors. The SIMS profile confirm the presence of a phosphorous layer in the implant and the measurement are compatible with the measurement performed on the diode's n implant. SRP measurement show that activating of the implant was completely correctly. However, no junction is found in the profile. A junction is however found on the backside of the sample as show in figure 4.6b. As the bulk is expected to be p-type, position of the junction is incorrectly located in the device. This lead us to suspect the presence of an additional donor in the bulk of the sensor that inverts the type of the bulk in the manner of radiation damage. It was found that the wafers from were originated these sample was subjected to an oxygenation at high temperature to increase its radiation hardness. The heating of the oxygenated silicon at temperature between 300 and 550 C will lead to the formation of thermal donors [50]. While thermal donor are annealed at higher temperature used for oxidation, if cooling of the wafer back to to room temperature is not done sufficiently fast, formation of thermal donors could have occurred during the transition. These thermal donor can eventually be sufficiently abundant to invert the type of the silicon bulk. Further SRP measurements were performed on the diode structure to determine how deep in the bulk the substrate was inverted. Figure 4.8 show the SRP measurements made on the sample diode on the first 15 microns of the implant. The measurements were performed down to 140 μm under the p and n implants. A junction

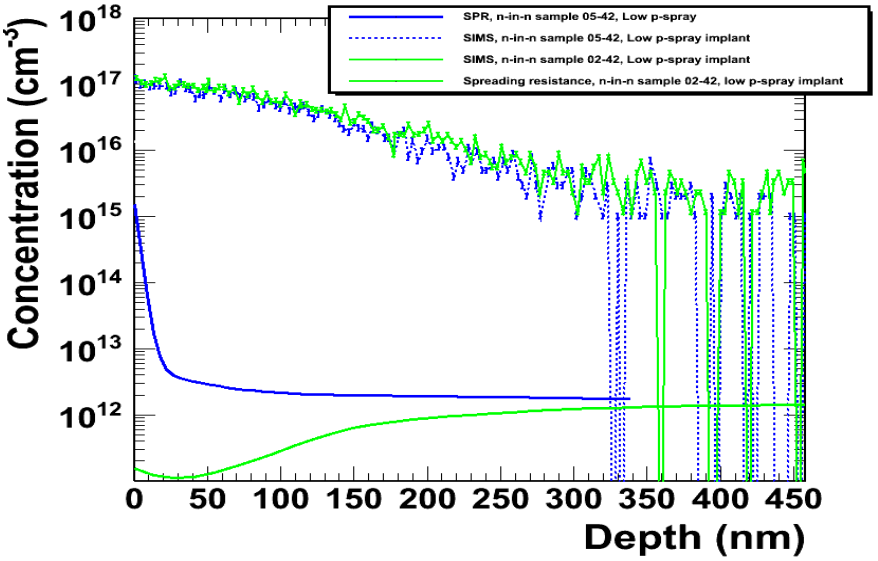

(a) moderated p-spray implant

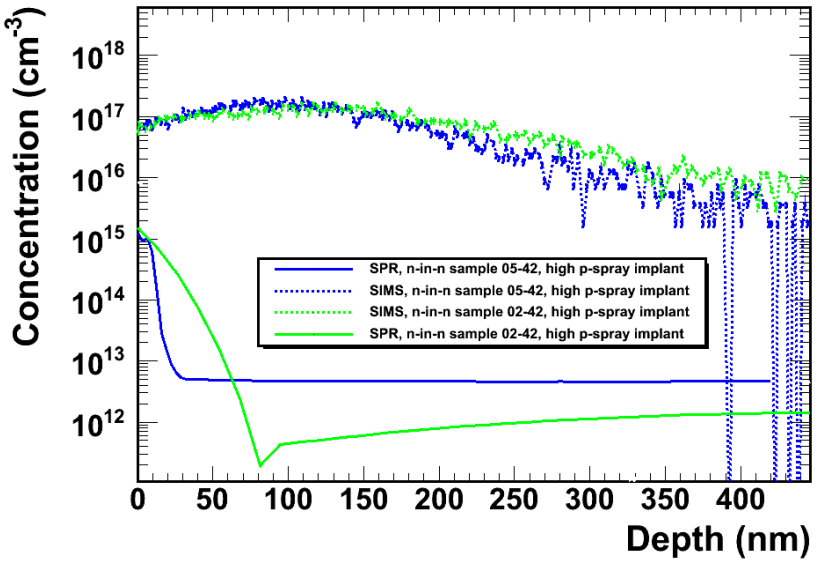

(b) p-spray implant

FIGURE 4.5 – Insulation doping profiles measurement on the n-in-n samples of the PPSU09 production

was found on the backside but in not shown in the figure as stepping was too large. The effective dopant concentration found at the center of the diode was $N_{eff} = 2.6 \times 10^{11} cm^{-3}$, corresponding to a n-type resistivity of 17.6 $k\Omega cm^{-1}$ and a depletion voltage of 18 V considering a 300 μm thick sensor.

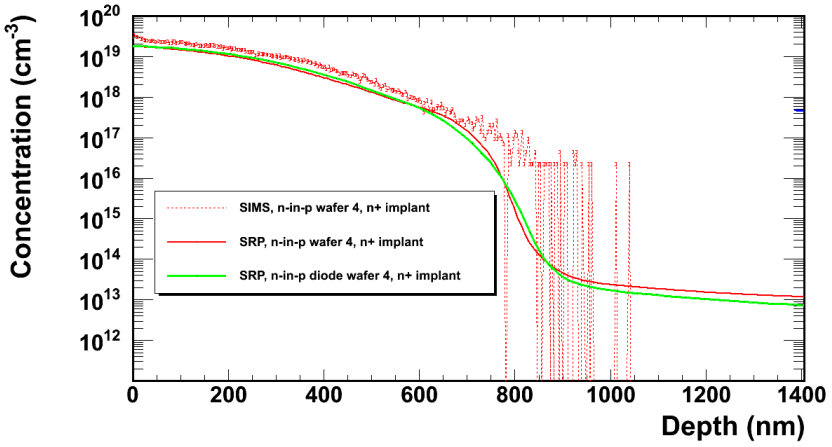

(a) N+ implant

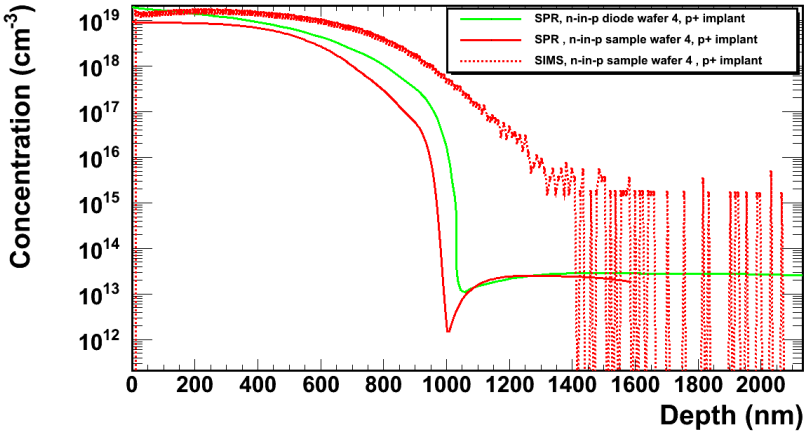

(b) P+ implant

FIGURE 4.6 – N+ and P+ Doping profiles measurement on the n-in-p samples of the PPSU09 production

The p-spray and moderated p-spray implantation are extremely important for the n-in-p sensors as the guard ring structure is located on the electron collection surface. Figure 4.7 show the doping profile measure on the samples for these implants. The SIMS measurement

confirm the presence of boron and the SRP measurement show a well activated profile. The moderated p-spray profile show a shift towards the left with regard to the p-spray profile, as expected. A junction can be found in both SRP profile confirming again the inversion of the bulk type due to thermal donor generation.

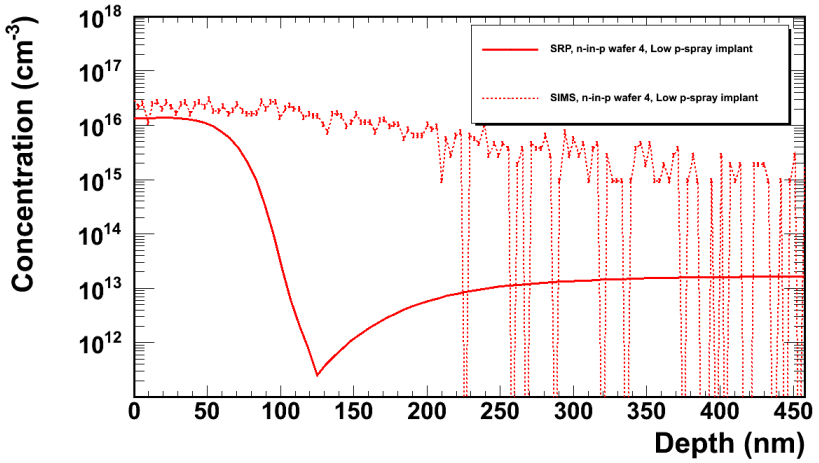

(a) moderated p-spray implant

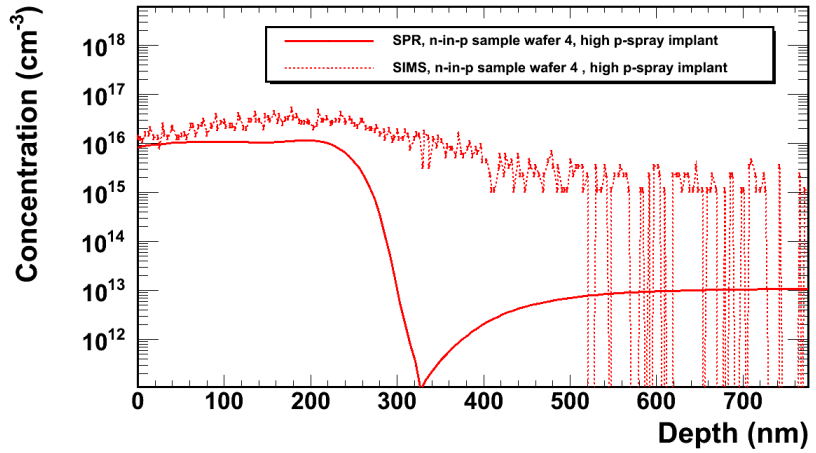

(b) p-spray implant

FIGURE 4.7 – Insulation doping profiles measurement on the n-in-p samples of the PPSU09 production

New sensor production taking into account the results from our measurement were planned to fix the problems encounter in the process. Independent measurements using

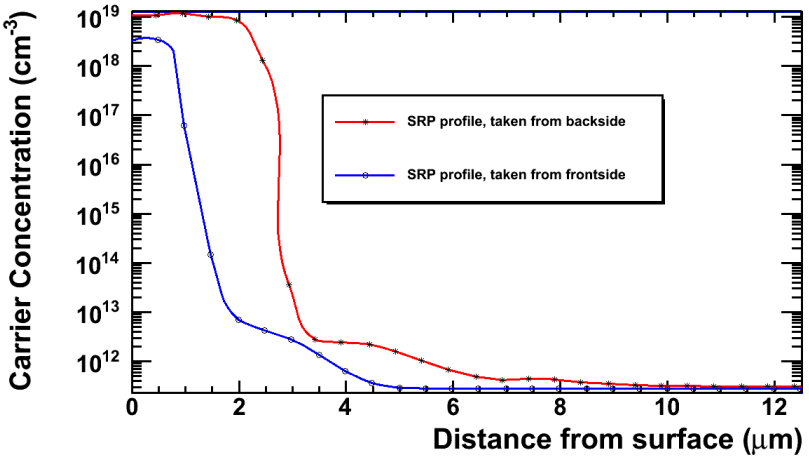

FIGURE 4.8 – SRP measurement performed deep into a n-in-p diode sample

SIMS was performed by LPHNE laboratory and confirm the results presented here. While SIMS and SRP represent efficient methods to characterize the implants of a production, the cost of each measurements limits the quantity that can be performed for each production. in the next section, I present a method that is in development at LAL to perform electrical profile measurement using our own setup.

4.1.1.3 Atomic Force Microscopy Spreading Resistance Profiling

Atomic Force Microscopy (AFM) measure the repulsive and attractive forces between a nanometer scale cantilever and the surface atoms of a sample. Figure 4.9 show the schematics of a typical AFM measurement. The cantilever tip's distance from the surface is measured using the deflection of a laser ray reflecting on its back surface. A very accurate piezoelectric translation system is used to scan sample surface with the cantilever and obtain a measurement of the topology of a surface. This method allow to study nanoscale feature of a surface and allow to perform accurate measurements while scanning on short distances. The Institut d'Electronique Fondamentale (IEF) located on Orsay campus is equipped with an AFM equipped with a resiscope. The resiscope is used to measure the electrical resistance between the tip of the needle and the backside of a sample when a certain bias voltage is applied. This apparatus allows us to scan and measure local resisti-

vity of beveled implant structures by scanning the surface of the bevel and measuring local resistivity. Calibration sample with known resistivity can be used to calibrate the method and translate resistance measurements into carrier concentration profiles.

In order to proceed with the measurement, a bevel of a small known angle had to be etched from the doping profile test structure. IEF own a polishing machine,a MECAPOL P400, that can be used to etch and polish the surface of our sample. A mechanical structure was design by Tristan Vandenberghe, mechanical engineer at LAL, to allow to polish the small silicon test structure. Figure 4.10 show the CAD drawing of the polishing device.

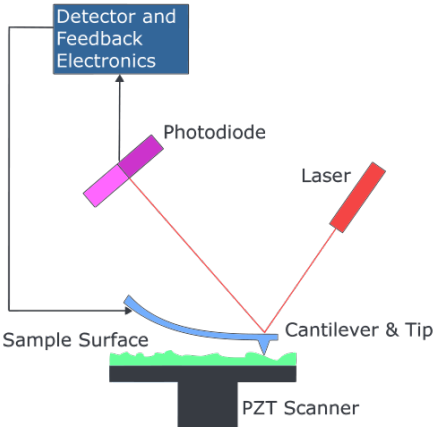

force micro-

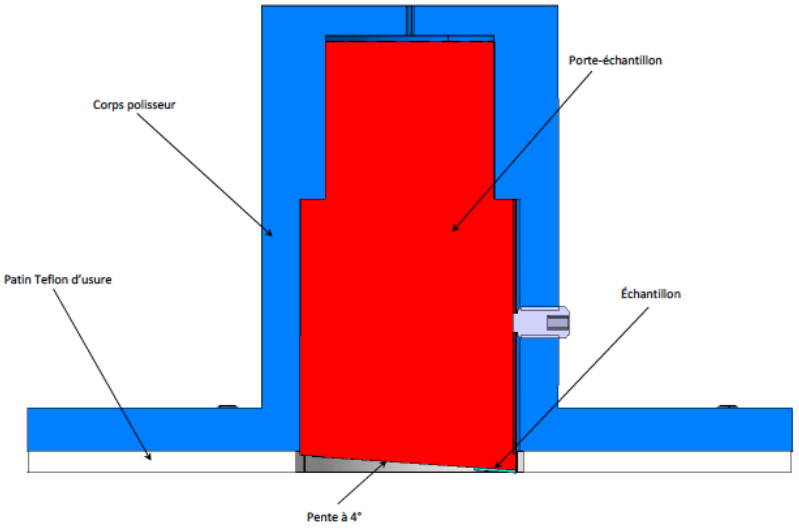

FIGURE 4.10 – Sample holder designed for small angle beveling in doping test structure using the MECAPOL P400 polishing machine.

Figure 4.10 show a bottom view of the device showing the sample holder with a doping profile test structure fixed on the angle surface using double sided conductive tape. The beveling of the surface is performed by first removing the extra

layer of silicon from the sample using a 2400 grain per square inch abrasive paper. The surface of the bevel is then polished using successively small grain polishing liquid with grain size of 9,3 and 1 μm. A final polishing is done using a commercial colloidal silica solution named NALCO. Through the polishing process, the rugosity of the surface has been monitored using a profilometer throughout each step to adjust the step of the polishing protocol to develop a standardized procedure. Optical inspection of the sample has also been performed after each polishment. Figure 4.11 show the evolution of the typical profile of the surface after various step of the process. It can be observed that the variation in height of the surface is reduced after each polishing step. The final state of the surface should exhibit defects of a typical size of 1 μm or less. The final angle of the beveled structure was measured by mechanical profilometry to allow for correct translation from measured distance from bevel edge to doping profile depth.

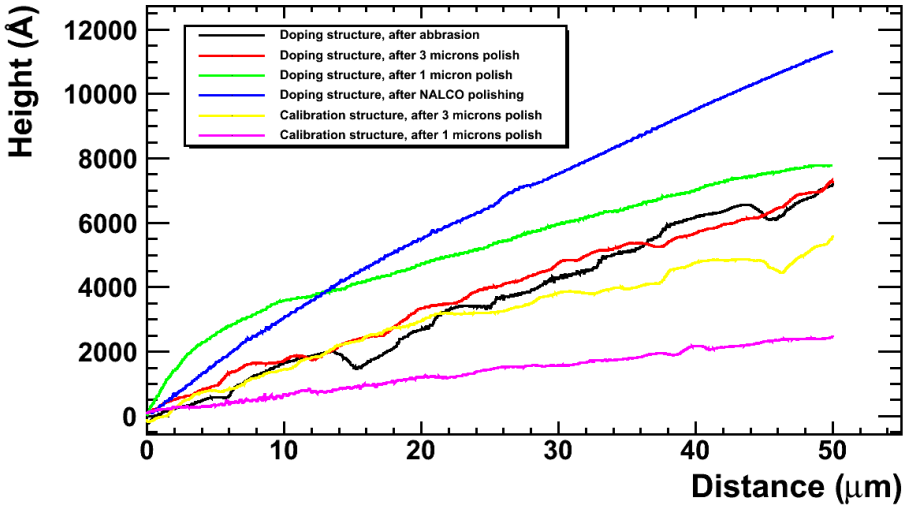

FIGURE 4.11 – Evolution of rugosity of a doping profile test structure after successive polishing steps

At the moment of writing these lines, several problem have been observed in the polishing procedure. The problems range from wrong polishing time to incompatibility of certain substance present at the surface of certain sample, such as the BCB used to insulate the guard rings of the n-in-p sensor, with the polishing liquids. However, preliminary

results obtained on two samples shown the feasibility of the method and its ability to measure small implant structure. Raw results of measurements performed on the n-in-p test structure are shown in figure 4.12. The results show the resistance of the surface as a function of the position of the scanning cantilever. The resistance is expressed in terms of the raw output of the resiscope in V, ranging from 0 to 10 V corresponding to a resistance range of 10^2 to 10^{12} Ω. Calibration sample will be measured to obtain an absolute value of the carrier concentration. Knowing the bevel angle, measured with mechanical profilometry, we can obtain the actual doping profile of the implant by multiplying the x distance by the sinus of the bevel angle. The relative depth of the implant is in agreement with the previously measured value for this structure.

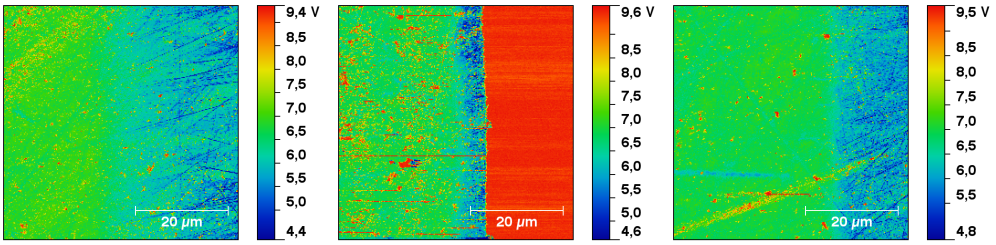

(a) n+ implant (b) moderated p-spray implant (c) p-spray implant

FIGURE 4.12 – Raw image of the resiscope signal for a scan of a 50x50 μm surface. Right side of the figure represent the surface of the structure.

Figure 4.13 show the converted doping profile of the n implant of figure 4.12, averaged in the X direction. The calibration between resistance and concentration values was done using preliminary measurements done on calibration sample with fixed carrier concentration. The very good agreement between the preliminary results obtained and the other doping profile measurement gives us confidence in the reliability of the method and further step will be taken to standardize the method to obtain reproducible results.

Another advantage of the AFM method is that it allows us to get two dimensional image of the implants if the implant lateral dimension can be constrained within the scanning window of the AFM, usually 50 x 50 μm. Trials have been performed to measure the p+ implant of the ATLAS n-in-n guard ring structure. A FE-I3 sensor was cut to expose the guard ring structure. The surface of the guard rings was beveled to expose the implants

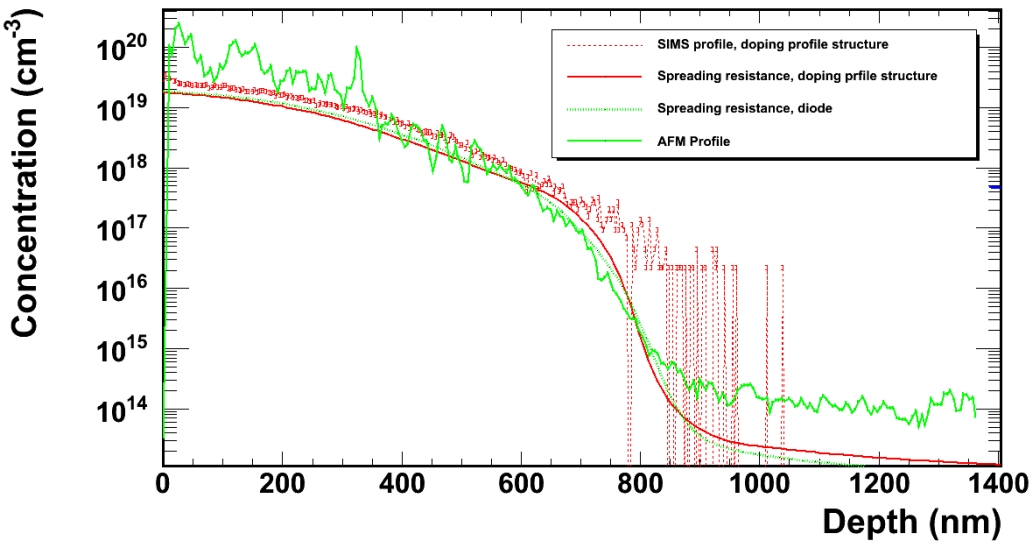

FIGURE 4.13 – Comparison between the doping profile of the n implant of the n-in-p production with the SRP and SIMS measurements performed on the sample

and an AFM measurement was performed on the sample. Figure 4.14 show the converted profile obtained on the sample. The surface of the sample, covered by oxide and nitride, can be seen in the lower part of the plot where resiscope output values are very high. This high resistance is due to the bad contact between the cantilever and the oxide. Two complete guard ring implants of a 10 μm width can be seen, as expected for this structure. The depth of the implants is compatible with the measured depth for the n-in-p production. Further work is needed to obtain more accurate and less noisy measurement. However, the preliminary results obtained and presented here have demonstrated the feasibility of the method. No other doping profile measurement methods allow for two dimensional profiling of the implants. This method makes it a very interesting candidate for comparison with TCAD simulation model of implantation required to create the structure used in electrical simulation.

4.1.1.4 Calibration of TCAD implantation model with experimental data

With the data of the PPSU09 doping profile structures, we were able to determine some of the main missing parameters needed for accurate simulation of the implantation in

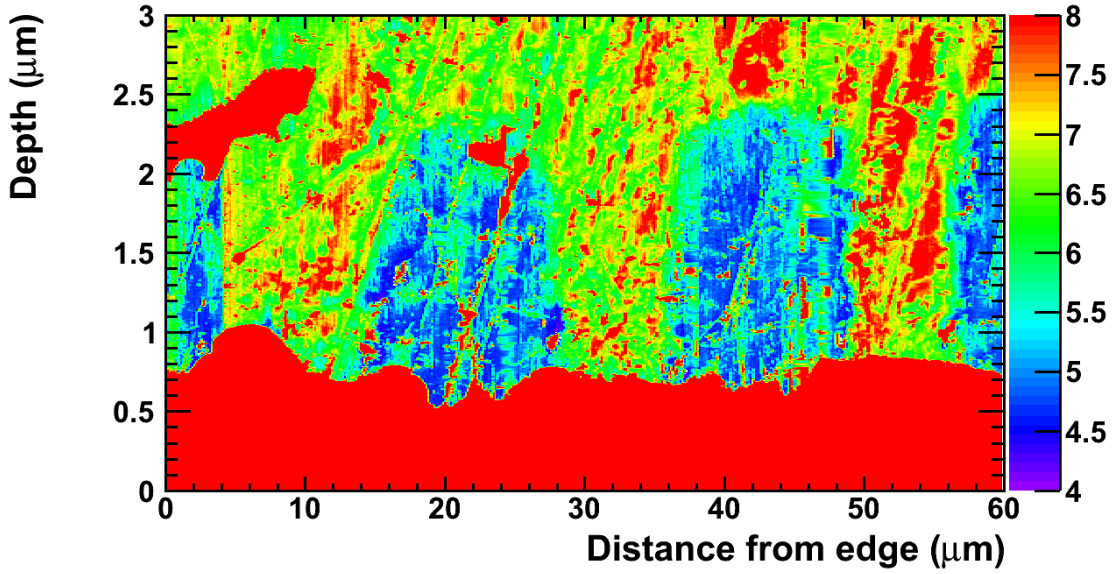

(a) SPR Raw measurement

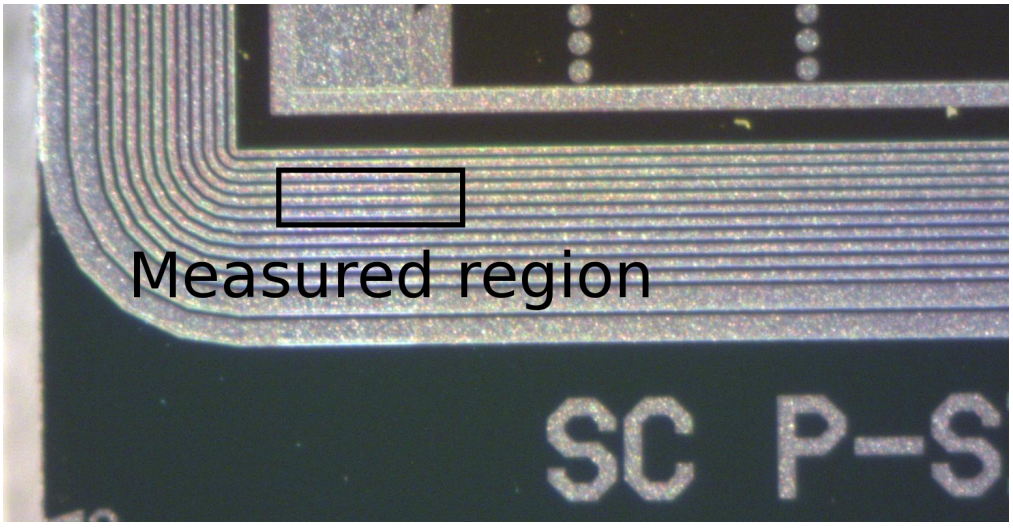

(b) Photography of the measured region

FIGURE 4.14 – 2D doping profile of an n-in-n ATLAS standard guard ring structure

TCAD process simulation. As p-spray and moderated p-spray were shown to have problems in the production, the experimental profile were used directly in the simulation to avoid the complex problem of finding the process step leading to such profile. Same method was done for simulation of the n-in-p sensor's n and p implant. The presence of thermal donor affect the doping profile and makes it very hard to disentangle the different process step leading to such profile .

Apart from the lack of activation of the p-spray for some sample, the n-in-n sample have shown the expected doping profile characteristics. The parameters needed to reproduce the implantation process of these implants are the temperature and duration of the thermal annealing used to activate the dopants, the thickness of the oxide layer used a screen and the energy and dose of the implanted ions. The Modified Levenberg-Marquart algorithm [39], built-in SILVACO software, was used to obtain the value of these parameters that produce a simulation of the doping profile that most closely fits the experimental SIMS and SRP measurements.

Two models are available in SILVACO TCAD software to simulate the diffusion of the dopants : The fermi diffusion model and the fully coupled diffusion model . The fully coupled model includes the physics of the previous model and adds a new phenomenon needed for more precise simulation of small details of the doping profile. The physics behind each of the model is described in the TCAD software manual [39]. Two implantation models are also available. A simple model which consist of a parametrization of implant profiles using various SIMS measurements can be used for fast simulation. A Monte-Carlo model using the binary collision approximation, can be used to obtain a more accurate description of the implant. However, the computing time needed increases by an order of magnitude when using the more accurate model. This limits the usability of the two last models for large structure simulation.

Optimization of the implantation parameters was performed using the simple diffusion and implantation models. The advanced models were then activated to compare the obtained profile to the SIMS measurements. figure 4.15 show the comparison between the doping profile obtained and the SIMS profile for the n-in-n p and n implants. It can be observed that the simulated profile reproduce well the shape of the experimental data. As

more complex model are used, even more accurate description of the profile is obtained. Parameters used to produce these profiles are shown in table 4.3. These parameters we used for the n-in-n sensor simulation shown in the last chapter. Experimental profiles were directly injected in the simulation in the case of the p-spray implants. Simulation of the n-in-p structure were also performed using the experimental data when available.

TABLE 4.3 – Optimized doping and diffusion parameters for the n-in-n PPSU09 production

Parameter	N+ implant	P+ implant
Oxide thickness (nm)	40	40
Implantation dose (cm^{-3})	1.38e15	5.5e14
Implantation energy (keV)	10	10
Annealing temperature (C)	1350	1293
Annealing duration (min)	0.22	0.15

4.1.2 Guard Ring measurements

The guard ring structure of the planar pixel sensor of the PPSU09 production have been simulated to predict their behavior under bias. The main measurable parameter is the bias voltage taken by the guard ring when the sensor is biased. In the clean room, a setup using a probe station enclosed in a copper faraday cage, connected to a Keithley 6517B high voltage source and an electrometer was used to measure the potential distribution of various guard ring structures. An electrometer with a high input impedance (10^{20} Ω) was used to ensure that the measurement of the guard ring voltage does not influence the sensor and modify the results. As guard rings are floating structure unconnected to any bias source, using a standard voltmeter with lower impedance would draw current from the guard ring modifying its electrical potential . N-in-p sensor were simulated using an n-bulk as it has been observed in the last section that the bulk type has been inverted by thermal donors.

The first measurements were performed on the three guard ring structure presented in figure 3.9. Figure 4.16 show the simulated and measured guard ring potential for the three guard ring models. The results obtained are in good agreement with the experimental data, giving us confidence that the TCAD simulation model correctly represent the physical be-

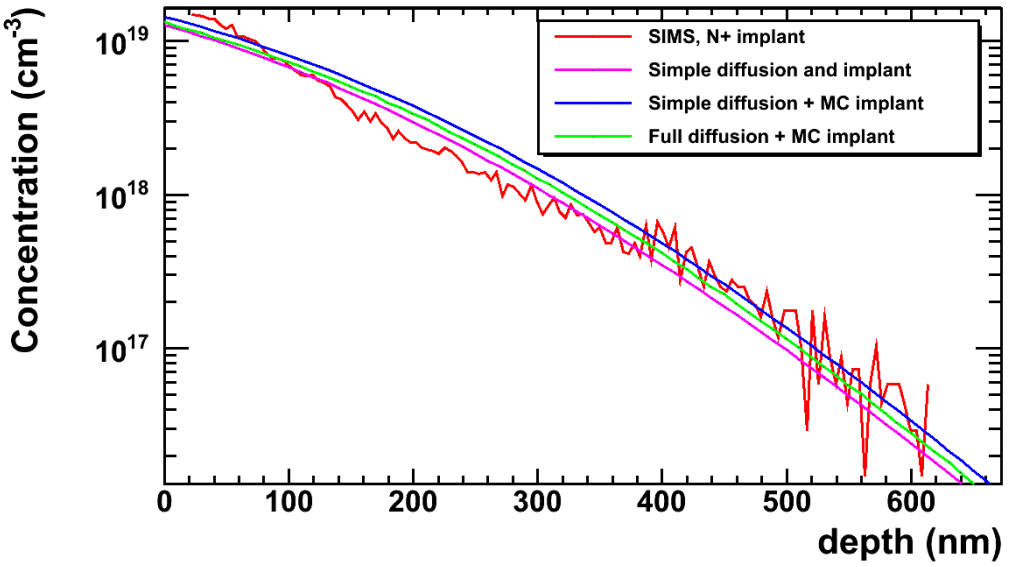

(a) N implant

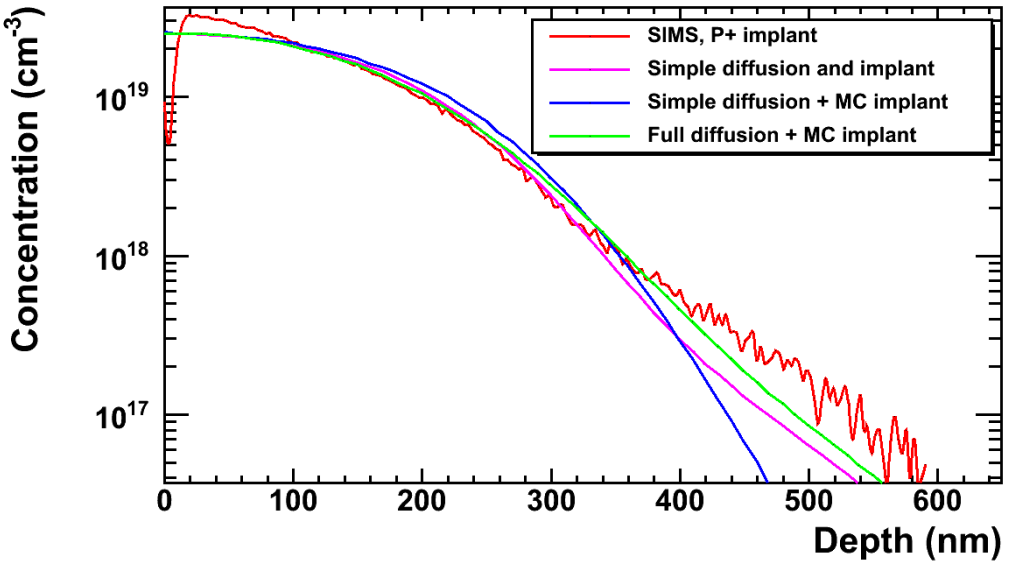

(b) P implant

FIGURE 4.15 – Comparison of simulated and measured n and p doping profile of the PPSU09 production after optimization of implantation and diffusion parameters

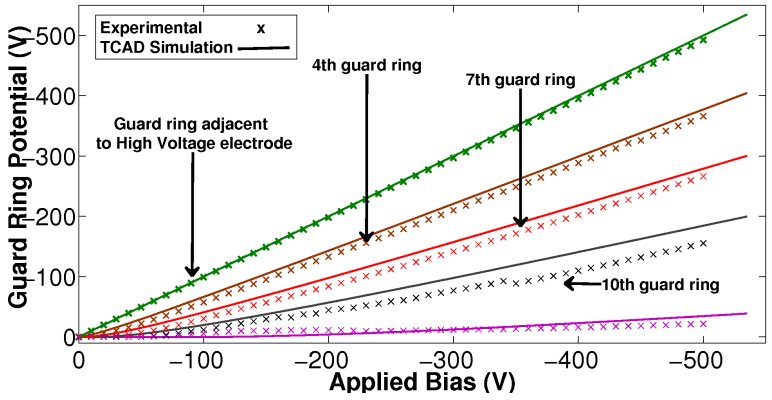

(a) ATLAS standard structure

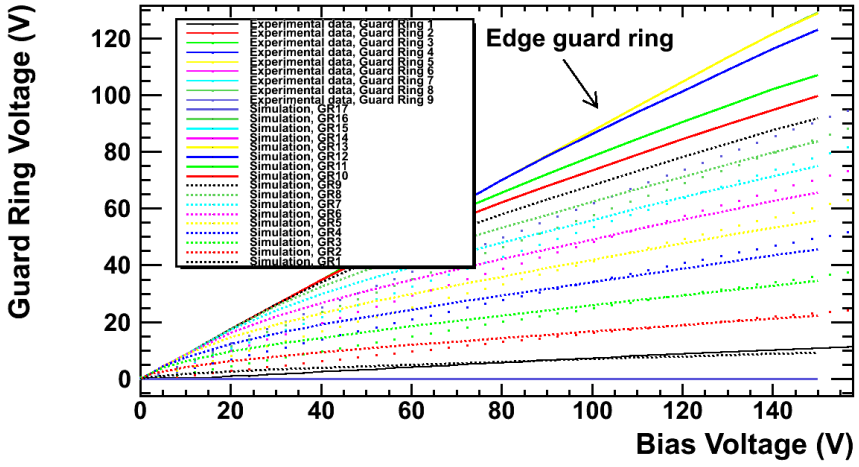

(b) Small guard ring structure

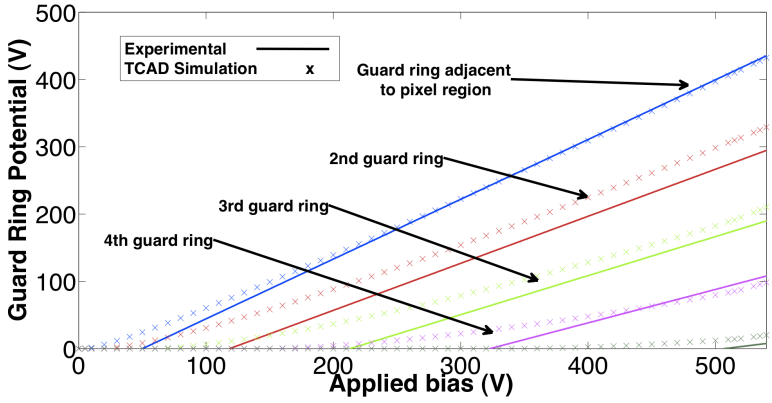

(c) Large guard ring structure

FIGURE 4.16 – Comparison of simulated and measured guard ring potential of the PPSU09 production guard ring structure after optimization of implantation and diffusion parameters

havior of multi-guard ring structures. Some discrepancies that could not be easily explained can be seen in the outer guard rings of the small guard ring n-in-p structure. The measurement of these guard rings have shown poor reproducibility hinting at some transient phenomenon. A possible explanation could be an oscillation of the guard rings around the edge potential due to some unknown effect that wasn't reproduced in simulation. The use of the experimental doping profile data has been very important to obtain correct results. It has been observed that the guard ring's bias potential obtained in simulation was very dependent on the doping profile characteristics of the n, p and p-spray implants. The use of the profile measurement allowed us to reduce the number of free parameters needed for the simulation and resulted in the correct guard ring behavior.

The size of the guard rings of the three model studied here doesn't allow easy measurements. Contact with the guard ring has to be done by etching mechanically the passivation layer over the guard ring structure using the probe station needle, which can eventually reduce the performance of the sensor. A limited number of full guard ring structure were measured to keep its integrity for future use for irradiation or beam test studies. As mentioned in the first section of this chapter, a set of test diodes with large contactable guard rings was placed in both the PPSU09 n-in-n and n-in-p production. The number of guard ring on the diode span from 1 to 4, the same guard ring size for each structure. For example, the 4 guard ring model contained the 3 guard rings of the 3 guard ring diode plus a fourth one added on the outer edge of the structure. The implant of the guard ring structure are 60 μm wide, with the electrode width being respectively, from the inner to outer guard ring, 120, 150,180 and 210 μm. The electrode overshoot the implant toward the outer edge of the diode by 18 μm and the distance between each ring is 10 μm. Measurement of the guard ring potential of the structure was done for the diodes of the PPSU09 n and p bulk production. Measurements within each production have shown a variation of less than 10 % between the measured guard ring potential for the diodes coming from different wafer. A good reproducibility has been observed as the same structure have led to the same results when measured two months after the first measurements. Two set of four diodes n-in-n diodes have been irradiated at CERN with 24 GeV protons to $1 \times 10^{15} n_{eq} cm^{-1}$ and $4 \times 10^{15} n_{eq} cm^{-1}$. A set of n-in-p diode was also irradiated to a fluence of $2 \times 10^{15} n_{eq} cm^{-1}$.

The sample were kept under 0 C after irradiation during transport and were kept at -28C during storage to avoid annealing effects.

A TCAD simulation of the four diodes was performed for each type of bulk, before and after irradiation. Figure 4.17 show the comparison of the simulated and measured guard ring potential for four diodes of the n-in-p production. The removal of the outer guard rings made no change to the guard ring potential of the inner guard rings and only results of the 4 guard ring simulation are shown in this figure. This is analog to the simulation of the removal of the ATLAS standard guard ring structure similar to what described in chapter 3. In both case, the removal of the outer guard ring have only minor influence on the potential taken by the other guard rings. Simulation reproduce well the guard ring potential curves at lower bias voltage but fails at higher voltage. However, the general behavior of the guard ring structure is well reproduced by the simulation. Other guard ring measurements results have shown better agreement with simulation The discrepancy between simulation and measurements could be induced by a physical phenomenon not included in the simulation or systematic effect in the measurements when measuring large guard ring as it is the case here.

The n-in-n diode simulation have shown the same results as for the n-in-p diode simulation. The guard ring behavior seems to be independent of the substrate type. The guard ring structure have been measured on the n-in-p and n-in-n irradiated diodes. Figure 4.18 show the measured potential on 2 of the diodes irradiated to a dose of less than $2 \times 10^{15} n_{eq} cm^{-1}]$. The guard ring seems, in both cases , to completely stop working. In the case of the n-in-n structure, this was predicted to happen after irradiation. For the n-in-p structure, the simulation predicts working guard rings. However, it was discovered that increasing the surface charge up to a value of $2 \times 10^{12} cm^2$ produce the observed effect. In the simulation, the guard ring stay shorted to ground potential for any bias voltage. The variation seen in the experimental data are not reproduced in details but the very low value and the uniformity of the potential on the guard rings show that they are not functional any more and the value measured is probably the result of a systematic effect present in the measurement setup.

The p-spray insulation used and measured in the n-in-p production might not be suffi-

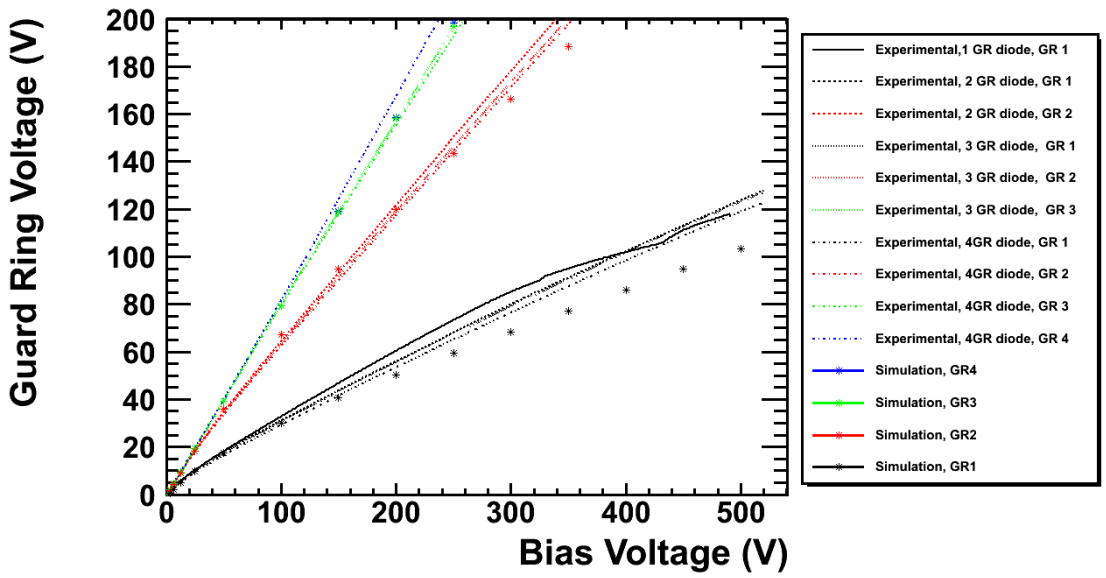

FIGURE 4.17 – Comparison of measurement and TCAD simulation of the potential of the LAL diode test structure for the n-in-p production

cient to ensure proper insulation of the guard rings after irradiation with charged particles. Neutron irradiation of these diode structure should be performed to evaluate the decouple the measurement and pinpoint the different effect affecting the guard ring. P-spray simulation seems to overestimate the insulation power of the implant and further work is needed.

4.1.3 Current versus Bias characteristics

An important parameter of pixel sensor are its leakage current and breakdown voltage. Simulation of leakage current represent a difficult task as all simulation are performed in two dimension, on sub-volume of the actual detector. Breakdown voltage prediction can however be done from simulation and compared with experimental results. Leakage current was measured in the various FE-I3 and FE-I4 structure of the n-in-n and n-in-p production. Figure 4.19 show the results of these measurements for the FE-I3 sensors. The n-in-p production contained two types of sensor using respectively the p-spray and the moderated p-spray insulation method. It can be clearly observed that p-spray sensors have lower

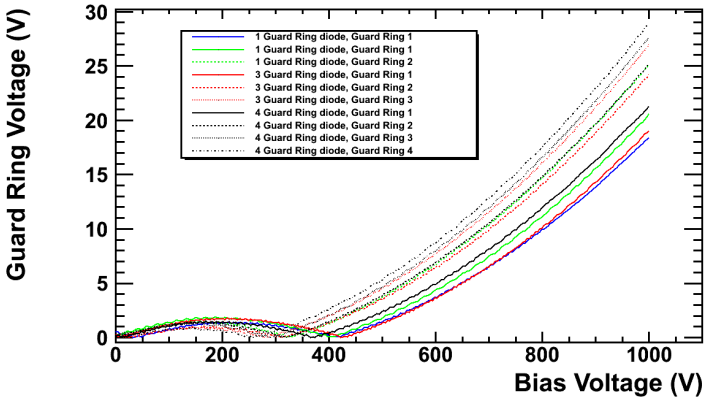

(a) n-in-n,1 $\times 10^{15} n_{eq} cm^{-1}$

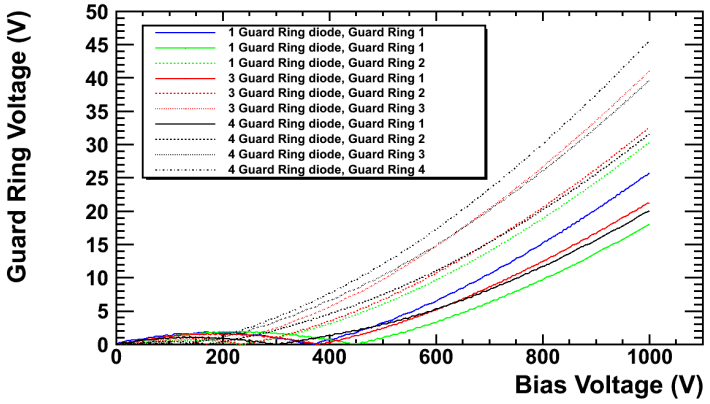

(b) n-in-p,2 $\times 10^{15} n_{eq} cm^{-1}$

FIGURE 4.18 – Measured guard ring potential for LAL diodes after irradiation

breakdown voltage, between 200 and 250V, as the p-spray implants surrounding the n implants generate high electric field region where high leakage current can be generated. The breakdown observed in these sensor is not a steep brutal one but rather a slow exponentially raising leakage current. The moderated p-spray sensors show breakdown around 400 V. In moderated p-spray, the p implant surrounding the n implants is less deep than the p-spray implant and this has for effect of reducing the electric field and leakage current in these regions. Simulation predict a much higher breakdown voltage for these sensors, around 1000V. It is however known that other sensor of the same production show higher breakdown voltage. The wafer used for these measurement was discarded and considered as a bad wafer in view of its lower breakdown voltages. The wafer is however useful for sensor characterization and irradiation studies. FE-I4 sensors with p-spray and moderated p-spray were also present on this wafer and leakage current measurement are shown in figure 4.20. Again in this case the moderated model show better breakdown voltage but statistics was too low to draw any conclusion.

The guard ring diode were also extensively measured before and after irradiation. At the moment of writing these line, no cooled probe station chuck were available to perform measurements on the irradiated diodes at a lower temperature to limit leakage current. The results shown here are of limited interest but still show the increase of leakage current with exposed fluence. Figure 4.21 show the IV characteristics of the diodes that were available for measurements. An interesting behavior can be observed in the case of the n-in-p diodes. The leakage current curves shown here for these sensors were taken successively on the same diode during overnight runs. The breakdown voltage observed in the curves for the n-in-p diodes drifted during the night getting higher until it settles to a stable higher value. It can be interpreted as a reorganization of the surface charge within the oxide layer due to the added presence of an electric field. Local hotspot breakdown due to locally accumulated charge are diluted as the charge drift in the field present in the oxide, revealing the real breakdown value of the diode. The big variation in breakdown from a diode to another, does not allow to draw conclusion on the relation between the number of guard ring and the breakdown voltage of the diodes. The n-in-n diode measurement show the only measurement available for n-in-n diode at the moment of writing these line. Most

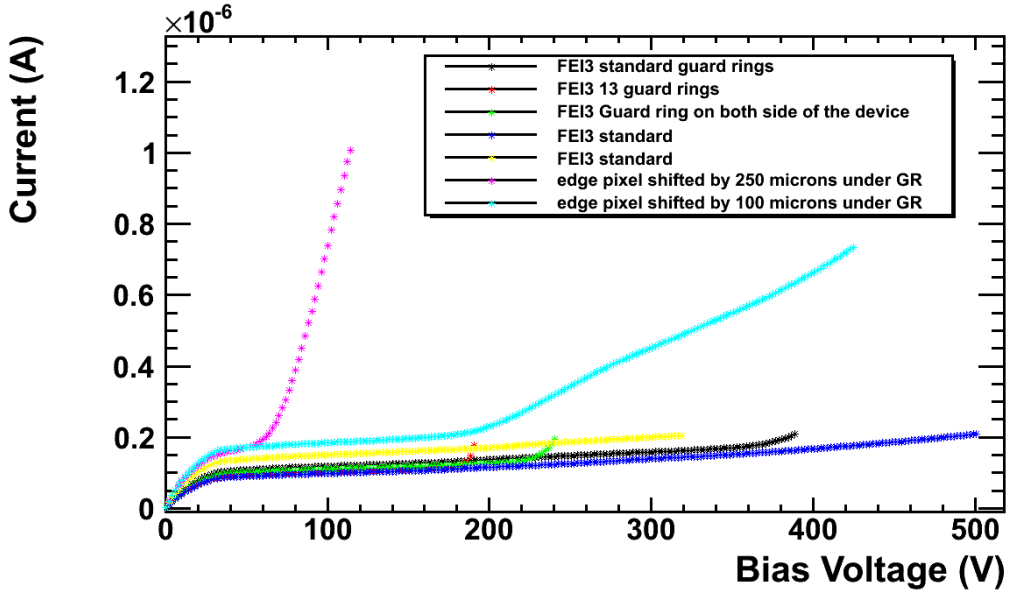

(a) n-in-n production

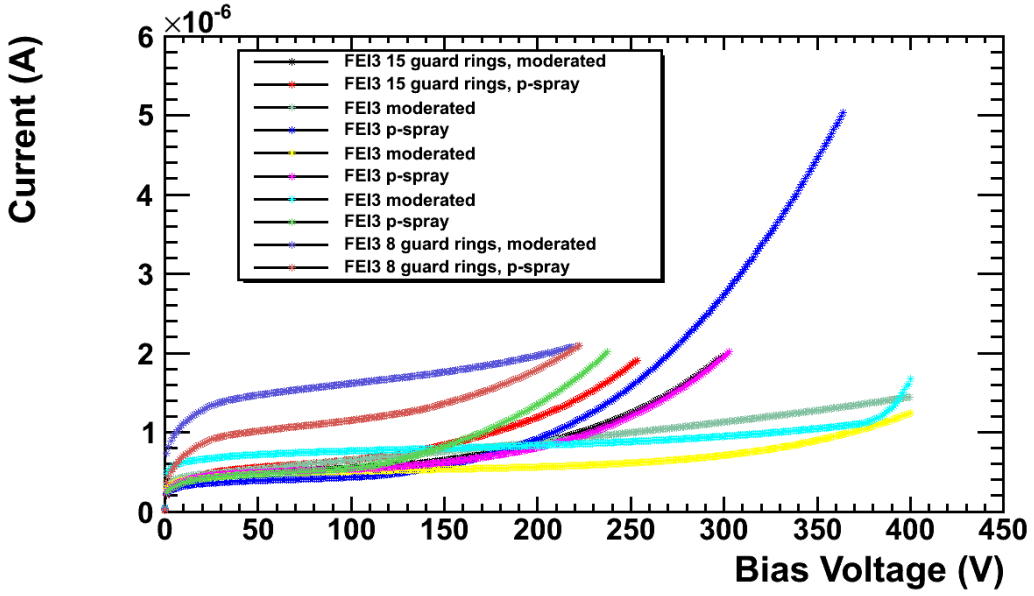

(b) n-in-p production

FIGURE 4.19 – Leakage current in the FEI3 of the PPSU09 production

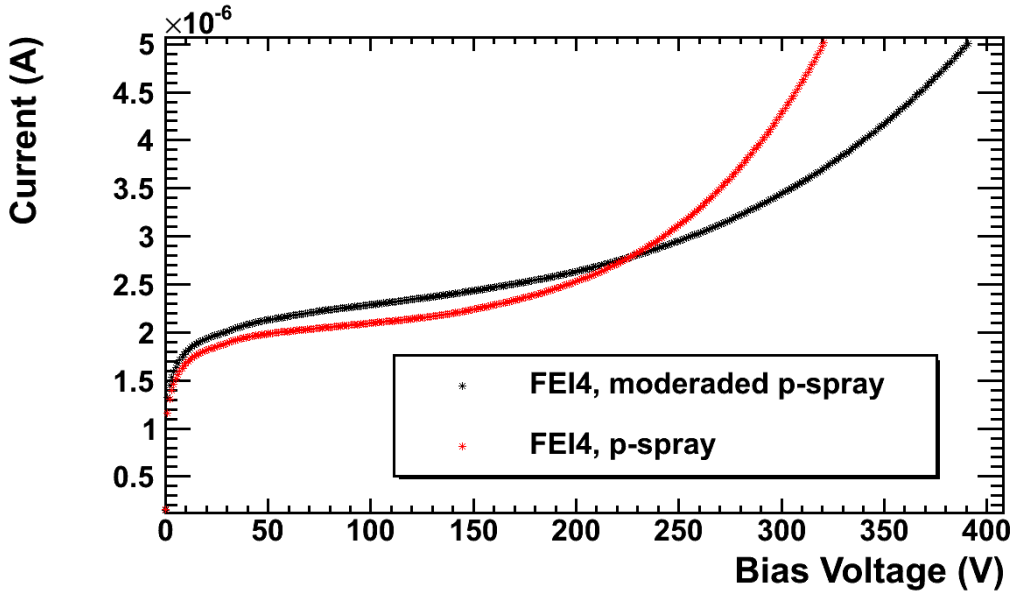

FIGURE 4.20 – n-in-p small guard rings FE-I4 leakage current

diode of the production were sent to irradiation for a short time period.

Figure 4.22 show the leakage current measured in the diode after irradiation. As measurement were taken at room temperature, very high leakage current value can be observed. Measurement were performed very quickly to avoid the heating of the diode that was also promptly put back to its cold storage. No apparent breakdown can be observed in any of the diode. A slow rise of current, also observed in the current-voltage curve simulated in chapter 3. The breakdown present before irradiation are quenched by the presence of the high amount of defects trapping the charge before it can multiply and create a cascade leaking to breakdown. Leakage value for the different diodes irradiated at the same fluence is uniform showing that leakage current after irradiation is dominated by bulk defect generation recombination current and not surface quality and edge effects as usually seen before irradiation.

Experimental measurements presented in this section were used to better understand the behavior of the sensors and interpretation of the simulation results can be used to gain understanding of the experimental data. Guard ring potential are well reproduced

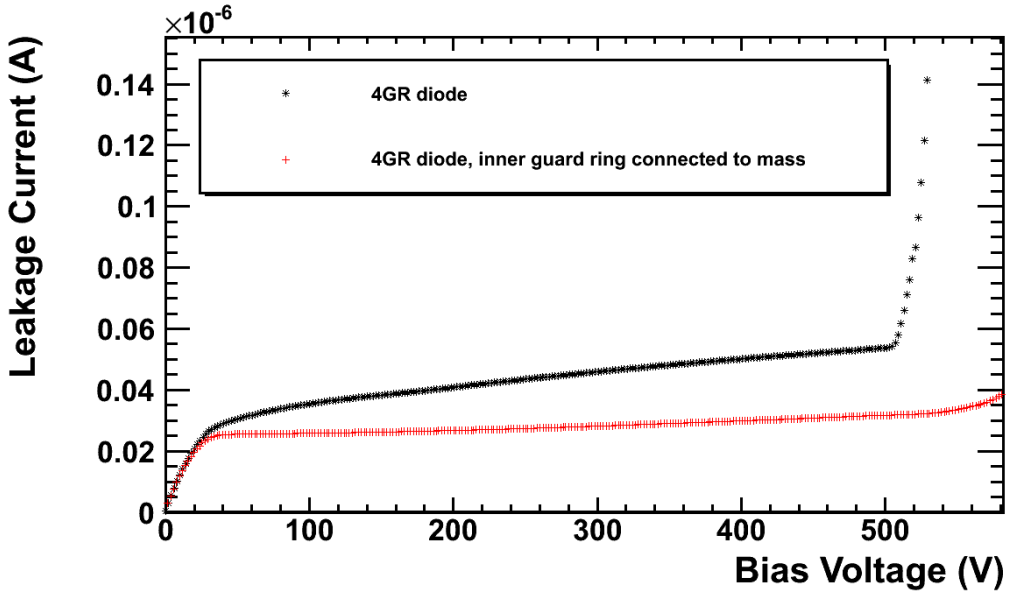

(a) n-in-n production

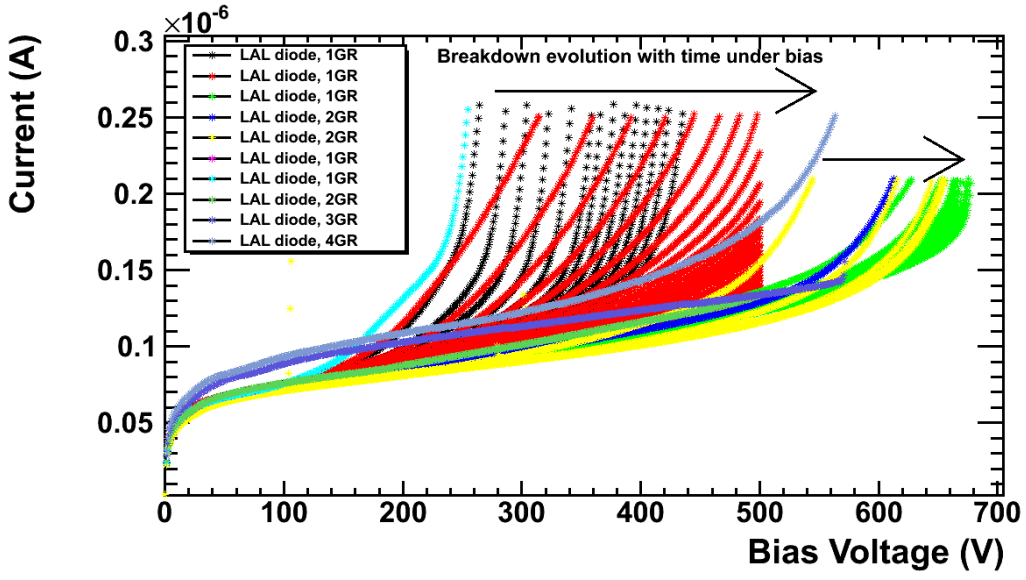

(b) n-in-p production

FIGURE 4.21 – Leakage current in the guard ring diodes of the PPSU09 production

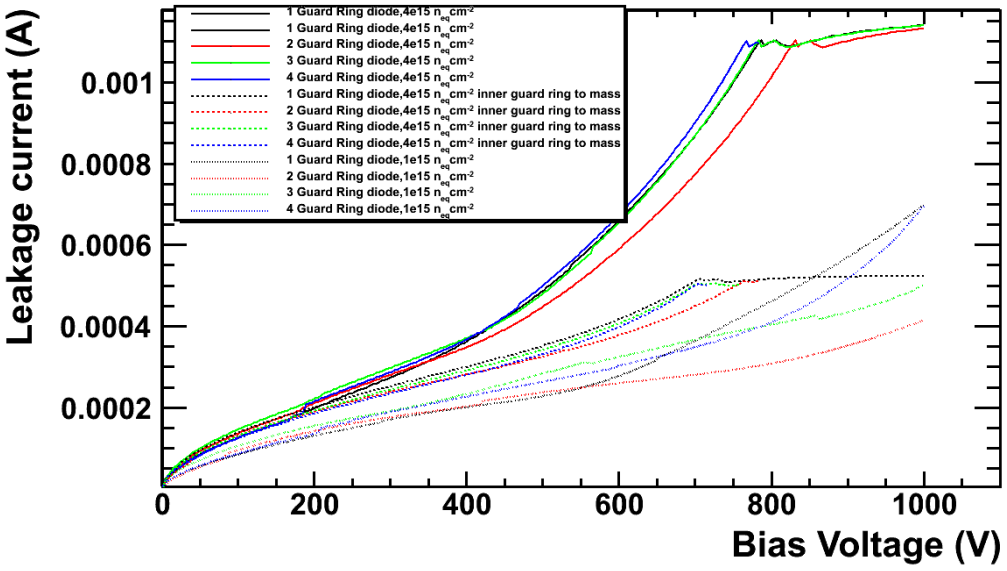

(a) n-in-n production

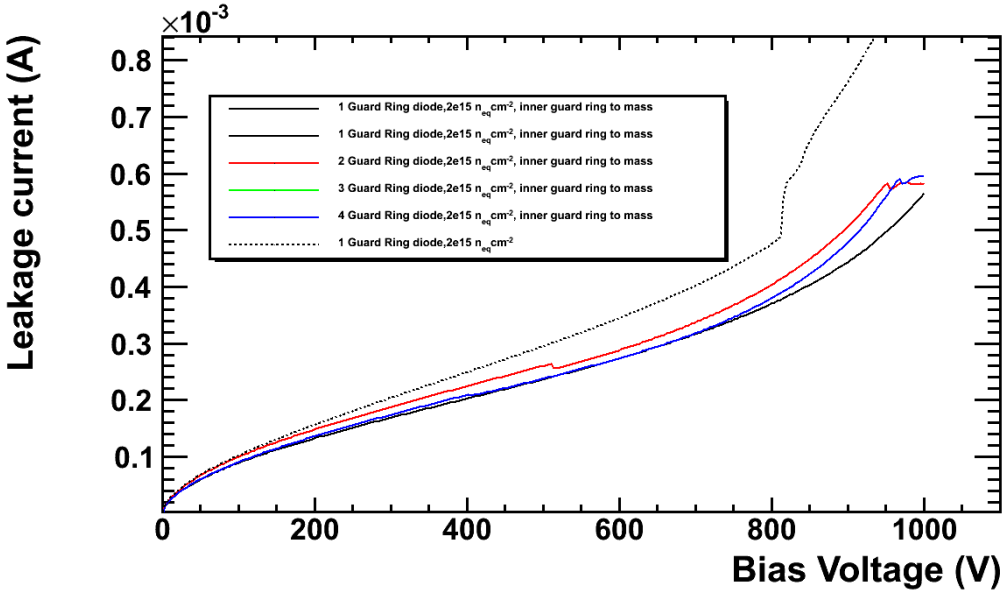

(b) n-in-p production

FIGURE 4.22 – Leakage current in the guard ring diodes of the PPSU09 production after irradiation

by simulation, both before and after irradiation, in the case studied here, and lead us to be confident in the results coming from TCAD simulation. The use of experimental doping profile allow easy plug-and-play reproduction of the guard ring structure behavior. The model presented in this work can be used for optimization of guard ring structure for future sensor such as the super LHC pixel detector. Leakage current and breakdown voltage remain hard to predict but the soft breakdown observed in radiation damage simulation is also observed in irradiated devices.The breakdown voltage value predicted by the simulation seems to be higher than the one observed in reality. The qualitative tendency can however be used to gain insight on the effect of modifications to the design of multi-guard ring structure.

Chapitre 5

Planar Pixel Sensor digitization for ATLAS IBL simulation

The ATLAS IBL pixel sensor will be subject to extensive radiation damage that will affect its performance in terms of reconstruction of the charged particles trajectory and impulsion. Charge collection efficiency will be reduced by trapping and high electric field will be present in the bulk of the sensor. Space charge inversion will eventually occur and sensor will futher need to be operated underdepleted as bias voltage sufficient for full depletion will not be reachable by the power supply of the detector system. To produce accurate simulation of the full detector system and evaluate reconstruction performances, we need an accurate and fast model of the charge collection to digitize the energy deposition information coming from the GEANT4 simulation of the detector. Our group has developed a digitizer based on our knowledge of TCAD and Monte-Carlo simulation of pixel detectors.

A simulation framework , the ALLPix software, was developed. It provides an easy test-bench for digitizer using the GEANT4 [51] simulation package. The software can be used to simulate any pixel sensor geometry along with its surrounding environment. A realistic model of the EUDET pixel telescope [52], shown in figure 5.1, was used in the test beam period of November 2009, july and november 2010 at CERN SPS (120 GeV pions) and in May 2010 at DESY (1-4 GeV electrons). It provides a simulation tool of the telescope that is useful for debugging and understanding the behavior of the telescope. Various digitization model can be used to convert the GEANT4 hits of the device under test into detector hit information. The simulation can be used to generate virtual telescope

data that can be reconstructed using the telescope reconstruction software. The comparison between the real test beam data and simulated one will be used to validate the digitizer package developed at LAL. Once validated. this digitizer can then be transferred to the ATLAS simulation software to perform full detector simulation.

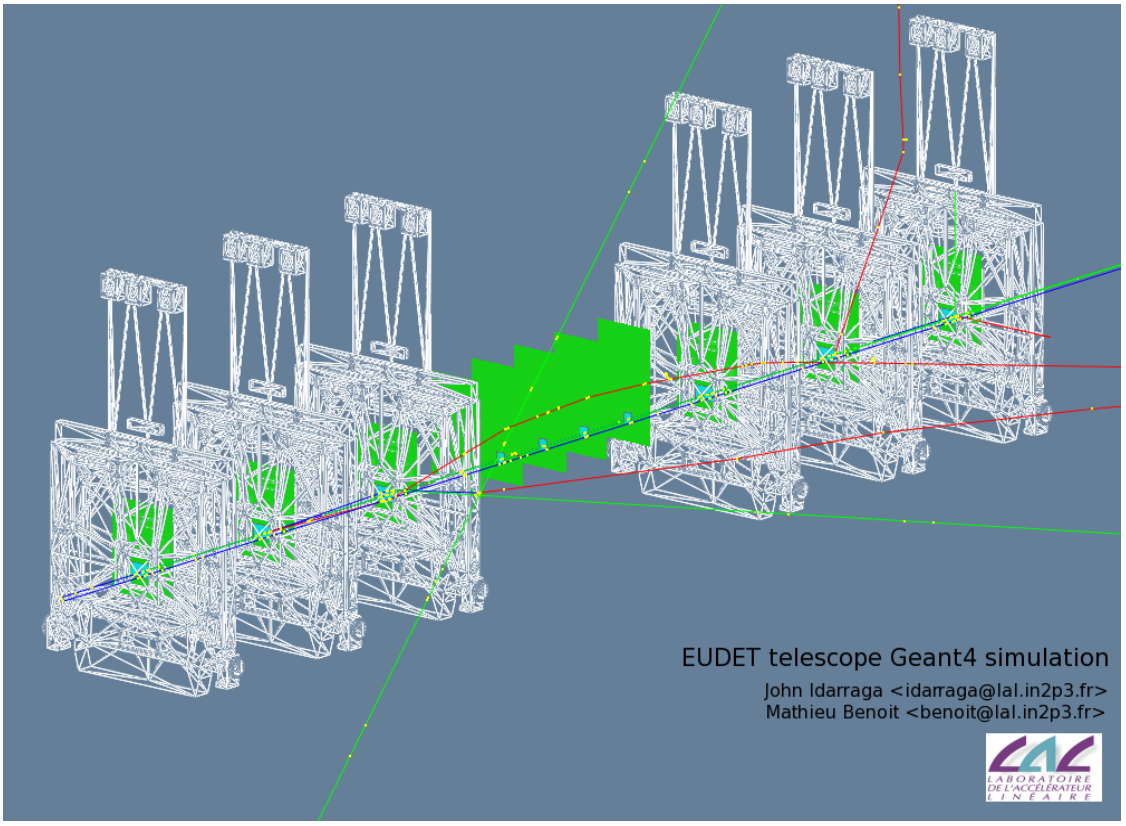

FIGURE 5.1 – EUDET telescope geometry implemented in the ALLPix framework. Wire frame box represent the 6 telescope planes and the green volumes in the middle are the DUT PCB card

The LAL digitization model presented here aims to provide a simple digitization tool for the FE-I3 and FE-I4 planar pixel sensor featuring the slim edges guard ring structures proposed for the IBL pixel detector. The radiation damage model used to compute the trapping time and resistivity of the bulk after exposure to radiation is the Hamburg model presented in chapter 2.

To simulate charge transport in the bulk of the pixel sensor, we first take the trajectory of the particle crossing the sensitive volume and divide it into a smaller fraction of charge

deposition hits. The energy deposition of each hit is translated in a number of electron hole pair and variation of this number following the Poisson statistics and the Fano factor is taken into account. The number of these hit can be set as a free parameter to allow more or less accurate representation of the charge deposition along the track. The punctual charge element are then transported in the electric following the drift-diffusion equation. Effects such as saturation velocity are taken into account to accurately compute the drift time of the punctual charge element. Electric field can be provided through a TCAD simulation result of evaluated using an analytical function. The integration of the trajectory is done using a fifth order integration method called Runge-Kutta-Fehlberg method [53]. For most simulation purpose, the drift inside unidimensional electric field should be sufficient to reproduce well the experimental data. A schematic of the digitization charge transport model can be seen in figure 5.2, where the drift cone of the charge element are shown spreading from the track position along the drift trajectory.

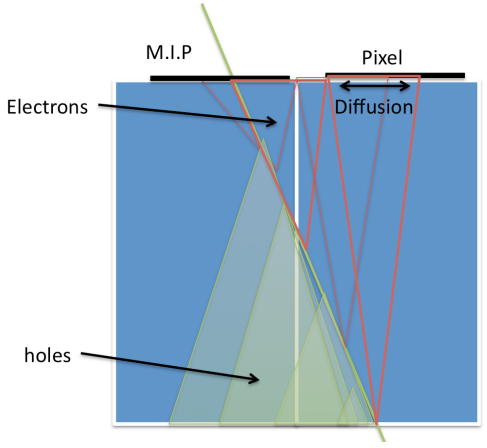

FIGURE 5.2 – Schematic of the digitization model

A lifetime is also computed for each charge element hole and electrons using the trapping lifetime computed with the Hamburg model. The charge element trapping position in the sensor is determined using the drift trajectory and velocity of each charge element. Using the initial and final position of the charge element, we can use Ramo theorem (equation

The lateral diffusion associated to each charge element is also computed using the drift time of the charge element and the classical solution of the diffusion equation for a

gaussian distribution. Equation 5.1 describe the evolution of the standard deviation of the distribution with time in silicon. D is the diffusion coefficient.

$$\sigma_{x,y,z}(t) = \sqrt{2D_{e,h}t} \tag{5.1}$$

The resulting gaussian distribution of charge is then projected on the pixel plane, and charge inside the element is divided between the pixels using equation 5.2

$$Q_i = \int_{x_0 i}^{x_f i} \int_{y_0 i}^{y_f i} \rho(x,y) dx dy \tag{5.2}$$

where Q_i is the charge collected by electrode i, bounded by the rectangle extending from $x_0 i$ to $X_f i$ and $y_0 i$ to $y_f i$ and $\rho(x,y)$ the projected gaussian distribution of the charge element on the pixel surface. Finally, the threshold of the readout chip threshold is simulated by eliminating pixel hit under a constant threshold that is a free parameter of the model. This model was implemented in a digitizer for the allpix framework. Results and comparison with test beam data will be shown in the next section.

5.1 Test beam validation of TCAD simulation and digitization

The EUDET telescope has been used to study the tracking performances of the different flavor of ATLAS pixel sensor from the PPSU production. The telescope is composed of 6 planes of MIMOSA26 MAPS sensor with a pitch of 18.5 μm arranged in a matrix of 1156x1156 pixels. The telescope is divided in two arms located each side of the ATLAS pixel detector assemblies. Particles crossing the entire telescope were selected using 4 scintillator triggers in coincidence two by two on each end of the telescope assembly. Data taken by the ATLAS pixel assemblies are recorded for the 16 next level 1 trigger count. The EUDET software is then used to reconstruct the trajectories of the recorded particles. The tracks are extrapolated to the device under test and used to analyze the behavior of the ATLAS pixel sensor. Track positioning resolution between the telescope arms is 3 μm.

5.1.1 Validation of the digitization model

I will present here a validation of the digitizer using the reconstructed data from CERN planar pixel October 2010 test beam period. The devices under test that were evaluated were , in increasing order distance from the beam : a 11 guard ring ATLAS n-in-n sensor from the PPSU09 production, a n-in-n stepwise shifted pixel structure and a n-in-p unir-radiated standard small guard ring pixel detector also from the PPSU09. A fourth sensor from Hammamatsu was present in the beam but it not considered in this analysis. The data contained 6.89 million events taken from run 20275 to 20358. Bias voltage were maintained at 150 V through the run and sensor were operated at room temperature. A simulation of 500 000 trigger event were accumulated using the telescope geometry to compare with the data from the pixel sensor under test.

Simulation was performed for a 250 μm thick 5000 $k\Omega cm^{-1}$ sensor biased at 150 V. Electric field was considered from a TCAD simulation of a single pixel cell for a cutline taken at its middle through the depth of the model. The diffusion coefficient for electrons was 40.2 cm^2/s and mobility was computed using the field dependent model shown in chapter 2.

Figure 5.3 and 5.4 show the unbiased residual of the track position reconstructed with the telescope with respect to the reconstructed hit position in the devices under test. Three methods of hit position reconstruction are used and compared in the test beam data reconstruction. The digital and analog method consist respectively of computing the center of gravity of the hit pixel that are regrouped in a cluster and calculating the charge-weighted center of gravity of the cluster's pixel. The simulation data were reconstructed in the same manner and figure **??** and **??** show the residual distribution between the Monte-Carlo truth particle hit position and the reconstructed position from digitization data.

Cluster size distribution of the device under test can be seen in figure 5.6 along with the simulated data. The simulation reproduce well within 3.5% the size distribution of clusters in test beam data for all three sensors. The Time-Over-Threshold (TOT) distribution in the pixel X direction can be seen in figure **??** for the three devices tested and for the simulation of the devices along with the results from simulation.

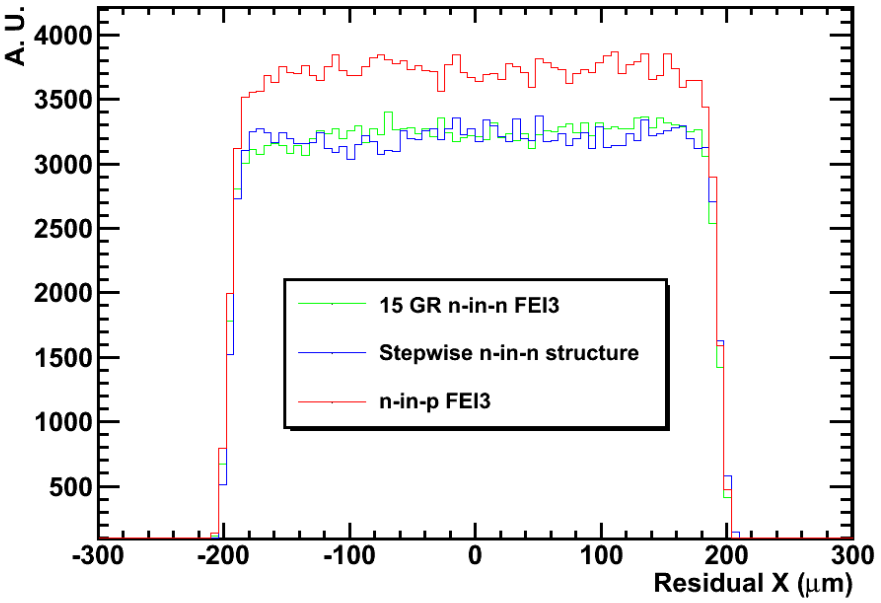

(a) X direction (400 μm pitch)

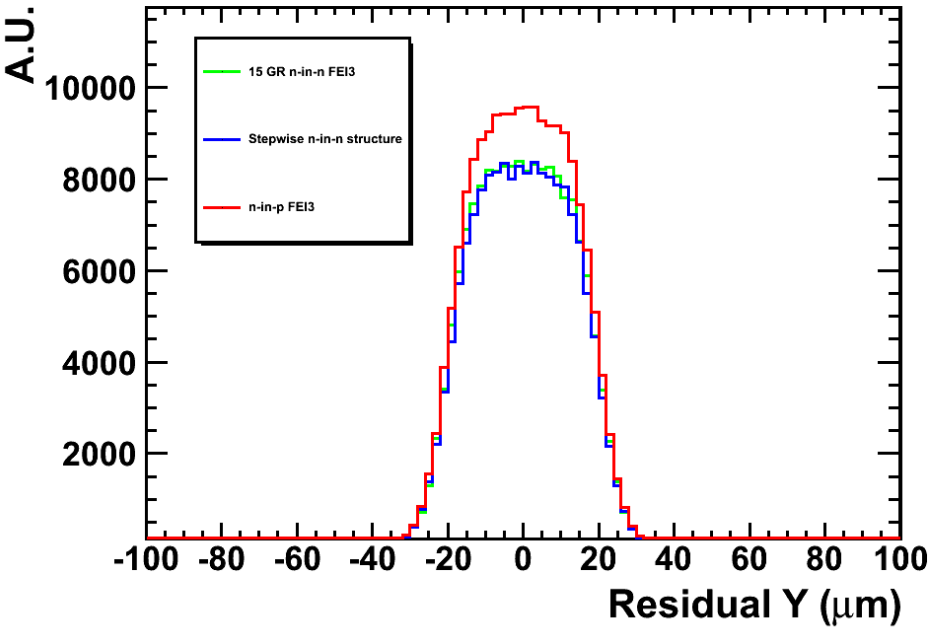

(b) Y direction (50 μm pitch)

FIGURE 5.3 – Experimental unbiased residual distribution for the planar sensors between the arms of the telescope, for cluster size 1

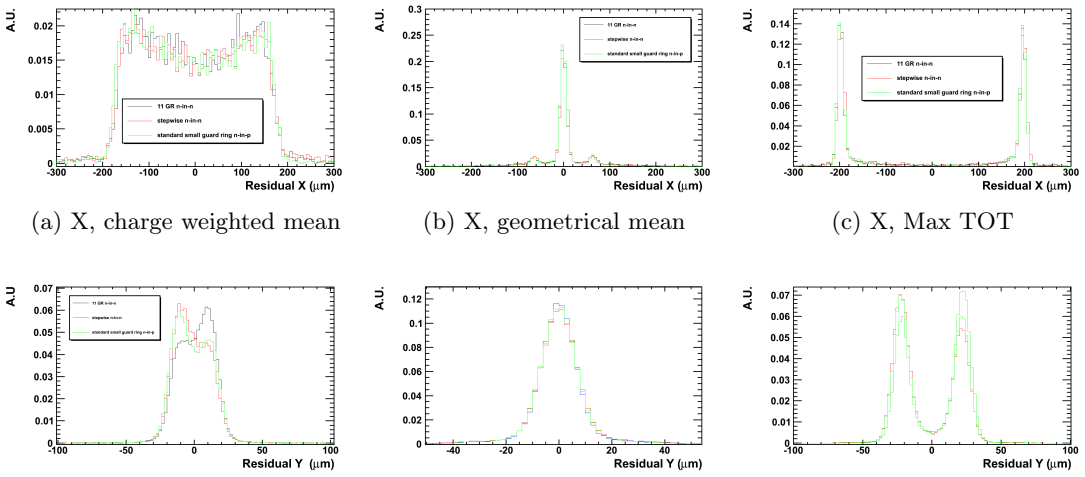

(a) X, charge weighted mean (b) X, geometrical mean (c) X, Max TOT

(d) Y, charge weighted mean (e) Y, geometrical mean (f) Y, Max TOT

FIGURE 5.4 – Experimental unbiased residual distribution for the planar sensors between the arms of the telescope, for cluster size 2

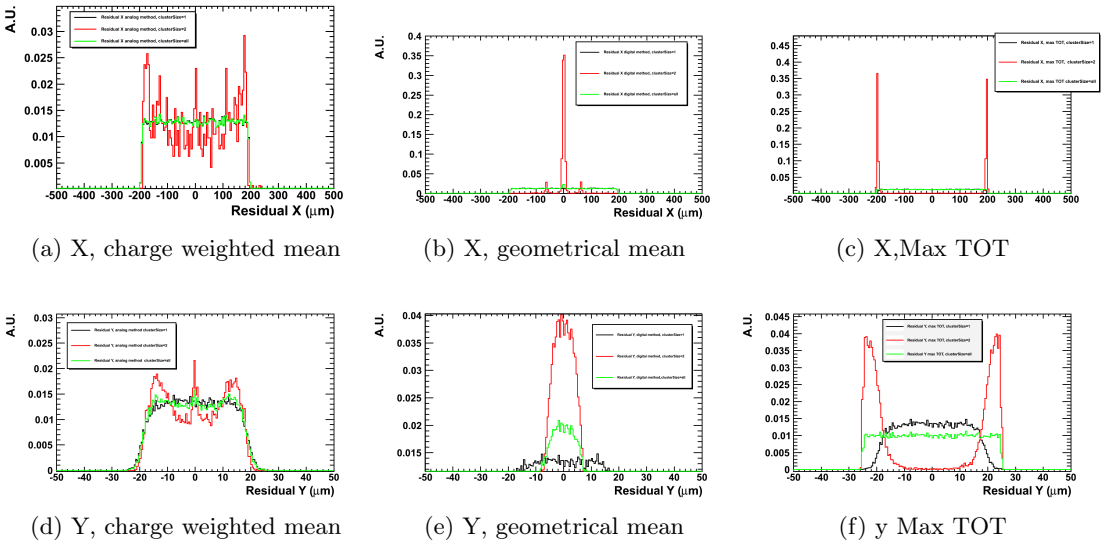

(a) X, charge weighted mean (b) X, geometrical mean (c) X,Max TOT

(d) Y, charge weighted mean (e) Y, geometrical mean (f) y Max TOT

FIGURE 5.5 – Simulated unbiased residual distribution for the planar sensors between the arms of the telescope

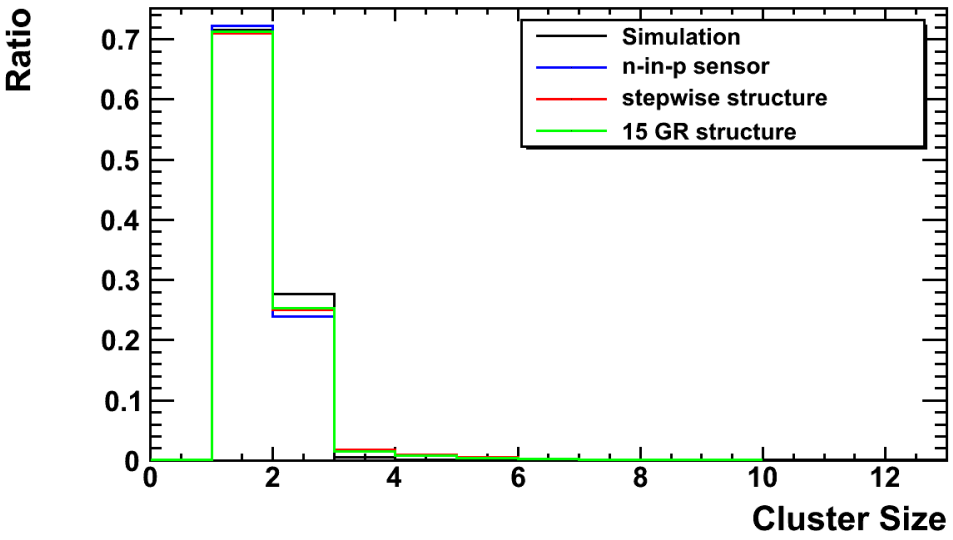

FIGURE 5.6 – Cluster size distribution in experimental Pion test beam data compared to digitization

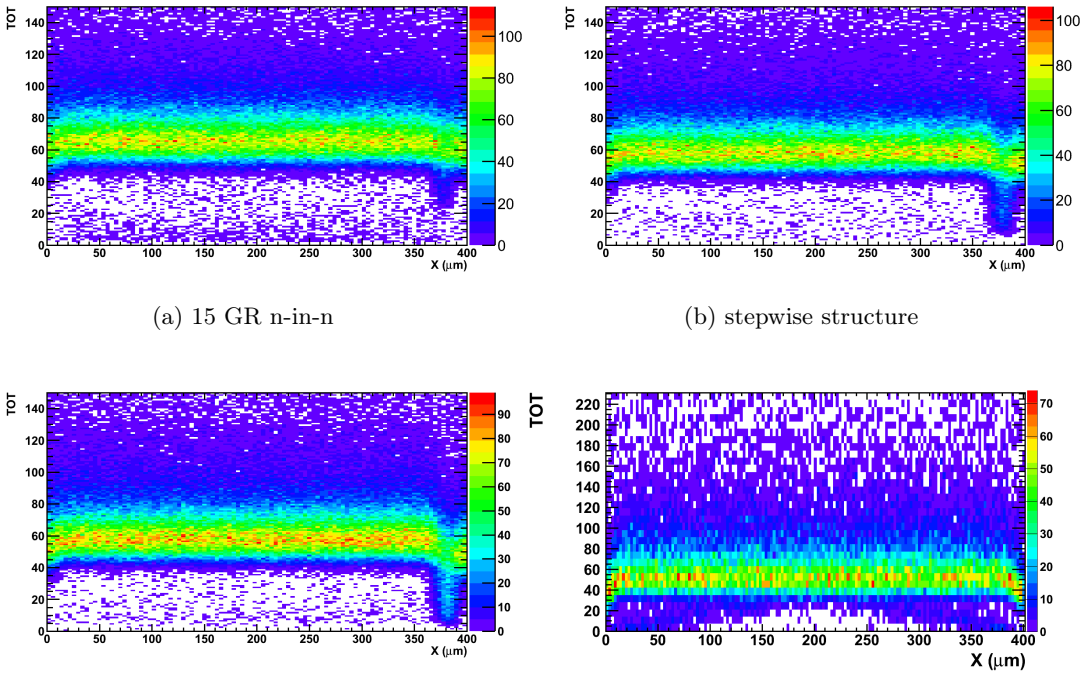

(a) 15 GR n-in-n

(b) stepwise structure

(c) n-in-p small guard rings

(d) Simulation

FIGURE 5.7 – TOT Profile in the X pixel direction, average of all pixels

The simulation results are in good agreement with the results obtained with the three device in test beam. The Charge profile along the X direction are different for the experimental dara compared to simulated data because of the punch-trough structure, seen in figure 5.8, which is used to bias the pixel and collect charges so that it does not reach the readout chip. This mechanism is not included in the simulation. The TOT average value from simulation is also lower than in the experimental data because the sensor was simulated with a thinner bulk. The calibration of the virtual chip was kept to obtain a value of 60 for a deposited charge of 22000 electrons.

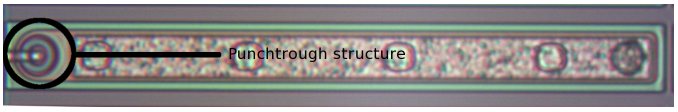

FIGURE 5.8 – FE-I3 standard pixel with its punch-trough bias structure

5.1.2 Edge effects

The stepwise ATLAS pixel structure has been designed to study the edge effects of the slim edge structure and verify the predictions of the TCAD simulation of the structure. Figure 5.9 show the geometry of edge pixel that was used in the production. Edge pixels are shifted by groups of 8 by steps of 25 microns under the guard ring structure. The efficiency and charge collection averaged over each set of 8 pixels can be seen in figure 5.10.

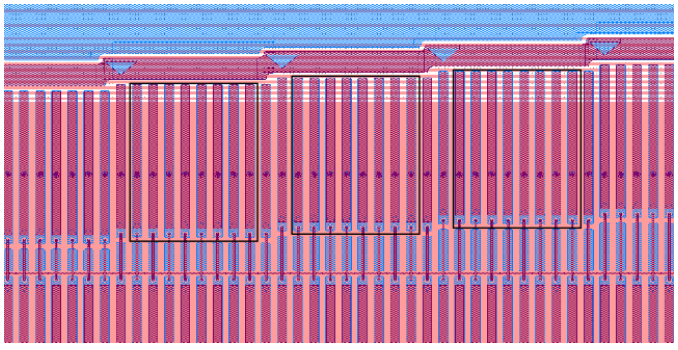

FIGURE 5.9 – GDS drawing of the stepwise pixel structure

The charge collected under the guard rings is reduced with respect to the charge collected within the guard ring structure. This effect was predicted from TCAD simulation and

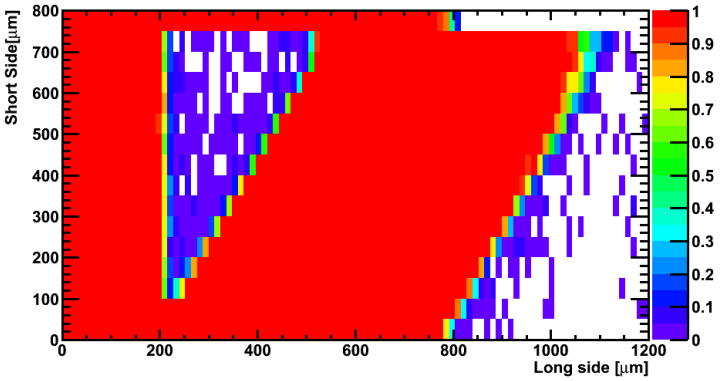

(a) Detection efficiency at the edge of the sensor

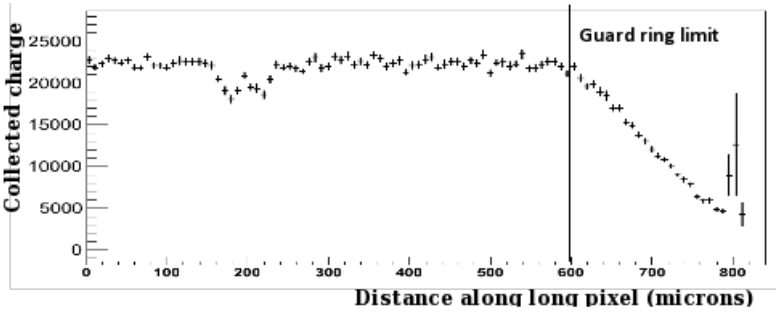

(b) Charge collection profile along a pixel shifted by 200

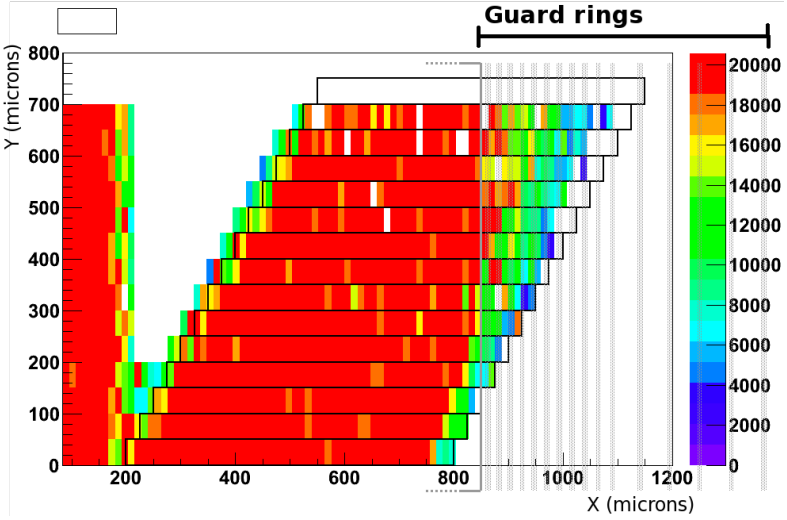

(c) Charge collection profile along the shifted pixels

FIGURE 5.10 – Experimental measurement of the charge collection and detection efficiency of the slim edge guard ring structure

demonstrated in test beam situation . The detection efficiency is maintained as signal is large enough to trigger the readout electronics. Post-irradiation behavior, with guard rings loosing their usefulness and SCSI occurring, the difference in charge collection in the active zone and under the guard ring should be minimal. These data can be used to parametrize the charge collection at the edge pixels in the digitizer to simulate the slim edge structure.

Overall , the digitization model reproduce well the behavior of ATLAS FE-I3 unirradiated and irradiated sensor tested at CERN using the EUDET telescope. This model can be scaled to simulate FE-I4 data and could be useful for future beam test using pixel sensors. The digitizer that was developed can be used in the general ATLAS simulation software to take into account effects such parameters like thickness of the sensor and pixel pitch size. This will be used in the IBL ATLAS detector simulation software to simulate the slim edge planar sensor candidate for its sensor. The possibility to use TCAD electric field and Ramo Potential , including the mechanism of trapping in the simulation is an ideal tool for a detailed simulation of irradiated sensors and should be used to evaluate the performances of the ATLAS pixel detector after irradiation .

Conclusion

TCAD simulation have been used for a long time in various engineering field to study complex system and help with their design. The fast computer available today are now allowing the simulation of large structure using complex model to represent the physics implicated in the operation of planar pixel sensor and other semiconductor detection devices. In this work, I presented various simulation results on planar pixel sensor under various condition of operation. It has been shown that reduction of inactive area in planar pixel sensors can be achieve through the reduction of the number of guard rings and by using the slim edge structure. The thinning of sensors have been shown to be a valid method to obtain a depleted sensor at lower bias voltage while maintaining comparable breakdown voltage associated to thick sensor featuring‘ the same number of guard rings. Cutting edge width reduction have been shown to not influence the lateral depletion of the sensor. Finally, anomalous charge collection observed in highly irradiated silicon sensor has been explained to first principles using TCAD simulation

The comparison between experimental data and TCAD simulation has demonstrated that TCAD simulation can lead to quantitative results when tuned with the correct process parameters using the adequate physical models. Further work will be needed to obtain more quantitative results concerning breakdown voltage for unirradiated and irradiated silicon sensors. Qualitatively, results obtained here are however encouraging and further work will certainly lead to more reasonable results in the near future. Behavior of irradiated sensors has been reproduced in many aspects, from charge collection and change in bulk resistivity to double junction formation and failure of the guard ring structures. Further irradiation studies with test structures will be needed to improve the prediction power of TCAD simulation. Lower fluences should be explored to observe the failure point of guard ring structure.

Beam test activities have shown that planar pixel sensor can be operated with reduced inactive area and deliver the same performance as the actual planar pixel detector used in ATLAS inner detector. The need to study fine effects present in these device brought us to develop a simulation package to study the digitization models proposed for our device and compare easily with beam test data taken at CERN SPS and DESY Electron Synchrotron. A digitization model using the Ramo potential and TCAD electric field simulation was

developed to help with the study of the new sensor prototypes and to be used in full scale ATLAS and IBL simulation. Comparison with beam test data show the model reproduce well the data for unirradiated sensors with various geometry. The model proposed can be used to simulate trapping and thinning effects in irradiated sensors. Comparison with irradiated data and with FEI4 readout should be done to validate further the digitization model.

The future of silicon detector will be exciting. The arrival of 3D electronics, which allow to build four-side buttable device and readout electronics using different process for different functions ,which I had the privilege to see during my thesis, will change our way to work with silicon sensors and will allow for faster, more radiation hard detector that exhibit less inactive zones. The first 3D electronic ASIC, the OMEGAPIX, shown in figure 5.11, was received at LAL and open a new era for HEP experiment. I hope my contribution to the design of the omegapix-2 will lead to exciting new ASICs for the next generation of pixel sensors.

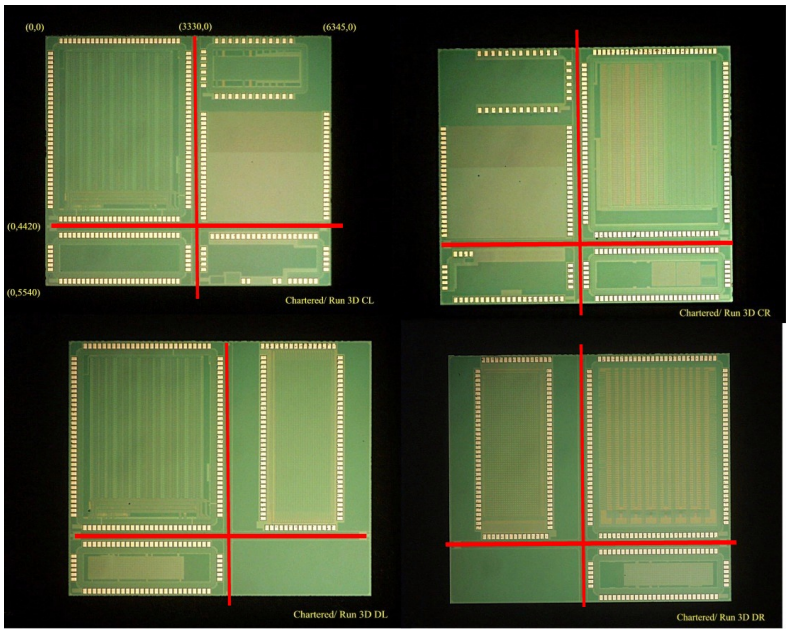

FIGURE 5.11 – The omegapix analog and digital tier

Personally ... Leaving your country, your family and your friends to pursue a career on an other continent is something I never thought I would do. It is a very difficult choice

to make but it is one I do not regret. During the last three year and half, I had the pleasure to work in one of the most amazing laboratory I have been honored to know. I travelled around the world to such exotic places as Alger, Bumerovska or Knoxville. I was granted a lot of autonomy and for that I thanks all the people who made this possible. I am not the same person today I was when I first left home with my package on my back. I discovered the real pleasure there can be in making errors and finding the good way to do things by myself. There was a lot of frustration, a huge amount of work that do not always show up in this thesis because choice were made and sometime because this work is hard to valorize. One of my greatest achievement during this thesis, in my opinion, was to build a clean room setup that is competitive and can reproduce results taken in other labs where clean room activities have been going on for many years, Unfortunately, sometime experimental work does not go as fast as you would like it to go. I hope the students who will take my place in this group will appreciate the work behind these setup, which will be working from day one for them, and will make good use of it to further advance the accuracy of our simulation models.

The knowledge I accumulated here will certainly follow me in my career and I hope to be able to continue it in the exciting field of experimental high energy physics as long as possible.

Word Cloud

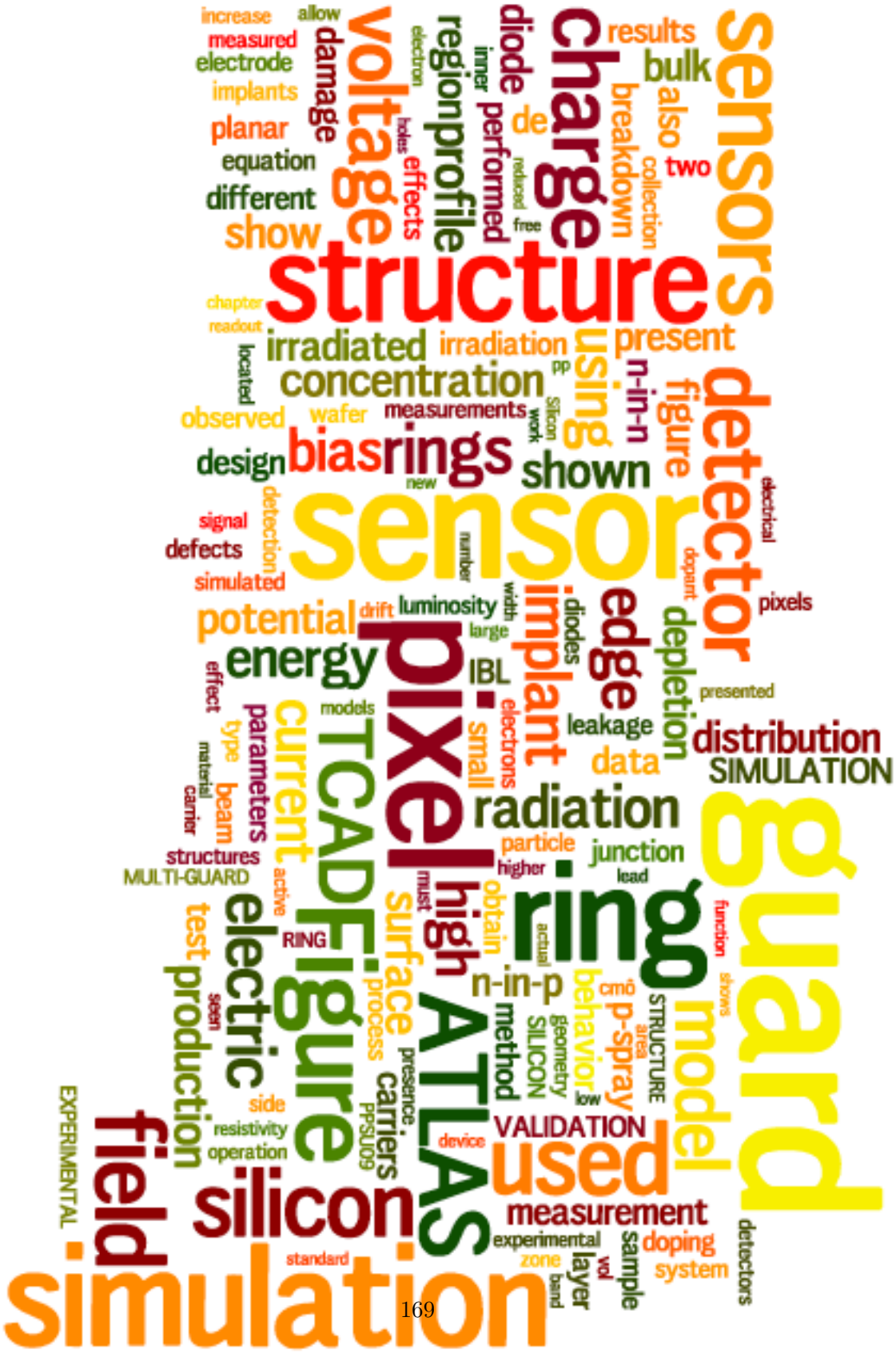
simulation
guard
sensor
pixel
ring
sensors
structure
detector
charge
voltage
silicon
field
ATLAS
used
model
Figure
TCAD
electric
current
implant
edge
energy
potential
bias
rings
irradiated
concentration
irradiation
present
using
shown
design
observed
wafer
measurements
figure
n-in-n
diode
bulk
results
also
two
breakdown
collection
region
profile
performed
de
damage
measured
electrode
implants
planar
equation
different
show
effects
holes
electron
inner
reduced
free
increase
allow
chapter
readout
located
pp
Silicon
work
new
detection
signal
defects
simulated
number
width
large
diodes
drift
luminosity
IBL
effect
models
electrons
small
leakage
depletion
dopant
electrical
pixels
presented
distribution
SIMULATION
data
radiation
particle
junction
lead
higher
structures
MULTI-GUARD
parameters
type
beam
material
carrier
active
must
obtain
high
surface
process
presence
carriers
PPSU09
RING
test
production
seen
n-in-p
behavior
cm
p-Spray
STRUCTURE
area
low
geometry
SILICON
method
VALIDATION
device
measurement
experimental
doping
sample
system
detectors
standard
zone
layer
vol
band
side
resistivity
operation
EXPERIMENTAL
function
shows

Bibliographie

[1] O. S. Brüning, P. Collier, P. Lebrun, S. nd Myers, R. Ostojic, J. Poole, and P. Proudlock, *LHC Design Report.* Geneva : CERN, 2004. 17

[2] G. Aad and al., "Atlas pixel detector electronics and sensors," *J. Isnt.*, vol. 3, p. 7007, 2008. 20, 21

[3] S. Coellia and the ATLAS Pixel Collaboration, "Mechanics and infrastructure for the atlas pixel detector," *J. Inst.*, vol. 172, pp. 280–283, 2007. 21, 23

[4] G. Aad and al., *ATLAS Pixel Detector Mechanics and Services.* Submitted to JINST, 2008. 22

[5] E. Verbitskaya, V. Eremin, Z. Li, J. Hâ˚rkËnen, and M. Bruzzi, "Concept of double peak electric field distribution in the development of radiation hard silicon detectors," *Nucl. Instrum. Meth. A*, vol. 583, no. 1, pp. 77 – 86, 2007. 22, 60, 64

[6] Z. Li and H. H. Kraner, "Fast neutron radiation damage effects on high resistivity silicon junction detectors," *J. Electronic Materials*, vol. 21(7), pp. 701–705, 1992. 22, 60, 64

[7] S. Baranov, M. Bosman, I. Dawson, V. Hedberg, A. Nisati, and M. Shupe, "Estimation of radiation background, impact on detectors, activation and shielding optimization in atlas," Tech. Rep. ATL-GEN-2005-001. ATL-COM-GEN-2005-001. CERN-ATL-GEN-2005-001, CERN, Geneva, Jan 2005. 24

[8] A. Tricomi, "Slhc : The lhc luminosity upgrade," *Nuclear Instruments and Methods in Physics Research Section A : Accelerators, Spectrometers, Detectors and Associated Equipment*, vol. 596, no. 1, pp. 43 – 47, 2008. Proceedings of the 8th International

Conference on Large Scale Applications and Radiation Hardness of Semiconductor Detectors. 30

[9] M. Capeans, G. Darbo, K. Einsweiller, M. Elsing, T. Flick, M. Garcia-Sciveres, C. Gemme, H. Pernegger, O. Rohne, and R. Vuillermet, "Atlas insertable b-layer technical design report," Tech. Rep. CERN-LHCC-2010-013. ATLAS-TDR-019, CERN, Geneva, Sep 2010. 32, 33

[10] "Utopia : Atlas slhc layout document,atl-p-ep-0001." 35

[11] F. Hartmann, *Evolution of silicon sensor technology in particle physics.* Springer, 2009. 39

[12] Y. Y. Peter and M. Cardona, *Fundamentals of Semiconductors, 3rd Edition.* Springer, 2003. 42, 45, 50

[13] G. F. Knoll, *Radiation Detection and Measurement.* Wiley, 4 ed., Aug. 2010. 44

[14] G. A. M. Hurkx, D. B. M. Klaassen, and M. P. G. Knuvers, "A new recombination model for device simulation including tunneling," *IEEE Trans. Electron Devices*, vol. 39, pp. 331–338, 1992. 47

[15] S. Selberherr, *Analysis and simulation of semiconductor devices.* Wien, 1984. 49

[16] D. M. Caughey and R. E. Thomas, "Carrier mobilities in silicon empirically related to doping and field," *Proc. IEEE*, vol. 55, no. 12, pp. 2192–2193, 1967. 50

[17] G. Lutz, *Semiconductor Radiation Detectors : Device Physics (Accelerator Physics).* Springer, May 2007. 51, 61, 64

[18] M. Mazziotta, "Electron-hole pair creation energy and fano factor temperature dependence in silicon," *Nuclear Instruments and Methods in Physics Research Section A : Accelerators, Spectrometers, Detectors and Associated Equipment*, vol. 584, no. 2-3, pp. 436 – 439, 2008. 52

[19] S. Ramo, "Currents induced by electron motion," *Proceedings of the I.R.E.*, vol. 27, p. 584, 1939. 53

[20] G. Cavalleri, "Extension of ramo's theorem as applied to induced charge in semiconductor detectors," *Nucl. Instr. and Meth.*, vol. 33, pp. 137–140, 1971. 54

[21] E. Gatti, A. Longoni, P. Rehak, and M. Sampietro, "Dynamics of electrons in drift detectors," *Nuclear Instruments and Methods in Physics Research A*, vol. 253, pp. 393–399, Jan. 1987. 54

[22] G. Lindstrom and al., "Developments for radiation hard silicon detectors by defect engineering–results by the cern rd48 (rose) collaboration," *Nucl. Instrum. Meth. A*, vol. 465, pp. 60 – 69, 2001. 63

[23] G. Lindstrom and al., "Radiation hard silicon detectors–developments by the rd48 (rose) collaboration," *Nucl. Instrum. Meth. A*, vol. 466, no. 2, pp. 308 – 326, 2001. 63

[24] A. Ruzin, "Recent results from the rd-48 (rose) collaboration," *Nucl. Instrum. Meth. A*, vol. 447, no. 1-2, pp. 116 – 125, 2000. 63

[25] M. Bruzzi and M. Moll, "Rd50 status report 2002/2003 rd50 : Radiation hard semiconductor devices for very high luminosity colliders," *CERN*, 2003. 63

[26] P. Luukka, "Status of defect engineering activity of the rd50 collaboration," *Nucl. Instrum. Meth. A*, vol. 530, pp. 152–157, 2004. 63

[27] F. Campabadal., M. Bruzzi, and M. Moll, "Rd50 status report 2004 : Radiation hard semiconductor devices for very high luminosity colliders," *CERN*, 2005. 63, 64

[28] M. Bruzzi and M. Moll, "Rd50 status report 2005 : Radiation hard semiconductor devices for very high luminosity colliders," *CERN*, 2005. 63

[29] M. Moll and B. Mara, "Rd50 status report 2007 - radiation hard semiconductor devices for very high luminosity colliders," *CERN*, 2008. 63, 64

[30] D. Menichelli, M. Bruzzi, Z. Li, and V. Eremin, "Modelling of observed double-junction effect," *Nucl. Instrum. Meth. A*, vol. 426, pp. 135–139, Apr. 1999. 64

[31] V. Eremin, E. Verbitskaya, and Z. Li, "The origin of double peak electric field distribution in heavily irradiated silicon detectors," *Nucl. Instrum. Meth. A*, vol. 476, no. 3, pp. 556 – 564, 2002. 64

[32] F. Moscatelli and al., "An enhanced approach to numerical modeling of heavily irradiated silicon devices," *Nucl. Instrum. Meth. B*, vol. 186, pp. 171–175, Jan. 2002. 64

[33] F. Moscatelli and al., "Comprehensive device simulation modeling of heavily irradiated silicon detectors at cryogenic temperatures," *IEEE Trans. Nucl. Sci.*, vol. 51, no. 4, pp. 1759–1765, 2004. 64

[34] M. Petasecca, F. Moscatelli, D. Passeri, G. Pignatel, and C. Scarpello, "Numerical simulation of radiation damage effects in p-type silicon detectors," *Nucl. Instrum. Meth. A*, vol. 563, no. 1, pp. 192 – 195, 2006. 64

[35] R. Wunstorf, M. Benkert, N. Claussen, N. Croitoru, E. Fretwurst, G. Lindstrom, and T. Schulz, "Results on radiation hardness of silicon detectors up to neutron fluences of 1015 n/cm2," *NIMA*, vol. 315, no. 1-3, pp. 149 – 155, 1992. 66

[36] L. Rossi, P. Fischer, T. Rohe, and N. Wermes, *Pixel Detectors : From Fundamentals to Applications*. Springer, 2006. 66, 79, 82

[37] J. Wustenfeld, *Characterisation of ionisation induced surface effects for the optimisation of silicon detectors for particle physics applications*. PhD thesis, Universitâ˚t Dortmund, 2001. 67

[38] E. H. Nicollian and J. R. Brews, *MOS Physics and Technology*. Wiley-Interscience, 2002. 67

[39] SILVACO International inc., 4701 Patrick Henry Drive, bldg 1, Santa Clara, CA 95054, *ATLAS User's Manual, Device Simulation Software*, June 2008. V 5.14.0.R. 77, 135

[40] E. Noschis, V. Eremin, and G. Ruggiero, "Simulations of planar edgeless silicon detectors with a current terminating structure," *Nucl. Instrum. Meth. A*, vol. 574, pp. 420–424, May 2007. 78, 79

[41] T. P. Ma and P. V. Dressendorfer, *Ionizing Radiation Effects in MOS Devices and Circuits*. Wiley-Interscience, 1989. 82

[42] M. Benoit, A. Lounis, and N. Dinu, "Simulation of guard ring influence on the performance of atlas pixel detectors for inner layer replacement," *J. Inst.*, vol. 4, no. 03, p. P03025, 2009. 84

[43] M. Benoit, A. Lounis, and N. Dinu, "Simulation of charge multiplication and trap-assisted tunneling in irradiated planar pixel sensors," Tech. Rep. ATL-UPGRADE-INT-2010-002, CERN, Geneva, Oct. 2010. 84

[44] A. Lounis, D. Martinot, G. Calderini, G. Marchiori, M. Benoit, and N. Dinu, "TCAD simulations of ATLAS pixel guard ring and edge structure for SLHC upgrade," Tech. Rep. ATL-COM-UPGRADE-2009-013, CERN, Geneva, Oct. 2009. 84

[45] M. Benoit, A. Lounis, and N. Dinu, "Simulation of radiation damage effects on planar pixel guard ring structure for ATLAS inner detector upgrade," *Nuclear Science, IEEE Transactions on*, vol. 56, pp. 3236–3243, Dec. 2009. 84

[46] G. Calderini, M. Benoit, N. Dinu, A. Lounis, and G. Marchiori, "Simulations of planar pixel sensors for the ATLAS high luminosity upgrade," *Nuclear Instruments and Methods in Physics Research Section A : Accelerators, Spectrometers, Detectors and Associated Equipment*, Apr. 2010. 84

[47] G. Casse and al., "Evidence of enhanced signal response at high bias voltages in planar silicon detectors irradiated up to 2.2Ã1016 neq cm-2," *Nucl. Instrum. Meth. A , j.nima.2010.04.085,*, vol. In Press, Corrected Proof, pp. –, 2010. 108

[48] M. Mikuz, V. Cindro, G. Kramberger, I. Mandic, and M. Zavrtanik, "Study of anomalous charge collection efficiency in heavily irradiated silicon strip detectors," *Nuclear Instruments and Methods in Physics Research Section A : Accelerators, Spectrometers, Detectors and Associated Equipment*, vol. In Press, Corrected Proof, pp. –, 2010. 108

[49] J. Harkonen, E. Tuovinen, Z. Li, P. Luukka, E. Verbitskaya, and V. Eremin, "Recombination lifetime characterization and mapping of silicon wafers and detectors using the microwave photoconductivity decay ([mu]pcd) technique," *Materials Science in Semiconductor Processing*, vol. 9, no. 1-3, pp. 261 – 265, 2006. 109

[50] R. Hull, *Properties of Crystalline Silicon (Emis Series)*. The Institution of Engineering and Technology, Jan. 1999. 125

[51] Geant4 Collaboration, S. Agostinelli, and al., "Geant4-a simulation toolkit," *Nuclear Instruments and Methods in Physics Research A*, vol. 506, pp. 250–303, July 2003. 149

[52] P. Roloff, "The EUDET high resolution pixel telescope," *Nuclear Instruments and Methods in Physics Research Section A : Accelerators, Spectrometers, Detectors and Associated Equipment*, vol. 604, pp. 265–268, June 2009. 149

[53] E. Fehlberg, "Low-order classical runge-kutta formulas with stepsize control," *NASA Technical Report*, pp. R–315, 1969. 151